WAVE-DRIVEN BOUNDARY LAYERS OVER PERMEABLE BEDS AND HYDRODYNAMICS OF WAVE-SWASH INTERACTIONS

by

Claudio Meza-Valle

A dissertation submitted in partial fulfillment of
the requirements for the degree of

Doctor of Philosophy

(Civil and Environmental Engineering)

at the

UNIVERSITY OF WISCONSIN–MADISON

2024

Date of oral examination: 04/15/2024

The dissertation is approved by the following members of the Final Oral Committee:

Nimish Pujara, Assistant Professor, Civil and Environmental Engineering

Hannah Zanowski, Assistant Professor, Atmospheric and Oceanic Sciences

Dante Fratta, Associate Professor, Geological Engineering

Dan Negrut, Professor, Mechanical Engineering

With all my love to my wife Pamela, and my children Kevin, Isabella and Emilia.

Thank you for being here.

Acknowledgments

First, I want to thank my family, Pamela, Kevin, Isabella, and Emilia, for their enormous support and their unconditional love and patience throughout this journey. I will always remember the sacrifice you have also put in following me in the doctorate process.

To my advisor, Dr. Nimish Pujara, for his trust and confidence in accepting me as his first student. You guide me to find myself through the research, remarking on my strengths and helping me improve my weaknesses as a researcher. Your support has led me to pursue high performance in investigation, and most importantly, you showed me that everything we do in research has to be meaningful for others. Thanks for allowing me to follow my dream of pursuing a Ph.D., and the opportunity of contributing to an area of science I am passionate about.

I am thankful for the help, feedback, and support I received from my friends in the Fluid Mechanics in Environmental Processes Lab (FMEP). The professors of the Water Resources Engineering group (WRE), Dr. Chin Wu, Dr. Daniel Wright, Dr. Paul Block, and Dr. Steve Loheide, from whom I always had encouragement and positive feedback about my research. Thanks for letting me be part of the WRE. Also, I want to thank James Lazarcik in the Water Science and Engineering Laboratory (WSEL) for the help he provided me in setting up multiple laboratory experiments and finding the right tools to build my experimental setup.

Thanks to my dear friend Hyungyu Sung, for his help in facilitating the codes for image processing and time series despiking presented in Chapter 4.

I want to thank my dissertation committee, Professors Hannah Zanowski, Dante Fratta, and Dan Negrut, who kindly accepted to be part of this work.

Last but not least, thanks to my relatives in Chile, who showed me that there is no distance when love is present.

“It may seem difficult at first, but all things are difficult at first.”

— Miyamoto Musashi, The Book of Five Rings

TABLE OF CONTENTS

List of Tables

List of Figures

WAVE-DRIVEN BOUNDARY LAYERS OVER PERMEABLE BEDS AND HYDRODYNAMICS OF WAVE-SWASH INTERACTIONS

Claudio Meza-Valle

Under the supervision of Dr. Nimish Pujara

At the University of Wisconsin-Madison

This thesis work comprises two main areas of study related to water waves on coastal processes: Wave-driven boundary layers over permeable sea beds and hydrodynamics of wave-swash interactions, which are a matter of interest in coastal science and engineering.

The effect of the permeable seabed on the development of the boundary layers driven by two different forcing conditions, transient oscillatory and solitary waves, is estimated by extending the classical formulations for an impermeable boundary. It is considered that within the porous region, flow velocities follow Darcy's law, which depends on pressure gradients as an effect of the transient waves and the hydraulic conductivity of the porous material. The physics of the interface fluid-permeable sea bed is modeled by implementing Dirichlet-type and Robin-type boundary conditions, based on the formulations stated by Le Bars and Worster (2006) and Beavers and Joseph (1967), approximated by employing analytical and numerical models. The analytical solutions based on the Dirichlet-type velocity boundary condition present a good agreement with numerical results using the Robin-type boundary condition, suggesting that the velocity boundary condition postulated by Le Bars and Worster can accurately capture the flow physics near the interface.

The developed analytical solutions presented an excellent match against experimental data in an oscillatory boundary layer generated by water waves propagating over a porous sea bed, presenting a better agreement than previous theories and remarking the effect of the transition zone inside the porous bed, where the viscous effects from the fluid are still valid until the fluid velocity matches Darcy's velocity.

The analyses highlight the induced flows for different hydraulic conductivities to assess the behavior and the structures of the velocities developed in the viscous boundary layer and to understand the variability of the developed bed shear stresses, which can be relevant to coastal processes, such as sediment transport.

Nearshore transport processes developing in coastal areas are postulated to be driven by wave-swash interactions, which have been mainly qualitatively quantified. In this work, using a train of consecutive solitary waves generated in a wave flume, the different categories of interactions are experimentally mimicked with a high degree of repeatability, allowing the construction of a broad set of wave-swash interactions observed in the field. In the experiments, the information on surface elevations, features of flows, and bottom pressure developed by the interactions are measured at the moment of the interaction. Observations showed that wave-swash interactions commonly present three main stages across the swash region, whose evolution and cross-shore location are linked to the type of interaction.

With the use of bed pressure measurements and free-surface displacement, the total vertical accelerations are estimated using a theoretical approach based on the vertical component of the Navier-Stokes equations. The analyses with the experimental information focus on the peak upward-directed acceleration generated by the wave-swash interactions, which induce significant magnitudes that exceed the acceleration of gravity in the swash, where the water depth is very shallow. It was found that the fluid velocities developed by the interactions follow vertical accelerations.

The wave-swash interactions and the developed total vertical accelerations and flows were quantitatively characterized in terms of the wave heights of the consecutive solitary waves and their separation times. For this, two dimensionless characteristic ratios were constructed, the wave height ratio, H_2/H_1, and the separation time, $T_{\text{sep}}/T_{\text{swash}}$, which show to be functional to characterize the hydrodynamics of wave-swash interactions.

Chapter 1

INTRODUCTION

1.1. Motivation and background

Waves impact different regions in the ocean as they propagate to the coast. In intermediate to shallower depths, waves influence the sea bed, inducing pressures and generating flows adjacent to the sea bed including mechanisms such as sediment transport, sea bed fluidization, and wave damping, among others. The characterization of these phenomena has been studied for more than 30 years to understand the effects of waves propagating over impermeable and permeable sea floors, for which there is no such uniformity in the proper physics to model the interface between the fluid and the porous sea bed.

Similarly, coastal areas are continuously affected by ocean oscillations acting as forcing conditions for coastal processes in the nearshore. There are a variety of water waves impacting the coast and generating coastal phenomena such as cross-shore and long-shore sediment transport, erosion, accretion, liquefaction, and in the long term, potentially modifying the morphological configuration of the coast. After the wave-breaking process, waves develop swash flows that interact with incoming wave events, called wave-swash interactions. These phenomena have been broadly studied and characterized qualitatively. However, there is a lack of information in terms of their quantification and their associated physical processes.

In this dissertation, these two coastal problems are worked on to bring new insights into the theory and analysis of waves propagating over permeable sea beds and the quantitative characterization of wave-swash interactions.

1.2. Wave-driven boundary layers over permeable beds

Oscillatory flows are present in a wide variety of problems across different areas of science and engineering. The well-known and classical solution to the boundary layer formed by oscillatory flow above a fixed flat plate was first presented by Stokes (1880), considered for different applications across science and engineering, and whose relevance lies on the fact that more complex situations involving boundary layer flows have arose along the years. Applications of the theory have addressed different problems; examples of this include flow driven by oscillating boundaries (Hossain and Daidzic, 2012), oscillatory pressure-driven flows (Issa, 2018), flow oscillations in a rotating system (Song and Rau, 2020), boundary layer transition Blondeaux and Vittori (2021), and quantifying sediment transport in oscillatory boundary layers (Mathieu et al., 2022; Vittori et al., 2020; Mazzuoli et al., 2019, 2020; Fromant et al., 2019). In all these applications, while there is general agreement on boundary layer solutions for impermeable boundaries, the nature of solutions with permeable boundaries differ substantially due to the ambiguities in modeling the boundary conditions at the interface between the free-fluid and the permeable region (Putnam, 1949; Hunt, 1959; Liu et al., 1996; McClain et al., 1977; Minale, 2014; Feng and Young, 2020; Samanta, 2017; Karmakar et al., 2022; Li et al., 2022; Angot et al., 2021).

Previous developments on the physics of boundary layers over permeable beds relate to steady flows, where the main challenge is setting the appropriate boundary conditions at the interface connecting the free fluid and the porous media flow (Beavers and Joseph, 1967; Saffman, 1971; Ochoa-Tapia and Whitaker, 1995a,b; James and Davis, 2001; Goharzadeh et al., 2005; Tilton and Cortalezzi, 2008; Ghisalberti, 2009; Goyeau et al., 2003; Le Bars and Worster, 2006; Zhang and Prosperetti, 2009; Nield, 2009; Morad and Khalili, 2009; Liu and Prosperetti, 2011; Morad and Khalili, 2009; Gupte and Adavani, 1997; Alazmi and Vafai, 2001; Wu and Mirbod, 2018; Davis and James, 2004; Arthur et al., 2013; Wu and Mirbod, 2018). One of the most studied boundary conditions to model the physics at the interface is the classical study of Beavers and Joseph (1967), which states that at the interface, there exist discontinuities between the velocity gradients occurring in the fluid and inside the porous region, which are related via properties of the porous

material such as the permeability and a slip coefficient, which depends on the "structure of the permeable material." Le Bars and Worster (2006) provided a significant advance on the Beavers and Joseph (1967) boundary condition. They showed how the same boundary condition could be adapted to state a continuity between the free fluid velocity and porous media velocity (Darcy's velocity) where the matching condition is applied at a certain depth below the interface. This region is then interpreted as a transition zone within the porous region where the free fluid velocity penetrates. This is consistent with physical intuition; since Darcy's flow is an averaged quantity inside the porous region, there should be a minimum distance below the interface before Darcy's law is valid. Therefore, the matching conditions between the fluid velocity and Darcy's velocity must occur at a distance greater than or equal to the averaging length. This insight provides two advantages: (1) it simplifies the interfacial boundary condition for analytical and numerical treatments and (2) it clarifies why previous studies have found the Beavers and Joseph slip coefficient to also be a function of the flow instead of being solely a function of the porous material. Numerical simulations in Le Bars and Worster (2006) show that their boundary condition reproduces closely flow obtained from the original condition proposed by Beavers and Joseph (1967). Additionally, only slight differences are found compared to the Darcy-Brinkman formulation (Brinkman, 1949).

From subsequent studies, it is now established that there does indeed exist a transition layer inside the porous region into which the free fluid flow penetrates and after which the velocity matches its porous media flow value. Several works (Le Bars and Worster, 2006; Tilton and Cortalezzi, 2008; Nield, 2009; Morad and Khalili, 2009) state that the characteristic length for this transition zone is represented by the squared root of the permeability, but data from experiments and numerical simulations suggest that the grain diameter may be a better characteristic length for this depth (Goyeau et al., 2003; Goharzadeh et al., 2005; Zhang and Prosperetti, 2009; Liu and Prosperetti, 2011). Both numerical simulations and experiments agree, however, that the thickness of the transition layer remains almost invariant for different flow conditions (*e.g.*, Reynolds numbers, flow channel height).

Building on these developments of steady viscous flow over a permeable bed, a set of analytical solutions for the laminar boundary layer velocities induced by linear oscillatory flows over a

permeable bed is presented, including explicitly a transition zone in the solutions via an empirical parameter, which was found scaling with the grain diameter. Previous theories on this matter, such as Liu et al. (1996) and McClain et al. (1977), have not explicitly considered the transition zone found in steady flow. Validation includes comparisons of the developed theory with numerical solutions of the boundary layer equations and experimental data from Liu et al. (1996), showing an excellent agreement with the analytical solutions. Error analysis allowed to make sensitivity of the solution for different values of the empirical parameter and its agreement with experimental data. The theory proposed, which is much simpler than previous theories, performs much better against data, although with an empirical parameter.

The slip velocity at the interface and the boundary layer velocity profiles are sensitive to the permeability of the porous material, while the thickness of the transition zone remains almost unaffected for seabeds with similar characteristics. The novel method can be seen as an extension to the classical boundary layer formulations for an impermeable boundary condition (Stokes, 1880; Batchelor, 2000; Svendsen, 2006) to model the oscillatory boundary layer flows over the permeable bed. In a complementary manner, the theoretical developments on permeable sea beds are extended to consider a transient solitary wave as a forcing condition, extending the solutions for an impermeable sea bed proposed by Liu and Orfila (2004).

1.3. Wave-swash interactions

Studies have shown evidence of irreversible erosion cases in different places due to high-energy wave events (Martínez et al., 2018; Rangel-Buitrago et al., 2015; Masselink et al., 2016). Hydrodynamically, waves transform in their propagation towards coastal areas developing several subregions in the nearshore (Dean and Dalrymple, 2004; Holthuijsen, 2007; Jackson and Short, 2020). The last of these stages corresponds to the swash zone, which is continuously affected by broken incident waves, and determined by the movement of the shoreline. According to the forcing conditions, the swash can experience fast changes in the coastal processes and act as the principal precursor for sediment transport and liquefaction in this zone (Elfrink and Baldock, 2002; Puleo

and Butt, 2006; Puleo and Torres-Freyermuth, 2016; Florence et al., 2022; Stark et al., 2022). The extent of the swash is delimited by the upper and lower limit of the runup and rundown process after the wave breaking, which consequently will develop the upwash and backwash flows on the beach slope, respectively. Figure (1.1) shows a detailed scheme of the surf and swash zones, specifying the runup and rundown limits, and the wave-swash interactions region.

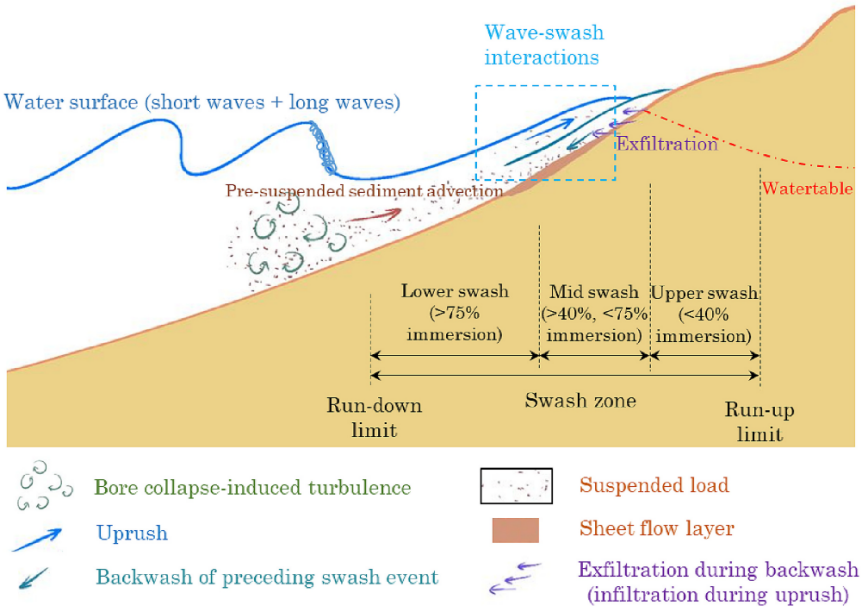

Figure 1.1: Cross-shore profile of the nearshore coastal region (Chen et al., 2023).

The swash is a dynamic region mainly affected by incident broken waves, and it ideally begins with the shoreward movement of the shoreline from a still water level (SWL). It is represented by decelerating and accelerating flows moving up and down the beach, delimited by a complete runup-rundown cycle, and it is the coastal space where the wave-swash interactions develop. At this point, incoming waves interact with the developed upwash or backwash flows of the previous event, modifying their characteristics according to the nature of a single wave event. The wave-swash interactions have been qualitatively characterized and described according to Hughes and Moseley (2007) and identified as a potential agent in the sediment transport process in this zone (Puleo et al., 2000). The study of this phenomenon has become relevant in ocean sciences and coastal engineering due to two main aspects: (1) interactions develop vertical pressure gradients

and accelerations and trigger sediment transport and liquefaction in the surf and swash zones, and (2) interactions modify the existing sediment transport mechanism in these coastal regions.

Considering a single two-wave interaction event, three main physical processes are identified for this phenomenon, characterized according to the following: (a) The upwash flow of the second wave catches the upwash flow of the first wave event (wave-upwash interaction). (b) The upwash flow of the second wave catches with the backwash flow of the first wave event. The flow is again pushed shoreward by the incoming upwash flow (weak wave-backwash interaction). (c) Physically similar to case (b). However, in this latter, the backwash flow of the first wave is strong, inducing a forced receding of the incoming flow, generating a stationary hydraulic jump (strong wave-backwash interaction). In specific cases, the development of a free swash occurs on the upper beach when a swash event does not present a wave-swash interaction. This event can appear as the time between successive wave events is long enough or when the wave event corresponds to a single event, which significantly dominates as a forcing condition over irregular waves in coastal areas, such as tsunamis or solitary waves, which is the matter of study in this work.

Despite the different efforts, the scientific community in coastal processes accepts that wave–swash interaction lacks quantitative characterization, and the associated physical processes such as sediment transport need to be studied (Masselink and Puleo, 2006; Puleo and Butt, 2006; Puleo and Torres-Freyermuth, 2016; Chardón-Maldonado et al., 2016; Chen et al., 2023). On the coast, the sediment transport is induced and modified by the forcing condition (Hughes et al., 1997; Baldock and Hughes, 2006), whose interaction can play a principal role in the location, direction, and how sediments transport in the swash zone, such as bedload and suspension, or able to trigger liquefaction (Sumer, 2014). Experimentally, regular waves, bi-chromatic waves, solitary waves, and dam-break induced bore has been functional to understand sediment transport and flow characteristics in the swash zone (O'Donoghue et al., 2010; Sou and Yeh, 2011; Kikkert et al., 2012; Lo et al., 2013; Pujara et al., 2015b; Chardón-Maldonado et al., 2016; O'Donoghue et al., 2016; Wu et al., 2021; Barranco and Liu, 2021; Pintado-Patiño et al., 2021). Several works, such as Alsina et al. (2009, 2012, 2016, 2018), show that collapsing bores can lift and advect the sediment transport

to the swash zone. Some authors have analyzed possible wave-induced liquefaction in coastal regions. This phenomenon is strongly related to the pressure gradients and vertical accelerations the seabed can experience as waves propagate onshore developing local liquefaction (Sumer, 2014). Studies to understand liquefaction have considered different setups and characteristics to analyze the phenomena, especially field measurements and laboratory experiments. Yeh and Mason (2014) shows that a tsunami-like solitary wave could also induce significant pressure gradients as the wave reaches a coastal region. The analytical results from their tsunami model show the built-up of the momentary liquefaction process (Sumer, 2014; Mason and Yeh, 2016), which is a principal factor in the sediment transport process and observed scouring effects. In the same manner, field studies have revealed liquefaction as a relevant developing wave-induced process in the surface layers of sand beaches in coastal regions, which can be a principal source initiating sediment suspension and, subsequently, bedload (Baldock et al., 2001; Stark et al., 2022; Florence et al., 2022). These studies emphasize developing pressure gradients in coastal regions induced by wave events associated with tropical storms, which indicate a potential vertical movement of the loose sediment in this region. Considering these findings, it is also important to assess the characteristics of developing vertical accelerations induced by the different wave-swash interactions.

Experimental and numerical evidence shows that predicting the physical processes that trigger or modify sediment transport, such as pressure gradients and vertical accelerations, associated with wave-swash interactions is difficult since even when measured and simulated wave trains present similar characteristics in surface elevations and velocities, sediment transport associated with them can behave differently in erosion and accretion. Numerical software does not account for physical processes to represent or numerically resolve the complete physics of wave hydrodynamics and sediment transport processes in the swash zone or coastal regions (Masselink et al., 2009; Smit et al., 2010; Ruffini et al., 2020; Mancini et al., 2021). Even when sediment transport mechanisms such as bedload and suspended sediment transport are well understood and implemented, they lack representation for pressure gradients and induced vertical accelerations. A recent study performed by Chen et al. (2023) conducted an extensive review of sediment transport models, concluding that

even though there is an acceptance that wave-swash interactions play a critical role in the sediment transport in the swash, there is no such a parameter(s) to determine the interaction type.

1.4. Background on water waves

1.4.1. Oscillatory waves

In the ocean, it is possible to find different types of waves whose physics is determined by the nature of their generation process. In deep to intermediate water depths, wind-generated waves propagate with a regular-like shape with a specific fixed amplitude and frequency (Dean and Dalrymple, 2004; Holthuijsen, 2007). The surface elevation ζ for a small-amplitude progressive wave traveling in the positive x-direction is given by

$$\zeta(x', y', z') = a' \cos(k'x' - \omega't') \tag{1.1}$$

where $a' = H'/2$ is the wave amplitude, and H' is the wave height. The wave number is given by $k' = 2\pi/L'$, and ω' is the dispersion relation given by

$$\omega'^2 = k'g'\tanh(k'h') \tag{1.2}$$

with g' and h' are the acceleration of gravity and water depth, respectively. The wave length L' and the wave celerity (phase velocity c') are defined as

$$L' = \frac{g'T'^2}{2\pi}\tanh(k'h') \tag{1.3}$$

and

$$c' = \frac{\omega'}{k'} = \frac{L'}{T'}, \tag{1.4}$$

with T' the wave period. The flow field is given by the horizontal and vertical velocity components

$$u'(x', y', z') = \frac{k'a'g'}{\omega'}\frac{\cosh[k'(h' + z')]}{\cosh(k'h')}\cos(k'x' - \omega't') \tag{1.5}$$

$$w'(x', y', z') = \frac{k'a'g'}{\omega'} \frac{\sinh[k'(h' + z')]}{\cosh(k'h')} \sin(k'x' - \omega't'), \tag{1.6}$$

and the pressure induced by the transient wave is given by

$$p'(x', y', z') = \rho' g' a' \frac{\cosh[k(h + z)]}{\cosh(kh)} \cos(k'x' - \omega't'). \tag{1.7}$$

The small-amplitude waves lies on the assumption that

$$\frac{k'a'}{\tanh(k'h')} \ll 1. \tag{1.8}$$

From the above expression, it is possible to observe that in a deep water condition $\tanh(k'h') \to 1$ as $h' \to \infty$, implying that $k'a' \ll 1$. On the other hand, as $h' \to 0$, $\tanh(k'h') \to k'h'$, meaning that in shallow water, the relation $a'/h' \ll 1$ stands.

For standing waves, the relations presented above remains with slight modifications in their oscillatory terms (Dean and Dalrymple, 2004).

1.4.2. Solitary waves

Solitary waves are finite small-amplitude waves whose surface elevation, which is permanent in its propagation process, is given by the following expression according to Boussinesq (1872)

$$\zeta(x', t') = H' \text{sech}^2[k'(x' - c't')]. \tag{1.9}$$

For a solitary wave, the wave number, k', and celerity, c', are given by

$$k' = \frac{1}{h'} \sqrt{\frac{3}{4}\epsilon} \quad ; \quad c' = \sqrt{g'(H' + h')} \tag{1.10}$$

with $\epsilon = H'/h'$ the wave steepness or non-linearity parameter, and g' stands for the acceleration of gravity. The wavelength and wave period for a solitary wave are defined as

$$L' = 2\pi/k' \quad ; \quad T' = 2\pi/k'c'. \tag{1.11}$$

The horizontal and vertical fluid velocities developed by a solitary wave in a constant depth region are given by the following expressions

$$u(x', z', t') = U' \text{sech}^2[k'(x' - c't')], \tag{1.12}$$

$$w(x', z', t') = U'\sqrt{3\epsilon}\left(\frac{z' + h'}{h'}\right)\text{sech}^2[k'(x' - c't')]\text{tanh}[k'(x' - c't')], \tag{1.13}$$

where $U' = \epsilon\sqrt{g'h'}$ is the maximum fluid velocity occurring under the wave crest.

The pressure under the solitary wave crest is given by

$$p'(x', t') = \rho' g' \zeta',$$

which can be rewritten as

$$p'(x', t') = \rho' g' H' \text{sech}^2[k'(x' - c't')]. \tag{1.14}$$

1.5. Outline of the dissertation

In Chapter 2, theoretical and numerical developments on wave-driven boundary layer flows over permeable beds are presented. This work analyzes the possibility of two (2) different boundary conditions to model the physics at the interface fluid-porous region for an oscillatory forcing condition. The developed analytical equations, which include a transition zone within the porous bed where the viscous flows from the fluid are still valid, extend the classical Stokes solutions for impermeable seabed to include the effects of the porous region. Results were validated against experimental data. The chapter also presents an extension to the theoretical developments made by Liu and Orfila (2004) on transient solitary wave-induced boundary layer flows over an impermeable sea bed, for which the permeable seabed boundary conditions are also implemented. Part of this chapter was already published in the journal *Physics of Fluids* (Meza-Valle and Pujara, 2022).

Chapter 3 presents an experimental work to characterize wave-swash interactions quantitatively. In this investigation, experiments using two (2) consecutive solitary waves of different

wave amplitudes separated by specific times are performed in a wave flume to analyze the distribution of the interactions in terms of two (2) constructed characteristic ratios, the wave (H_2/H_1) and temporal ($T_{\text{sep}}/T_{\text{swash}}$) ratios. A theoretical approach to calculate the total vertical accelerations induced by the wave-swash interactions is functional to use the information from measurements of surface elevations and bottom pressures and gives relevant information on the interactions and their developed kinematic magnitudes and their relations. This work is under review in the Journal of Geophysical Research: Oceans.

Chapter 4 presents a recent work carried out in the directional wave basin of the Oregon State University to analyze flows and runups induced by a train of consecutive solitary waves separated at specific times. The train of solitary waves is propagated for two different angles of incidence to assess the impact of the wave obliquity on the induced velocities, accelerations, and maximum runups. These quantities are characterized quantitatively through two characteristic ratios, the wave height and dimensionless separation time, constructed from the wave properties. Estimated runups are also compared to theoretical formulations from the literature, presenting a good agreement for wave events with no obliquity.

Conclusions of the dissertation are presented in Chapter 5.

Chapter 2

WAVE-DRIVEN BOUNDARY LAYERS OVER PERMEABLE BEDS

2.1. Introduction

In their propagation process, waves in the ocean are prone to develop flows adjacent to the seabed, which in many cases is a porous medium. Several authors, such as Putnam (1949); Hunt (1959); Liu et al. (1996); McClain et al. (1977), have treated this problem to model the fluid-permeable seafloor interface by extending the well-known and classical solution to the boundary layer formed by oscillatory flow over an impermeable flat plate (Stokes, 1880). However, despite the different developments and theories, there is no general solution to the boundary condition that should be applied at the interface, and there exists some ambiguity in how to model the boundary condition.

Based on prior developments of steady viscous flow over a permeable bed, a set of analytical solutions for the laminar boundary layer velocities induced by linear oscillatory flows over a permeable bed is formulated in this work. Earlier theories on this subject, such as Liu et al. (1996) and McClain et al. (1977), have not explicitly considered the transition zone found in a steady flow (Le Bars and Worster, 2006). The developments presented in this work include the effect of a transition zone inside the porous region, along which the effects of the viscous fluid are still valid before it matches Darcy's velocities. Solutions show that this transition scales with the grain diameter or analogously, with the square root of the hydraulic conductivity of the porous media.

Comparisons of the proposed theory with numerical solutions of the boundary layer equations and experimental data from Liu et al. (1996) show excellent agreement with the analytical

solutions. Error analysis performed on the empirical parameter was carried out to sensitize the analytical solution and its agreement with experimental data. The validated analytical solutions for the oscillatory wave case correspond to an extension of the well-known boundary layers solutions for impermeable boundaries (Stokes, 1880; Batchelor, 2000; Svendsen, 2006), which can be recovered from the developments presented in this work as the permeability conditions of the seabed tend to zero. Analytical solutions considering a transient solitary wave as a forcing condition are also presented, which extend the impermeable sea bed solutions from Liu and Orfila (2004).

This chapter presents new analytical and numerical solutions for laminar boundary layer flows induced by oscillatory and transient solitary waves over a permeable sea bed, where the effects of hydraulic conductivity of the porous material are included in the solutions of the boundary layer equations. The solution and analyses of developed bed shear stresses are also presented.

2.2. Boundary layer theory

A boundary layer corresponds to a thin region that develops near a boundary due to the viscous effects of the fluid. Inside this region the fluid velocities vary rapidly diffusing vertically through the boundary layer width until they reach the stream velocity of the fluid. It is known that boundary layer equations correspond to an exact solution of the Navier-Stokes equations, and are given by the following dimensional expressions according to Batchelor (2000)

$$\frac{\partial u'}{\partial t'} = -\frac{1}{\rho}\frac{\partial p'}{\partial x'} + \nu\frac{\partial^2 u'}{\partial z'^2} \tag{2.1a}$$

$$0 = -\frac{1}{\rho}\frac{\partial p'}{\partial z'} \tag{2.1b}$$

$$\frac{\partial u'}{\partial x'} + \frac{\partial w'}{\partial z'} = 0 \tag{2.2}$$

where u' is the streamwise horizontal velocity, w' is the vertical velocity, p' is the fluid pressure, ρ' is the fluid density, and ν' is the kinematic viscosity. Eqs. (2.1) correspond to the horizontal and vertical momentum equations and Eq. (2.2) is the continuity equation.

The boundary layer is generated due to vorticity effects developed at the interface fluid-boundary, which diffuses vertically, so the fluid velocity inside the boundary layer can be decomposed as $u' = u'_i + u'_r$, where u'_i and u'_r are the irrotational and rotational velocities, respectively. In absence of pressure gradients, the fluid velocity inside the boundary layer is given by the following expression

$$\frac{\partial u'}{\partial t'} = \nu \frac{\partial^2 u'}{\partial z'^2}, \tag{2.3}$$

which for an impermeable interface condition will follow that $u' = 0$ at $z' = 0$ and $u' = u'_i$ as $z' \to \infty$ (Stokes, 1880; Rosenhead, 1988; Batchelor, 2000). Similarly, as the horizontal irrotational velocity, u'_i, does not depend on the vertical coordinate, Eq. (2.3) can also be rewritten as

$$\frac{\partial u'_r}{\partial t'} = \nu \frac{\partial^2 u'_r}{\partial z'^2}. \tag{2.4}$$

2.3. Boundary layers over permeable sea beds

Considering that a seafloor is made of a porous material, (e.g., gravels and sands), the velocity inside this region can be modeled by Darcy's law for permeable bed flows, meaning that the velocity inside the permeable seabed can be determined by the dynamic pressure gradients according to Bear (1972) as follows

$$u'_s(x', z', t') = -\frac{K'}{\rho' g'} \frac{\partial p'}{\partial x'}, \tag{2.5a}$$

$$w'_s(x', z', t') = -\frac{K'}{\rho' g'} \frac{\partial p'}{\partial z'}, \tag{2.5b}$$

in which the subscript, s, denotes the variables inside the permeable bed, and K' represents the hydraulic conductivity of the porous region.

2.3.1. Oscillatory wave case

Starting from the classical boundary layer equations (Batchelor, 2000) and the dimensional oscillatory waves properties presented in Section (1.4.1), the usual assumptions in oscillatory systems are that the streamwise length scale is larger than the cross-stream length scale and velocity variations are much stronger in the cross-stream direction than in the streamwise direction. This leads to the neglect of the non-linear advective acceleration in the streamwise momentum equation, which is much smaller than the unsteady acceleration. In dimensionless form, the momentum equations are

$$\frac{\partial u}{\partial t} = \frac{\partial (U\mathrm{e}^{it})}{\partial t} + \frac{\partial^2 u}{\partial \eta^2} \tag{2.6a}$$

$$0 = \frac{\partial p}{\partial \eta} \tag{2.6b}$$

where Eq. (2.6a) and Eq. (2.6b) correspond to the streamwise and cross-stream momentum balances, respectively, and

$$\begin{gathered} x = k'x' \; ; \quad \eta = z'/\sqrt{\nu'/\omega'} \; ; \quad t = \omega' t' \; ; \\ p = p'/\rho' U_0'^2 \; ; \quad (u, w, U) = (u', w', U')/U_0' \end{gathered} \tag{2.7}$$

where x' and z' are the dimensional streamwise and cross-stream coordinates with corresponding dimensional velocities u' and w', respectively. Further, p' is the dynamic fluid pressure, ρ' is the fluid density and ν' corresponds to the kinematic viscosity of the fluid. For sake of simplicity, some primes are dropped in the following calculations.

The oscillatory free-stream velocity in dimensional form is $U\mathrm{e}^{i\omega t}$, which has a characteristic magnitude U_0 and where U is complex and can vary in x-direction. The cross-stream coordinate z is scaled by the boundary layer thickness $\sqrt{\nu/\omega}$, and η is therefore the stretched cross-stream coordinate inside the boundary layer. In Eq. (2.6a), it is considered that the free-stream acceleration balances the horizontal pressure gradient

$$-kU_0^2 \frac{\partial p}{\partial x} = \omega U_0 \frac{\partial (U\mathrm{e}^{it})}{\partial t}.$$

The dimensionless continuity equation is

$$\frac{\partial u}{\partial x} + \sqrt{\frac{\omega}{\nu k^2}} \frac{\partial w}{\partial \eta} = 0. \tag{2.8}$$

where $\sqrt{\omega/\nu k^2}$ is the Womersley number.

The flow inside the porous region is modeled as described by Darcy's law (Bear, 1972), given in dimensionless form by

$$u_s(x, \eta, t) = -\sigma \frac{U_0}{(\omega/k)} \frac{\partial p}{\partial x} \tag{2.9}$$

with

$$\sigma = \frac{K'\omega}{g'}, \tag{2.10}$$

where σ is the dimensionless hydraulic conductivity and K' is the hydraulic conductivity of the permeable material. Figure (2.1) shows the variation of the parameter σ for different values of the hydraulic conductivity, K', and wave periods, T'. Values of K' ranging from 10^{-5} m/s to 10^{-1} m/s are chosen to represent typical values for fine sands to gravel (Domenico and Schwartz, 1990) and the range of T' covers characteristic values of wave periods (1 s to 10 s) of in intermediate and shallow waters.

2.3.2. Solitary wave case

The physical problem is extended to include a solitary wave propagating over a permeable seafloor considering the dimensional properties for a transient solitary wave presented in Section (1.4.2). The origin of the reference system $(x', z') = (0, 0)$ is at the still water level pointing in the positive (x', z')-directions, so the seafloor is located at $z' = -h'$. The variables inside the permeable bed are those associated with the subscript s. The surface elevation of the solitary wave ζ' propagates over a constant depth h', the wave height is represented by H', and the length scale is associated with the solitary wave wavelength, L'. The time scale is given by the expression $L'/\sqrt{gh'}$. Next, a set of non-dimensional variables are introduced, which correspond to the spatial coordinates and some physical properties of the solitary wave

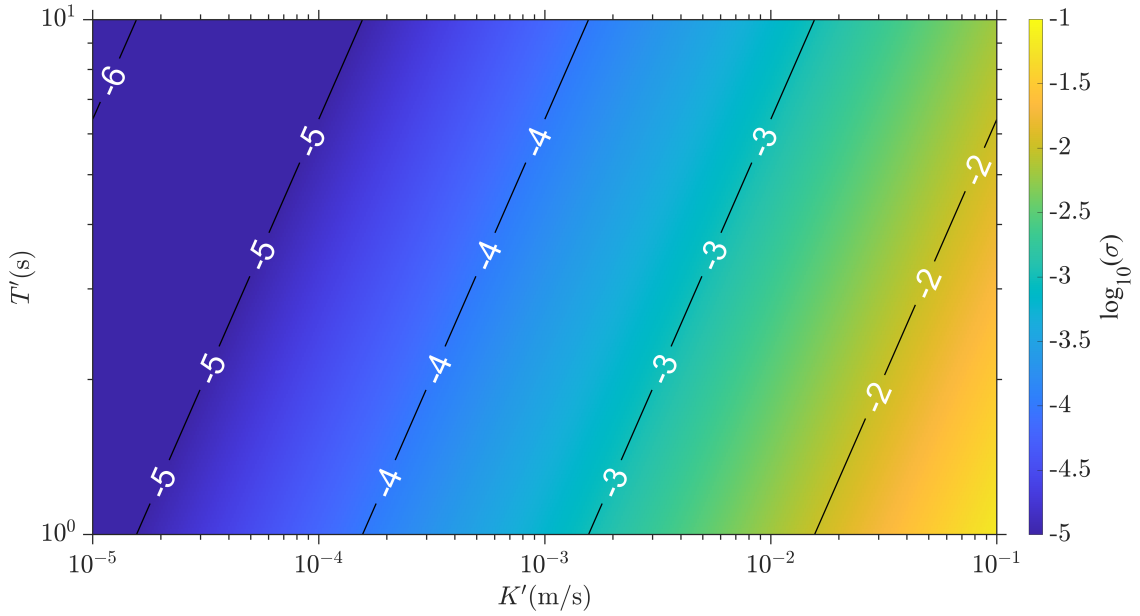

Figure 2.1: Variation of $\sigma = K'\omega/g'$ for different hydraulic conductivities, K', and wave periods, T'.

$$\begin{cases} x = x'/L' \; ; z = z'/h' \; ; t = \sqrt{g'h'}t'/L' \\ \zeta = \zeta'/H' \; ; p = p'/\rho g' H' \; ; \\ u = u'/\epsilon\sqrt{g'h'} \; ; w = \mu w'/\epsilon\sqrt{g'h'} \; ; \end{cases} \tag{2.11}$$

Here, u_i' and w_i' correspond to the horizontal and vertical irrotational velocities propagating in the positive (x', z')-directions, respectively. The wave steepness of the solitary wave, $\epsilon = H'/h'$, was already introduced, and $\mu = h'/L'$ is the relative depth.

Following the formulations from Mei et al. (2005), the dimensionless solitary wave free surface elevation, ζ, can be represented as follows:

$$\zeta = \text{sech}^2\left[\frac{\beta}{\mu}(x - ct)\right], \tag{2.12}$$

with

$$\beta = \sqrt{\frac{3\epsilon}{4}} \quad \text{and} \quad c = \sqrt{1+\epsilon}. \tag{2.13}$$

Introducing the velocity potential ϕ for the irrotational velocity, the horizontal and vertical components (u, w) can be expressed as

$$u_i(x,z,t) = \frac{\partial \phi}{\partial x} = \zeta \tag{2.14}$$

$$w_i(x,z,t) = \frac{\partial \phi}{\partial z} = \sqrt{\frac{3\mu^2}{\epsilon}}(z+1)q\left\{-\epsilon\zeta^2\right\}, \tag{2.15}$$

where the subindex i denotes the irrotational condition.

The viscous effects become important in a thin boundary layer adjacent to the bottom (at $z = -1$), implying that the no-slip boundary condition is satisfied. Inside the boundary layer, the velocity components are expressed as the summation of irrotational and rotational parts. Thus,

$$u(x,z,t) = u_i(x,t) + u_r(x,z,t), \quad w(x,z,t) = w_r(x,z,t), \tag{2.16}$$

where u and w are the horizontal and vertical velocity components in the boundary layer and u_i is given in Eq. (2.14). Inside the boundary layer, the vertical pressure gradient is small enough to be ignored at the leading order. On the other hand, the horizontal pressure gradient is balanced by the acceleration associated with the irrotational velocity. Since the ratio of the boundary layer thickness and the length scale is $\mathcal{O}(\alpha)$, the next stretched coordinate is introduced

$$\eta = \frac{z+1}{\alpha/\mu} \tag{2.17}$$

where

$$\alpha^2 = \frac{\nu}{L'\sqrt{g'h'}}. \tag{2.18}$$

Here, ν corresponds to the kinematic viscosity of the fluid, and α^2 can be understood as an inverse Reynolds number.

The linearized momentum equation following Liu and Orfila (2004) expressions for the rotational velocity in the boundary layer is

$$\frac{\partial u_r}{\partial t} = \frac{\partial^2 u_r}{\partial \eta^2}, \tag{2.19}$$

and leading order vertical component of the rotational velocity is integrated from the continuity equation

$$\frac{\partial u_r}{\partial x} + \frac{\partial w_r}{\partial \eta} = 0. \tag{2.20}$$

The boundary conditions for the boundary layer flow can be expressed as follows. The rotational velocity components vanish outside the boundary layer, i.e.,

$$u_r,\ w_r \rightarrow\ 0\ \text{ as } \eta\ \rightarrow\ \infty \tag{2.21}$$

and on the other hand, the no-slip boundary condition on the seafloor must be satisfied,

$$u_r + u_i = 0\ \text{ on } \eta = 0. \tag{2.22}$$

The solution for the boundary value problem of u_r, described in Eqs. (2.19), (2.21), and (2.22), has been provided in Liu and Orfila (2004, 2007a) for an impermeable sea bed case.

To include the effects of the porous media, the expression for the horizontal velocity u_s' inside the permeable bed is obtained by taking the derivative of the dimensional dynamical pressure given by Eq. (1.14), whose derivative with respect to x' yields

$$\frac{\partial p'}{\partial x'} = -\rho g' \{2k'H'\text{sech}^2[k'(x' - ct')]\text{tanh}[k'(x' - c't')]\}. \tag{2.23}$$

Replacing now (2.23) on (2.5a), the following dimensional expression for the permeable bed velocity u_s' inside the permeable bed is obtained

$$u_s'(x', z', t') = 2k'K'H'\text{sech}^2[k'(x' - c't')]\text{tanh}[k'(x' - c't')]. \tag{2.24}$$

According to this theory, the flows inside the permeable bed are driven by the dynamic pressure p' associated with the transient wave propagating on the free surface. Then, the permeable bed velocity u_s' at $\eta \leq 0$ is stated as

$$u_s' = \sigma u_s(x, \eta \leq 0, t), \tag{2.25}$$

where $\sigma = K'H'/L'\epsilon\sqrt{g'h'} = K'\mu/\sqrt{g'h'}$ is the non-dimensional coefficient for the velocity u_s' inside the permeable bed. It is important to notice that the permeable bed velocity (2.25) is different from the irrotational velocity presented in Eq. (2.14). The irrotational velocity under a solitary wave is always positive, moving in the same direction as the wave propagation.

2.4. Interfacial boundary conditions

Working in a two-dimensional Poiseuille flow scenario, Beavers and Joseph (1967) (BJ) postulated that there is a transference of the tangent velocity from the fluid to the permeable bed at the interface ($\eta = 0$), which can be treated as a discontinuity between the velocities in these two domains. Physically, at the interface, there is an equilibrium between the velocity gradients above the permeable bed and inside the permeable bed. This boundary condition is written as

$$\frac{\partial u}{\partial \eta} = \frac{\kappa}{\sqrt{\sigma}}(u - u_s) \quad \text{on } \eta = 0. \tag{2.26}$$

The parameter κ, corresponds to the slip coefficient, and was introduced as an empirical parameter that depends on the structure of the porous material. With κ determined experimentally, BJ's boundary condition yielded good comparison with their experimental data, and the form of their boundary condition was provided further theoretical support by Saffman (1971).

Le Bars and Worster (2006) (LW) presented an analysis that compared the two-layer system (Stokes flow in the free fluid domain and Darcy's flow in the porous medium) with a single layer system (Darcy-Brinkman formulation where the porosity smoothly transitions from its porous media value deep within the porous layer to zero in the free fluid). They found that the Stokes flow penetrates to a small depth into the porous medium, which constitutes a transition zone and whose magnitude scales with the pore size. Thus, LW suggest that the BJ boundary condition can be simplified by re-writing it as a continuity between the fluid velocity and Darcy's velocity at a distance δ within the porous boundary

$$u_s = u \quad \text{at } \eta = -\delta \tag{2.27}$$

where δ is the transition zone depth in dimensionless form. LW further show that this transition depth takes the following form (in our notation)

$$\delta = m\sqrt{\frac{\sigma}{n}} \tag{2.28}$$

where n is the porosity and m is an $\mathcal{O}(1)$ constant. The equivalence between the LW boundary condition (Eq. (2.27)) and the BJ boundary condition (Eq. (2.26)) also showed that $\kappa = \sqrt{n}$, which was consistent with the original postulate that κ was a property of the porous material.

As $\sigma \to 0$, both the BJ and LW boundary conditions tend towards the expected no-slip condition for an impermeable boundary.

Following others who have used the Carman-Kozeny formulation to interpret the thickness of the transition zone in terms of grain diameters. Substituting the Carman-Kozeny expression (Carman, 1937) into Eq. (2.28) yields

$$\delta\sqrt{\frac{\nu}{\omega}} \approx mD_s\frac{n}{\sqrt{180}(1-n)} \tag{2.29}$$

where $\delta\sqrt{\nu/\omega}$ on the left side is the dimensional transition zone depth and D_s is the grain diameter of the porous boundary. This shows that the value of the transition depth, which could scale either with the square root of the permeability or with the grain diameter, will be determined by the value of the empirical constant m.

2.5. Analytical solutions for LW boundary condition

Oscillatory wave case

To consider the LW boundary conditions in the oscillatory flow problem, a shifted vertical coordinate that includes the depth of the transition zone in the domain is first introduced as

$$\bar{\eta} = \eta + \delta. \tag{2.30}$$

Then, it is possible to state that $u = u_s$ at $\bar{\eta} = 0$, and the LW boundary conditions can be written as

$$u \to U \text{ as } \bar{\eta} \to \infty \tag{2.31a}$$

$$u = \mathrm{i}\sigma U \mathrm{e}^{\mathrm{i}t} \text{ on } \bar{\eta} = 0. \tag{2.31b}$$

To find a solution to the governing equation Eq. (2.6a) subject to boundary conditions Eqs. (2.31), it is assumed the solution has a separable form

$$u = \mathbb{R}[f(\bar{\eta})\mathrm{e}^{\mathrm{i}(t+\phi)}] \tag{2.32}$$

where $\mathbb{R}$ correspond to the real part and ϕ is a phase shift. Substituting Eq. (2.32) into the governing equation leads to a second order ordinary differential equation with constant coefficients

$$f''(\bar{\eta}) - \mathrm{i}f(\bar{\eta}) = -\mathrm{i}U\mathrm{e}^{-\mathrm{i}\phi} \tag{2.33}$$

that can be solved with a pair of complex roots and a particular solution $f(\bar{\eta})_p = U\mathrm{e}^{-\mathrm{i}\phi}$. The following general solution for $f(\bar{\eta})$ is obtained as

$$f(\bar{\eta}) = A\mathrm{e}^{\bar{\eta}\frac{(1+\mathrm{i})}{\sqrt{2}}} + B\mathrm{e}^{-\bar{\eta}\frac{(1+\mathrm{i})}{\sqrt{2}}} + U\mathrm{e}^{-\mathrm{i}\phi}. \tag{2.34}$$

where A and B are constants to be determined from the boundary conditions in Eqs. (2.31). $A = 0$ if the solution is to remain finite and satisfy the boundary condition as $\bar{\eta} \to \infty$. B and ϕ are found from the boundary condition at $\bar{\eta} = 0$ to be

$$B = -U\sqrt{1+\sigma^2}$$

$$\phi = -\arctan(\sigma).$$

This final solution is

$$u = U\mathrm{e}^{\mathrm{i}t}\left[1 - \sqrt{1+\sigma^2}\mathrm{e}^{-\bar{\eta}\frac{(1+\mathrm{i})}{\sqrt{2}}}\mathrm{e}^{-\mathrm{i}\arctan(\sigma)}\right]. \tag{2.35}$$

The bed shear stress can be computed via

$$\tau_b = \left.\frac{\partial u}{\partial \eta}\right|_{\eta=0}$$

which is given by

$$\tau_b = \sqrt{\frac{1+\sigma^2}{2}}\mathrm{e}^{-\mathrm{i}\arctan(\sigma)}(1+\mathrm{i})\mathrm{e}^{-\delta\frac{(1+\mathrm{i})}{\sqrt{2}}}U\mathrm{e}^{\mathrm{i}t}. \tag{2.36}$$

The vertical velocity in the boundary layer can be computed from continuity. Rearranging Eq. (2.8) gives

$$w - w_s = -\sqrt{\frac{\nu k^2}{\omega}}\int_{-\delta}^{\eta}\frac{\partial u}{\partial x}d\eta$$

where the LW boundary condition is used to ensure continuity of the fluid and Darcy velocities at the transition depth: $w = w_s$ at $\eta = -\delta$. Here, $w_s = 0$ since $\partial p/\partial\eta = 0$, and the solution for the vertical velocity is

$$w = -\frac{dU}{dx}\sqrt{\frac{\nu k^2}{\omega}}\mathrm{e}^{\mathrm{i}t}\left\{\bar{\eta} + \sqrt{\frac{1+\sigma^2}{2}}\mathrm{e}^{-\mathrm{i}\arctan(\sigma)}(1-\mathrm{i})\left[\mathrm{e}^{-\bar{\eta}\frac{(1+\mathrm{i})}{\sqrt{2}}} - 1\right]\right\}. \tag{2.37}$$

Following with the developments made before, the streaming velocity u_b, in its dimensionless form as follows

$$u_b = \sqrt{\frac{\omega}{\nu k^2}}\int_0^{\eta}\overline{uw} - (\overline{uw})_{\infty}d\eta \tag{2.38}$$

where u and w are the horizontal and vertical velocities, respectively, and the overline means the quantities are averaged in the time as

$$\overline{uw} = \frac{1}{2\pi}\int_0^{2\pi}(uw)dt. \tag{2.39}$$

The horizontal and vertical velocities u, w have been previously obtained, which are used directly in the calculations for the streaming velocity. The equation for this quantity has the following

form

$$u_b(\eta,t) = \frac{U_x^2}{4}\Bigg\{ -(1+\sigma^2) + 4\sqrt{1+\sigma^2}\cos(\arctan(\sigma)) + (1+\sigma^2)\exp(-\sqrt{2}(\eta+\delta)) + 2(1+\sigma^2)\exp(-\sqrt{2}(\eta+\delta))\sin\left(\frac{\eta+\delta}{\sqrt{2}}\right) - (1+\sigma^2)\exp\left(-\frac{\eta+\delta}{\sqrt{2}}\right)\Bigg[(\sqrt{2}(\eta+\delta)+4)\cos\left(\frac{\eta+\delta}{\sqrt{2}}+\arctan(\sigma)\right) + \sqrt{2}(\eta+\delta)\sin\left(\frac{\eta+\delta}{\sqrt{2}}+\arctan(\sigma)\right)\Bigg]\Bigg\} \quad (2.40)$$

The set of solutions for the horizontal velocity, vertical velocity, and bed shear stress (Eq. (2.35)–(2.40)) are extensions of the well-known the Stokes boundary layer with a permeable bed. Indeed, as the hydraulic conductivity vanishes $\sigma \rightarrow 0$, the classical solutions (Stokes, 1880; Batchelor, 2000; Rosenhead, 1988) are recovered.

Solitary wave case

Following the developments presented in the previous section, the effects of the permeable bed are implemented following Le Bars and Worster (2006). Similarly, inside the boundary layer at $\bar{\eta} = \eta + \delta$, the total horizontal velocity in the boundary layer must match that of the permeable bed. The boundary conditions are given by

$$u_r + u_i = \sigma u_s \ \text{ on } \bar{\eta} = 0, \quad (2.41)$$

$$u_r,\ w_r \rightarrow 0 \ \text{ as } \ \bar{\eta} \rightarrow \infty, \quad (2.42)$$

where the velocity u_i is given in Eq. (2.14) and σu_s has been already obtained in Eq. (2.25). The continuity equation including the modified vertical coordinate corresponds to

$$\frac{\partial u_r}{\partial x} + \frac{\partial w_r}{\partial \bar{\eta}} = 0. \quad (2.43)$$

By integrating Eq. (2.43), the vertical rotational velocity component can be obtained along the permeable sea bed at $\bar{\eta} = 0$. The solution for the boundary layer flows are calculated by slightly modifying the impermeable bed solution from Liu and Orfila (2004), yielding

$$u_r(x,\bar{\eta},t) = -\frac{\bar{\eta}}{2\sqrt{\pi}}\int_0^t \frac{(u_i-\sigma u_s)}{\sqrt{(t-\tau)^3}}\exp\left[-\frac{\bar{\eta}^2}{4(t-\tau)}\right]d\tau \tag{2.44}$$

and

$$w_r(x,\bar{\eta},t) = -\frac{1}{2\sqrt{\pi}}\int_{\bar{\eta}}^{\infty}\hat{\eta}\left[\int_0^t \frac{\partial(u_i-\sigma u_s)/\partial x}{\sqrt{(t-\tau)^3}}\exp\left(-\frac{\hat{\eta}^2}{4(t-\tau)}\right)d\tau\right]d\hat{\eta}, \tag{2.45}$$

where, $\hat{\eta}$ corresponds only to a variable change for integration. Furthermore, the leading order viscous shear stress can be readily calculated as

$$\tau_b(x,t) = \left.\frac{\partial u_r}{\partial \eta}\right|_{\eta=0} = \frac{1}{\sqrt{\pi}}\int_0^t \frac{\partial(u_i-\sigma u_s)/\partial\tau}{\sqrt{(t-\tau)}}d\tau. \tag{2.46}$$

Inside the boundary layer, it is of interest to look at the displacements of the horizontal water particles as it depicts the mass transport above the seabed. Following Svendsen (2006) and Liu and Orfila (2004), the net displacement of the water parcels can calculated according to the following integral expression

$$x(t) = x_0 + \int_{t_0}^{t} u(x(\tau),\tau)d\tau. \tag{2.47}$$

where u is the fluid velocity, x_0 is the initial position of the particles, t_0 is the initial time, and τ is only the integration variable for the time. The net horizontal displacement for the water particles was obtained by numerical integration of the previously computed velocities for impermeable and permeable sea beds, which are a function of time for different $\bar{\eta}$ elevations.

2.6. Numerical approximation for Beavers and Joseph (1967) boundary condition

This section presents numerical approach considered to implement the Beavers and Joseph (1967) boundary condition. The governing equation is solved for the horizontal velocity in the boundary layer numerically using finite differences and the Crank-Nicolson semi-implicit scheme. We use the BJ boundary condition at $\eta = 0$ and initialize the simulations with $u(\eta,0) = 0$.

The vertical coordinate η is discretized over a range from 0 to 10 and time is discretized such that $\Delta t/(\Delta\eta)^2 = 0.5$. Simulations were run long enough so that hat the solutions reach its stability. The oscillatory case show a period steady state value within the first two cycles allowing comparisons against the analytical solution to be made in the time span $0 < t < 2\pi$.

The numerical implementation of the Crank-Nicolson scheme to discretize the governing equation (Eq. (2.6a)) in time (n) and space (j) is presented below. The discretized equation is

$$\frac{u_j^{n+1} - u_j^n}{\Delta t} = \frac{1}{2}\left[\frac{u_{j-1}^{n+1} - 2u_j^{n+1} + u_{j+1}^{n+1}}{\Delta\eta^2}\right] + \frac{1}{2}\left[\frac{u_{j-1}^{n} - 2u_j^{n+1} + u_{j+1}^{n}}{\Delta\eta^2}\right] + \frac{C_j^{n+1} - C_j^n}{\Delta t} \quad (2.48)$$

where $C = U\mathrm{e}^{\mathrm{i}t}$ and $\beta = \Delta t/\Delta\eta^2$ corresponds to CFL number. Re-arranging terms leads to the following form

$$-\frac{1}{2}\beta u_{j-1}^{n+1} + (1+\beta)u_j^{n+1} - \frac{1}{2}\beta u_{j+1}^{n+1} - C_j^{n+1} = \frac{1}{2}\beta u_{j-1}^{n} + (1-\beta)u_j^{n} + \frac{1}{2}\beta u_{j+1}^{n} - C_j^{n}. \quad (2.49)$$

To include the BJ boundary condition (Eq. (2.26)) in the Eq. (2.49), which mathematically corresponds to a Robin-type boundary condition, a second order discretization is considered to avoid loss of accuracy. To do this, a ghost point at the border of the numerical domain is used. The implementation of LW boundary condition follows a trivial procedure, as it corresponds to a Dirichlet-type boundary condition. The discretization of the BJ boundary condition at time step n is as follows

$$\frac{u_{j-1}^n - u_{j+1}^n}{2\Delta\eta} = \lambda(u_{j+1}^n - u_{s_j}^n) \quad (2.50)$$

with $\lambda = \kappa/\sqrt{\sigma}$. Re-arranging the above equation, the following expression is obtained

$$u_{j-1}^n = u_{j+1}^n - 2\Delta\eta[\lambda(u_{j+1}^n - u_{s_j}^n)]. \quad (2.51)$$

For sake of simplicity, some of the expressions are skipped for time step $n+1$ as it is analogous to the aforementioned discretization. Including the boundary terms in Eq. (2.49), the Crank-Nicolson

scheme takes the following form

$$(1+\beta)u_j^{n+1} - \beta u_{j+1}^{n+1} = (1-\beta)u_j^n + \beta u_{j+1}^n - \beta\Delta\eta\lambda(u_{j+1}^{n+1} + u_{j+1}^n) + \beta\Delta\eta\lambda(u_{s_j}^{n+1} + u_{s_j}^n) + (C_j^{n+1} - C_j^n), \quad (2.52)$$

which is a matrix equation with a tridiagonal matrix, which is easily solved (*e.g.*, using the Thomas algorithm).

2.6.1. Oscillatory wave case

The boundary layer velocity profiles for a permeable bed at different phases of an oscillation cycle are presented in Figure (2.2). The analytical velocity profiles obtained with the LW boundary conditions (solid magenta) show very good agreement with the numerical solutions with the BJ boundary condition (black dashed line). To compare the numerical solution with the analytical solution close to the interface $\eta = 0$, time series of slip velocities and bed shear stresses are presented in Figure (2.3). Again it is observed an agreement between the analytical and numerical solutions considering LW and BJ boundary conditions, respectively, but also observe small differences. These differences can be attributed to the precise value of the constant m that effectively sets the thickness of the transition zone until the flow is well described by Darcy's law.

Figure (2.4) shows how flow at the interface varies with the dimensionless permeability σ. The maximum value of the slip velocity is shown in panel (a), the maximum bed shear stress value in panel (b), with their respective phase lags in panels (c) and (d). As permeability increases, the slip velocity magnitude increases and the bed shear stress magnitude decreases since the flow encounters lower resistance. The phase lags are less sensitive to the permeability compared with the magnitudes.

The results of the analytical solution for the streaming velocity are shown in Figure (2.5). Profiles present magnitudes that are proportional to the hydraulic conductivity σ. It is possible to notice the significant difference in magnitude at the interface $\eta = 0$, compared to the magnitudes of considering a no-slip boundary condition. Profiles exhibit maximum magnitudes at certain

specific η, reaching higher streaming velocities at vertical coordinates closer to the boundary as the permeability increases. This behavior indicates a relation to the slip velocity, which increases as the sea bed becomes more permeable. On the other hand, average streaming velocity displays rapid variations in magnitude as the hydraulic conductivity augments (Figure (2.6)). This behavior of the streaming velocity is relevant to the study and analysis of sediment and mass transport.

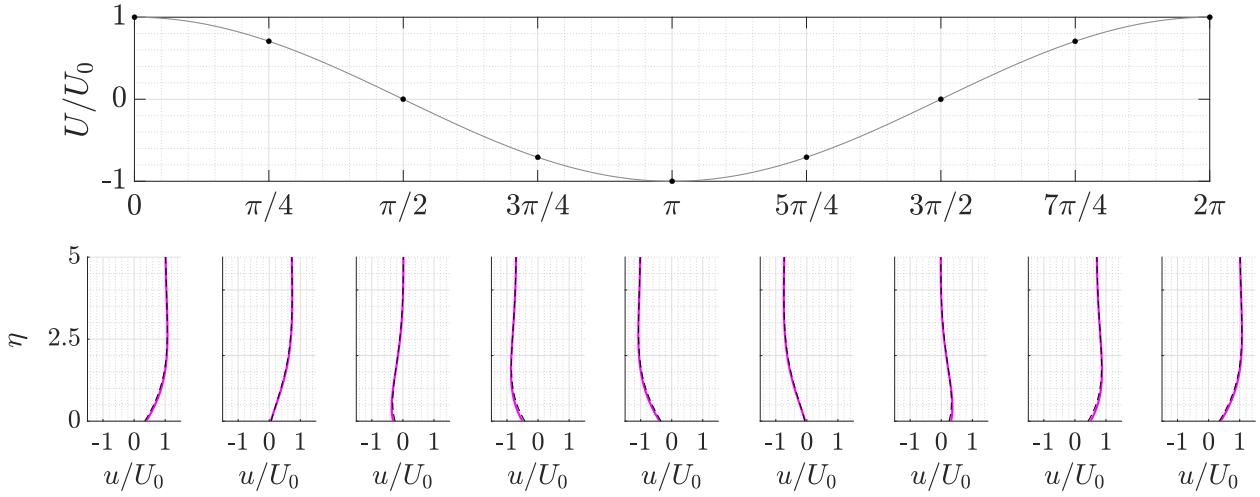

Figure 2.2: Velocity profiles for a permeable bed condition for $\sigma = 0.1$ and $U_0 = 1$, and $m = 1$. Top: Free-stream velocity. Bottom: LW boundary condition (analytical solution: solid magenta line), BJ boundary condition (numerical solution: black dashed line).

2.6.1.1 Comparisons with laboratory data

Analytical solutions against experimental data reported in Liu et al. (1996) are compared to show the validity of the theory proposed in this work. In the experiments, surface gravity waves propagate over a permeable bed generating an oscillatory boundary layer. The experimental cases are listed in Table (2.1), which gives values for the water depth h, wave amplitude a, wave period T, the dimensionless hydraulic conductivity σ measured using a constant-head permeator, the porosity n, and the dimensionless wave steepness ka and dimensionless wavelength kh calculated using the wavenumber k from the dispersion relation. From linear wave theory, the dimensionless

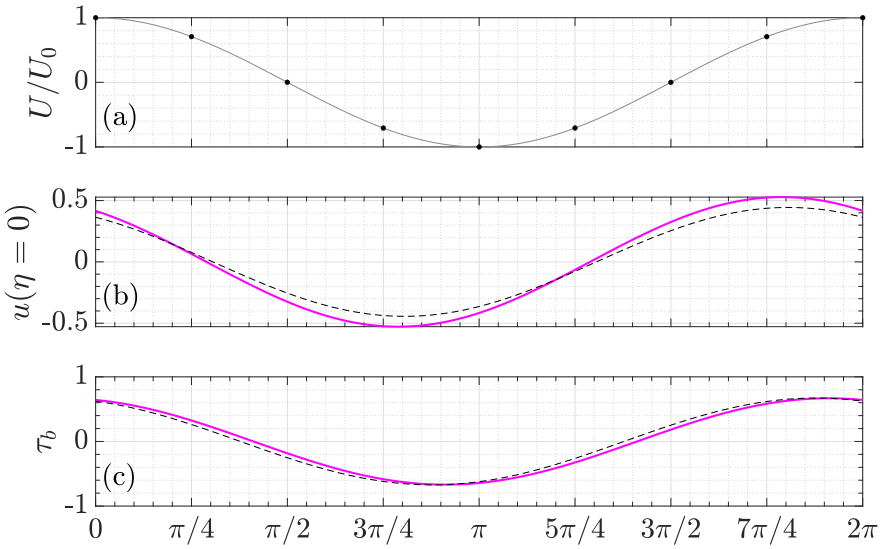

Figure 2.3: Slip velocity and shear stress at the interface ($\eta = 0$) for $\sigma = 0.1$ and $U_0 = 1$. Top: Free-stream velocity. Middle: LW boundary condition (analytical solution: solid magenta line), BJ boundary condition (numerical solution: black dashed line). Bottom: Bed shear stress. LW boundary condition (analytical solution: solid magenta line), BJ boundary condition (numerical solution: black dashed line).

Table 2.1: Experimental data from Liu et al. (1996).

Group	Exp.	$D_s \times 10^{-3}(m)$	a (cm)	h (cm)	T (s)	σ	n	ka	kh
2	A2	0.5	0.517	19.9	1.254	0.0012	0.3830	0.0203	0.7801
3	A3	1.5	0.512	19.9	1.254	0.0090	0.3824	0.0201	0.7801
4	A4	3.0	0.515	19.9	1.254	0.0373	0.3840	0.0202	0.7801
2	B2	0.5	0.537	24.0	1.114	0.0013	0.3830	0.0227	1.0141
3	B3	1.5	0.513	24.0	1.114	0.0102	0.3824	0.0217	1.0141
4	B4	3.0	0.522	24.0	1.116	0.0419	0.3840	0.0220	1.0117
2	C2	0.5	1.181	24.7	1.035	0.0014	0.3830	0.0545	1.1396
3	C3	1.5	1.167	24.7	1.033	0.0109	0.3824	0.0540	1.1426
4	C4	3.0	1.140	24.7	1.035	0.0452	0.3840	0.0526	1.1396

free-stream velocity that drives the boundary layer is given by

$$U = \frac{ka}{\sinh kh} \mathrm{e}^{-\mathrm{i}(x-t)}.$$

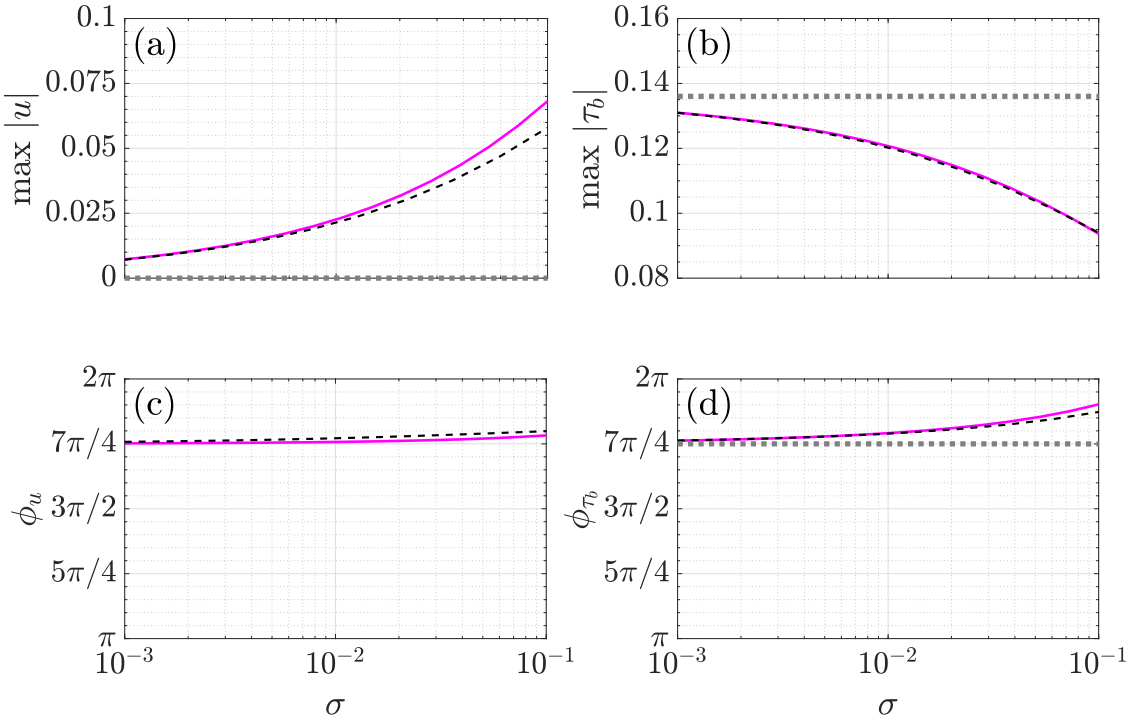

Figure 2.4: Top: Variation of the maximum slip velocity (a) and bed shear stress (b) as functions of σ, with $U_0 = 1$. Bottom: Variation of the phase associated to the maximum slip velocity (c) and bed shear stress (d) for different values of σ. Grey line: No-slip boundary condition (analytical solution). Magenta line: LW boundary condition (analytical solution with m = 1). Black dashed line: BJ boundary condition (numerical solution).

This wave-induced flow can be considered to be uniform inside the boundary layer and the flow in the permeable bed (below the transition zone) can be considered to be well modeled by Darcy's law. Thus, the experimental conditions are ideally suited to test our analytical solutions, which can be found by substituting $U = \mathrm{e}^{-\mathrm{i}x}$ into Eq. (2.35)–(2.37). The horizontal velocity solution is given by

$$u = U_0 \left\{ \cos(x-t) - \sqrt{1+\sigma^2}\cos\left(x - t + \frac{\eta+\delta}{\sqrt{2}} + \arctan(\sigma)\right)\mathrm{e}^{-\frac{\eta+\delta}{\sqrt{2}}} \right\} \tag{2.53}$$

where

$$U_0 = \frac{ka}{\sinh kh}.$$

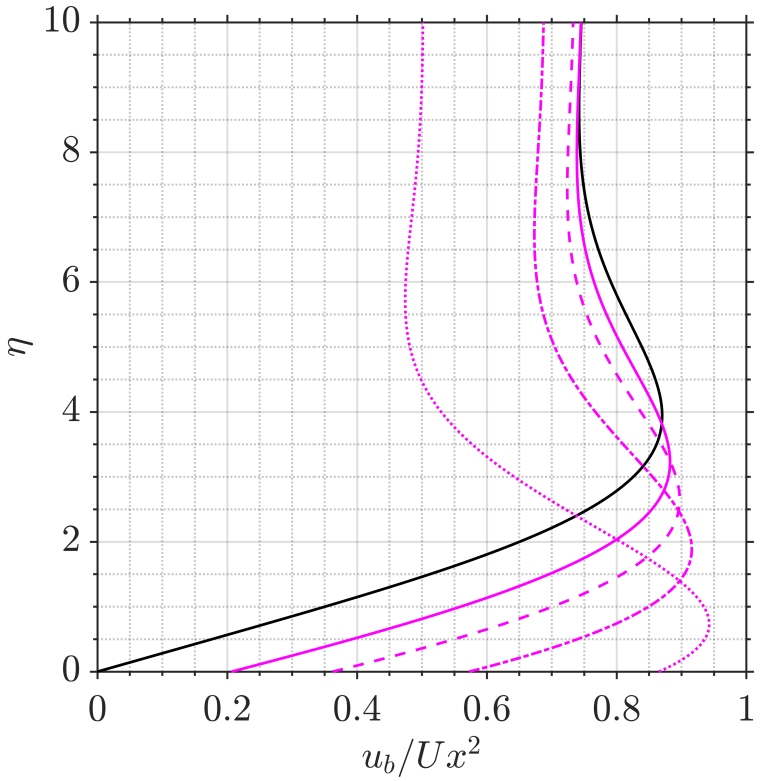

Figure 2.5: Left: Streaming velocities profiles for different values of σ, with $U_0 = 1$. Black line: No-slip boundary condition (analytical solution). Magenta lines: LW boundary condition (analytical solution with m = 1). $\sigma = 0.1$ (Solid line), $\sigma = 0.25$ (dashed line), $\sigma = 0.5$ (dash-dotted line), $\sigma = 1.0$ (dotted line). Right: Variation of the average streaming velocity between $\eta = [0, 10]$ for variable permeability σ. Black line: No-slip boundary condition (analytical solution). Magenta line: LW boundary condition (analytical solution with m = 1).

As before, the above expression reduces to the expected impermeable bed solution (Svendsen, 2006) as $\sigma \to 0$.

Figure (2.7) shows the comparison between the analytical solution and experimental data. Here, the parameter m plays an important role because it determines the depth of the transition zone below the interface and essentially controls the magnitude of the slip velocity. Rather than tuning the value of m for each experimental case, the comparisons by taking a single value of m for the experiments where the porous medium presents the same characteristics in permeability and porosity (groups 2, 3, and 4) are shown. The agreement between the data and the theoretical

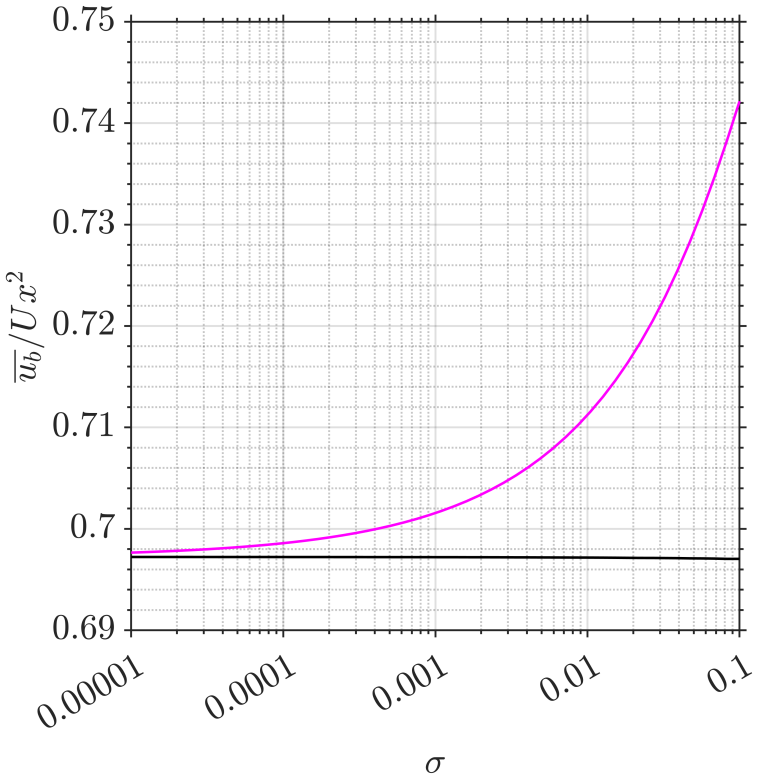

Figure 2.6: Left: Streaming velocities profiles for different values of σ, with $U_0 = 1$. Black line: No-slip boundary condition (analytical solution). Magenta lines: LW boundary condition (analytical solution with m = 1). $\sigma = 0.1$ (Solid line), $\sigma = 0.25$ (dashed line), $\sigma = 0.5$ (dash-dotted line), $\sigma = 1.0$ (dotted line). Right: Variation of the average streaming velocity between $\eta = [0, 10]$ for variable permeability σ. Black line: No-slip boundary condition (analytical solution). Magenta line: LW boundary condition (analytical solution with m = 1).

developments of this work proposed is remarkable, especially given that a more detailed matched asymptotic solution in Liu et al. (1996) was much less successful.

In order to extend the analysis, an error estimation was performed considering the averaged Root Mean Squared Error (RMSE) across the experimental cases of groups 2, 3, and 4 shown in Figure (2.7). From the analysis, it is found the optimum value of m, for which the error is minimum. From Figures (2.8, 2.9 and 2.10) it is possible to visualize the performance of the matching condition of this theory compared to the experiments for different values of the parameter m. In

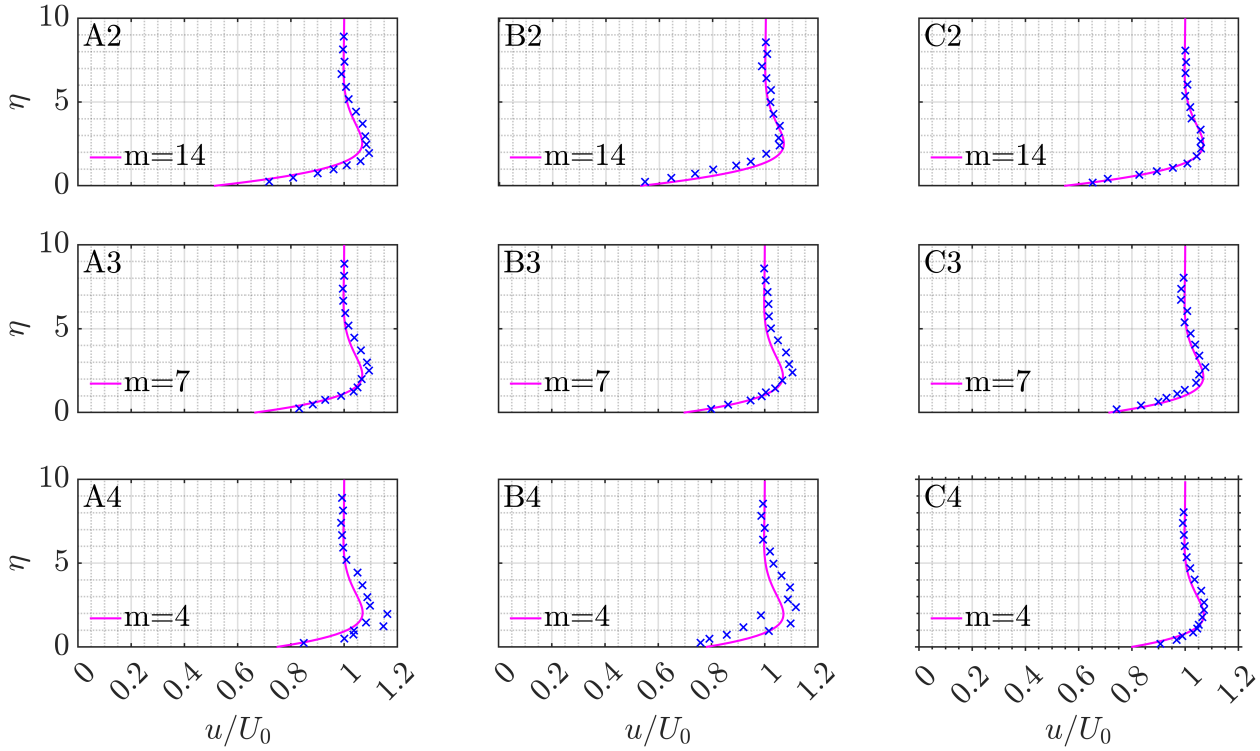

Figure 2.7: Dimensionless velocity profiles at $x - t = 2\pi$ (under the wave crest) for the different cases listed in Table (2.1), showing a comparison between the LW analytical solution (solid magenta line) and experimental data (Liu et al., 1996) (blue crosses). Groups: 2 (Top), 3 (Middle), 4 (Bottom).

general, the errors associated with the selected values of m for each group are lower compared with the literature.

From Eqs. (2.28) and (2.29), it is observed that the thickness of the transition zone is proportional to both $\sqrt{\sigma}$ or D_s. From the empirical data, it is found that a value of $m = 14, 7$ and 4 gives good agreement across different groups of oscillatory flow conditions and permeable beds, and thus, the transition zone thickness remains almost invariant for different oscillatory flow conditions. In terms of the grain diameter it is

$$\delta\sqrt{\frac{\nu}{\omega}} = [0.69, 0.32, 0.19]D_s, \tag{2.54}$$

and in terms of the permeability it is

$$\delta = [22.62, 11.32, 6.45]\sqrt{\sigma}. \tag{2.55}$$

The above expressions show different orders of magnitude when the different scales apply, which agrees with previous data (Goharzadeh et al., 2005; Morad and Khalili, 2009; Liu and Prosperetti, 2011). Since the scaling with grain diameter is closer to a value of 1 than the scaling with the permeability, results suggest the grain diameter to be a more suitable characteristic length for the transition zone. Different from other studies, this conclusion is obtained indirectly by using the empirical parameter m in relation to the boundary layer in the free fluid.

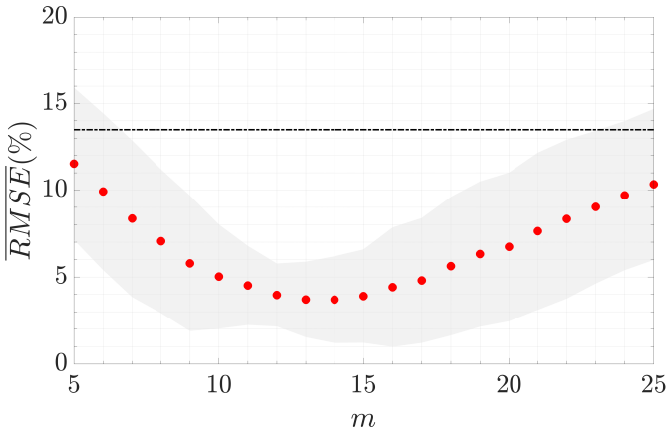

Figure 2.8: Average RMSE of velocity magnitudes for different values of m (red dots) compared to Liu et al. (1996) theoretical solution (black dash-dotted line). Errors calculated on Group 2 experimental data.

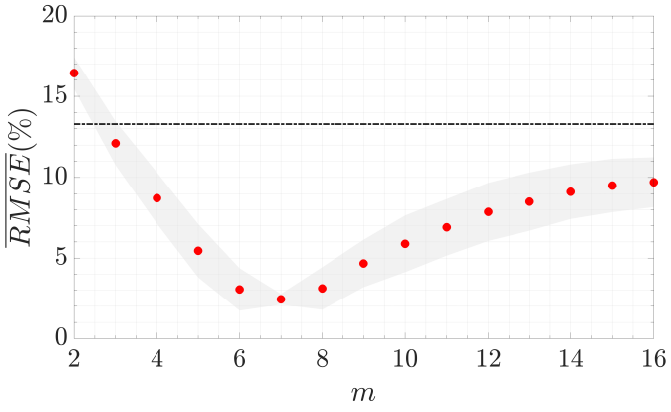

Figure 2.9: Average RMSE of velocity magnitudes for different values of m (red dots) compared to Liu et al. (1996) theoretical solution (black dash-dotted line). Errors calculated on Group 3 experimental data.

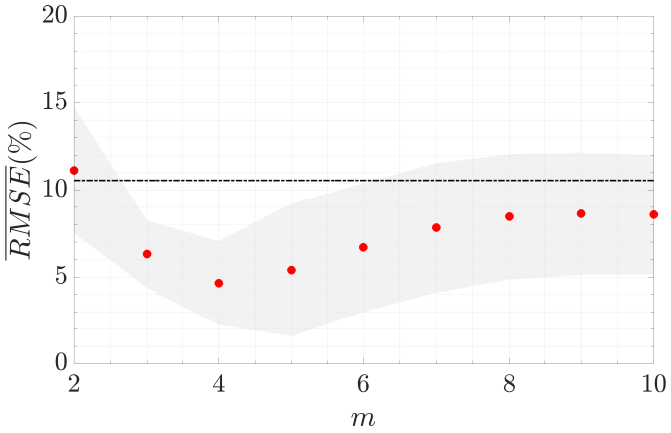

Figure 2.10: Average RMSE of velocity magnitudes for different values of m (red dots) compared to Liu et al. (1996) theoretical solution (black dash-dotted line). Errors calculated on Group 4 experimental data.

A single value $m = 5$ is tried in the analytical solution to compare against the empirical data (Figure (2.11). Results show that even when a single parameter can give a good agreement for some experimental cases, it is enough to characterize the oscillatory boundary layer flows for permeable beds with slightly different characteristics, such as porosity and hydraulic conductivity. For a value of $m = 5$, the dimensional transition zone is

$$\delta\sqrt{\frac{\nu}{\omega}} = 0.24D_s \pm 0.01D_s, \tag{2.56}$$

which, expressed in terms of the permeability gives the relation

$$\delta = 8.08\sqrt{\sigma} \pm 0.01\sqrt{\sigma}. \tag{2.57}$$

2.6.2. Solitary wave case

Evaluations of integrals and numerical simulations have been performed to assess the behavior of the solitary wave-induce boundary layer equations. For convenience, a moving coordinate $\xi = x - Ct$ is introduced in the results, which acts as time when $x = 0$ (Liu and Orfila, 2004; Liu et al., 2007a).

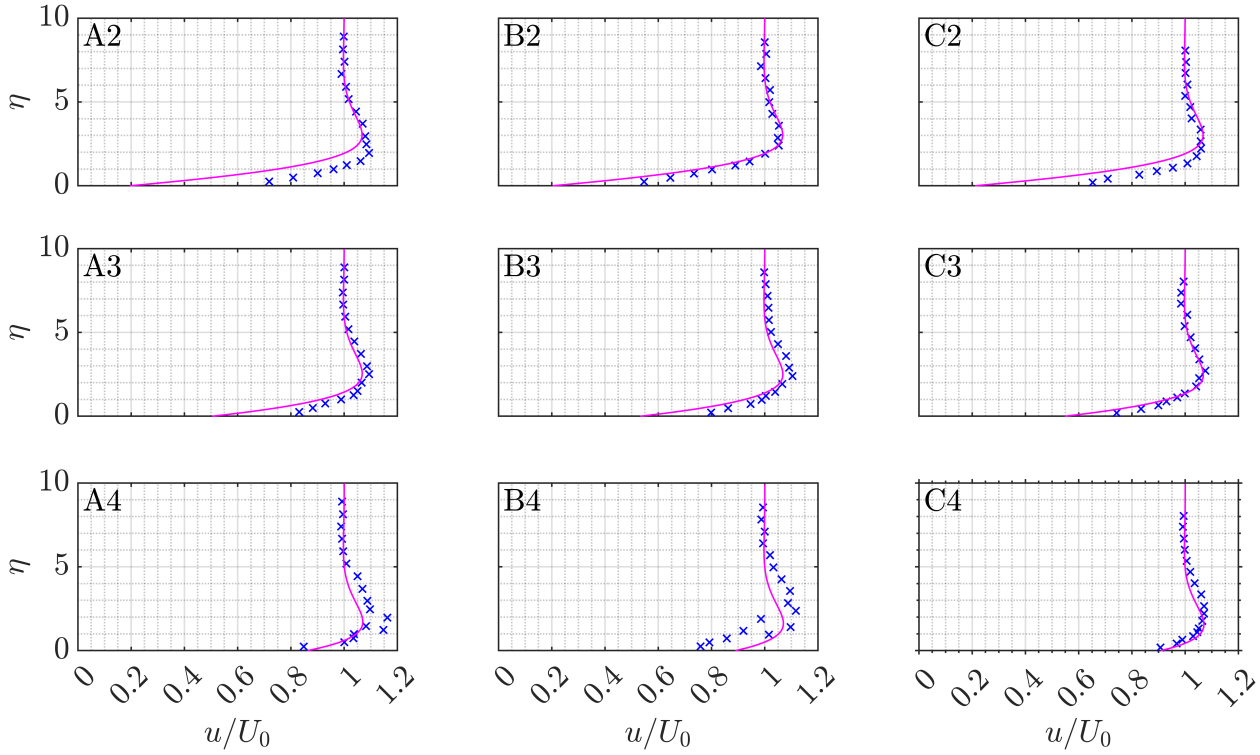

Figure 2.11: Dimensionless velocity profiles at $x - t = 2\pi$ (under the wave crest) for the different cases listed in Table (2.1), showing a comparison between the LW analytical solution, with a fixed value $m = 5$ (solid magenta line) and experimental data (Liu et al., 1996) (blue crosses). Groups: 2 (Top), 3 (Middle), 4 (Bottom).

Figures (2.12) and (2.13) show the time series of horizontal velocities and rotational vertical velocity associated with a non-linearity parameter $\epsilon = 0.2$ and hydraulic conductivity $\sigma = 0.0311$ ($K' = 0.5$ (m/s)) at different elevations of η. In general, velocities present acceleration and deceleration on the permeable bed, which start vanishing as it moves outside the boundary layer. When the solitary wave moves in the positive x direction, fluxes present positive values, changing the sign in the deceleration process. This can also be observed in Figure (2.14a) where the time series of velocities at $\eta = 0$ show that the magnitude of u is proportional to the hydraulic conductivity. It is noticed that reversal flows are lower than accelerating flows. In the same way, the bed shear stress also present a significant variation in its magnitude as σ increases (Figure (2.14b)). However,

this magnitude decreases with the hydraulic conductivity. This physical effect happens as a reduction of the friction at the interface as the slip velocity increases. In general, this quantity presents positive values during the acceleration process of the solitary wave, which are significantly higher than the reversal stresses.

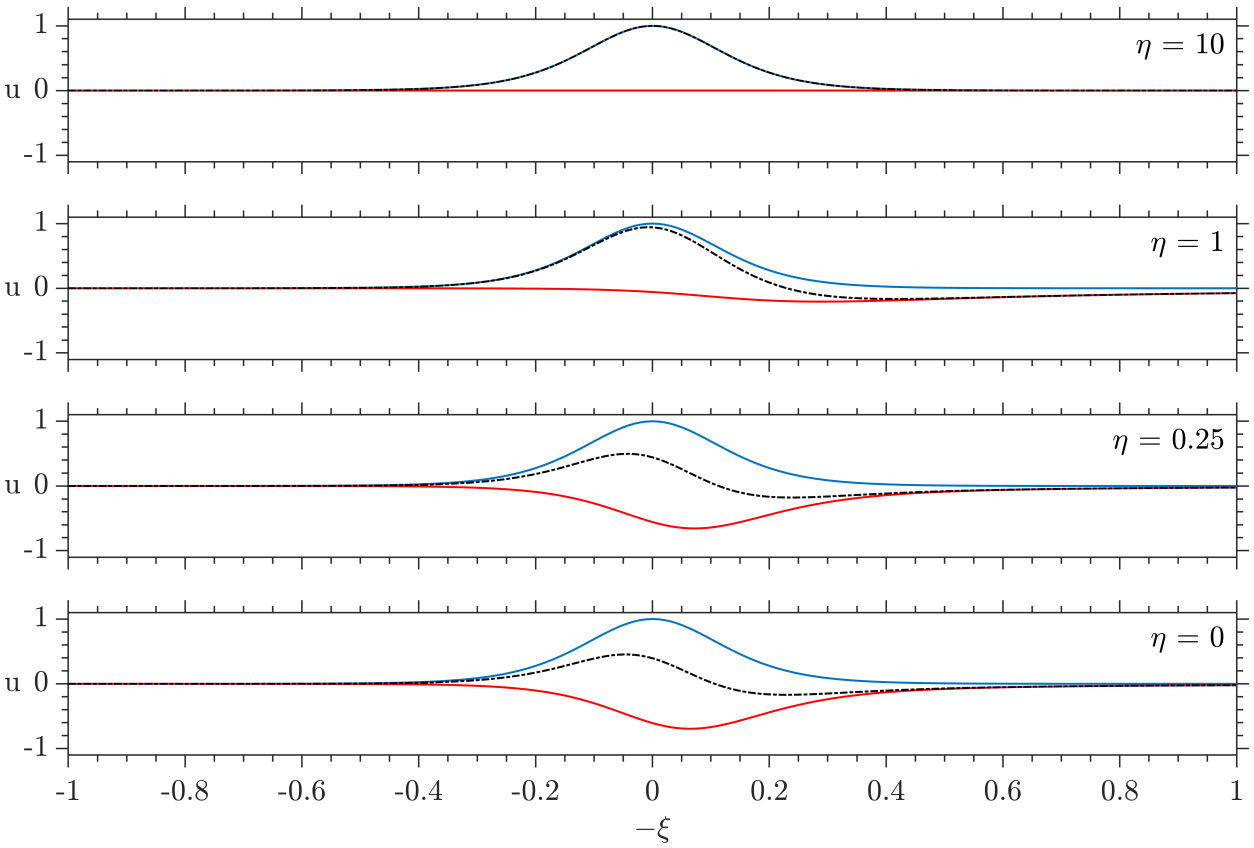

Figure 2.12: Horizontal velocity for a permeable bed (LW boundary condition). $\epsilon = 0.2$ and $\sigma = 0.0311$ ($K' = 0.5$ (m/s)). u_i (solid gray line), u_r (dash-dotted orange line), u_r (dotted gray line).

The analytical and numerical results are also assessed to check the performance of the methods and boundary conditions for the solitary wave. Figure (2.15) shows the velocity profiles solved numerically (BJ) and analytically (LW) for different phases of the transient solitary wave for $\epsilon = 0.2$ and $\sigma = 0.0311$. To make the solutions comparable, a value of $m = 1$ was used in the analytical LW solution, for which the results of both boundary conditions must behave similarly. Profiles present similar results displaying small differences at the interface $\eta = 0$. This difference is

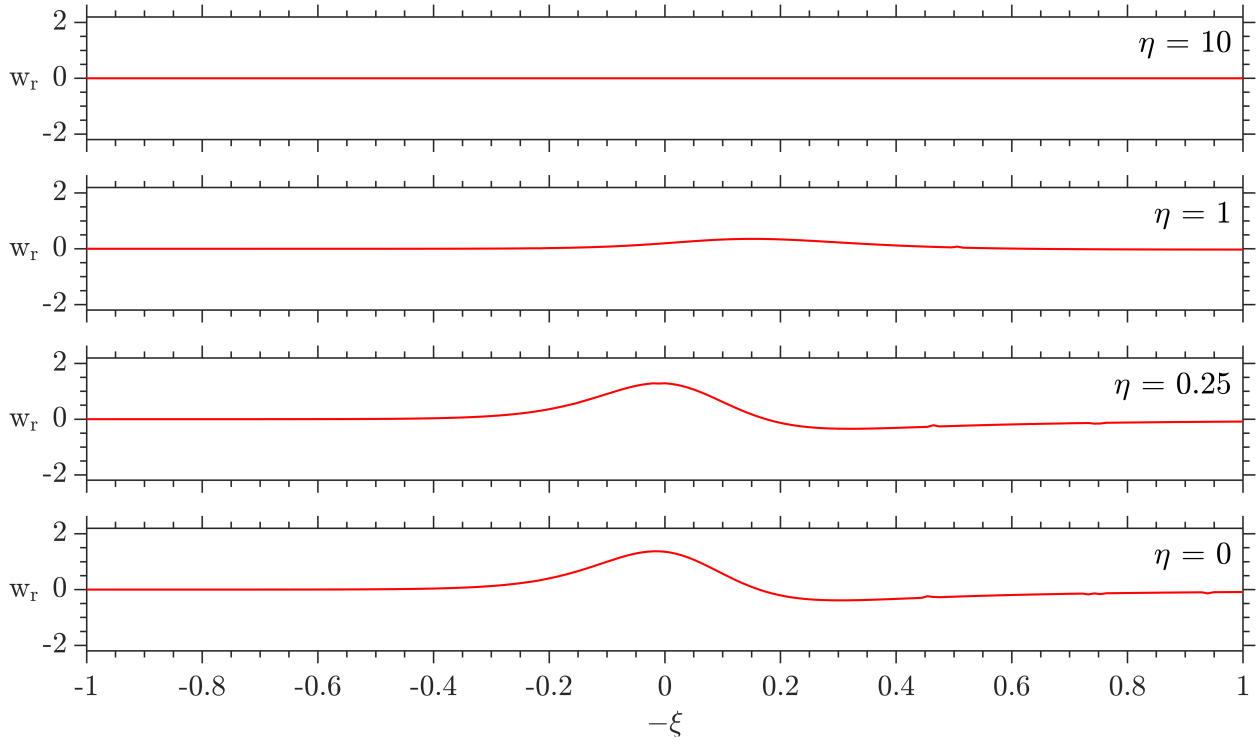

Figure 2.13: Rotational vertical velocity w_r (LW boundary condition), for different elevations of the boundary layer η. $\epsilon = 0.2$ and $\sigma = 0.0311$ ($K' = 0.5$ (m/s)).

attributed to numerical numerical error, which could be improved by increasing the time resolution for the numerical solution. The differences at the interface were found to be $\sim 14\%$. Figure (2.16) shows the velocity profiles considering the Le Bars and Worster (2006) boundary condition only at different points along the solitary wave signal for different values of the hydraulic conductivity σ. As expected, variations on the velocity structure are associated with σ, which increase near the boundary. Reversal flows seem to decrease faster along the vertical coordinate η with increasing values of σ.

The influence of the permeable sea beds on the net horizontal displacements of water parcels is evaluated against the impermeable case. Figure (2.17) presents the water parcel displacements in time at different elevations η = [0.25, 1.0, 10]. For elevations closer to the boundary, curves show how the displacements increase with the conductivity of the permeable bed. As the rotational velocity component modifies its structure at the interface and within the boundary layer, modifying

also the total velocity, displacements are prone to increase close to the boundary, different from an impermeable scenario. In the outer regions of the boundary layer, the contribution of the porous material decays, and the rotational velocity vanishes, reaching similar displacements despite magnitude of the hydraulic conductivity. It is observed that the curves are always positive, indicating the low contribution of the reversal flow inside the boundary layer, especially close to the boundary. Further, water particles present higher displacements in distances far from the boundary $\eta = 0$.

Figure (2.18) presents the distribution of the maximum horizontal displacements for different η and σ. It is possible to notice that for elevations (η) closer to the boundary the displacements tend to increase with the hydraulic conductivity, pointing to the influence of the permeable seabed on the boundary layer velocities and thus on the horizontal displacements. On the other hand, displacements tend to reach a constant magnitude far from the boundary, regardless of the values of σ.

2.7. Concluding remarks

Analytical solutions for oscillatory boundary layers over a permeable bed have been found and compared against numerical solutions and experimental data. The boundary conditions at the interface between the fluid and permeable bed represent the biggest source of uncertainty in such a scenario. In the presented numerical simulations, the well-known Beavers and Joseph (1967) boundary condition was implemented. The analytical solutions, which consider the Le Bars and Worster (2006) boundary condition, show how the boundary layer structure depends on the dimensionless hydraulic conductivity $\sigma = K'\omega/g'$, with the solutions recovering the well-known impermeable bed Stokes boundary layer in the limit $\sigma \to 0$. Further, these solutions agree well with numerical solutions in terms of the velocity profiles, slip velocities, and wall shear stresses. The solutions also agree well with experimental data of an oscillatory boundary layer driven by surface waves propagating over a bed of solid spheres. The analytical solutions contain an $\mathcal{O}(1)$ empirical parameter, whose value is constrained with the use of experimental data. It was found that, physically, this parameter controls the thickness of the transition zone below which the flow

dynamics are dominated by Darcy's law. The results agree with previous literature on steady flows that the transition zone thickness is on the order of 1 grain diameter. The boundary conditions were also implemented to extend the Liu and Orfila (2004) formulations for boundary layers induced by a transient solitary wave over impermeable sea beds, which have also been solved analytically and numerically. Results show that the permeability conditions of the porous region modifies the structure of the rotational velocity in the boundary layer, and thus, the total velocity. As expected, velocities are shown to be proportional to the hydraulic conductivity. An interesting finding corresponds to the net horizontal displacements for water parcels, which have the potential to modify the mass transport in the boundary layer. Net displacements show that close to the boundary, the effects of a permeable sea bed contribute to higher displacements, being proportional to the conductivity, while outside the boundary layer, the permeability becomes less important, reaching a constant displacement regardless of the permeability conditions.

Future research on this matter could extend the physical insights from the results presented in this work to various applications in coastal engineering and oceanography such as water wave damping (Putnam, 1949; Reid and Kajiura, 1957; Liu, 1973; Liu and Dalrymple, 1984), mass exchange, and sediment transport in both laminar and turbulent conditions (Liu, 1977; Conley and Inman, 1994; Corvaro et al., 2014), and wave-driven canopy flows (Luhar et al., 2010; Webber and Huppert, 2020, 2021).

An specific extension of the developments presented in this work could include performing new experiments increasing the range of hydraulic conductivities to obtain a wide range of specific m parameter. These findings could contribute to reducing uncertainties in the selection of this empirical parameter when specific conductivities are required. In the same way, an inverse problem can be proposed to obtain the empirical parameter m prior to its calibration by knowing the properties of the porous material.

Following the same line of research, the physics of the boundary conditions presented in this work can be suitable to model the top boundary condition in the analysis of transient wave-induced flows inside permeable bed flows.

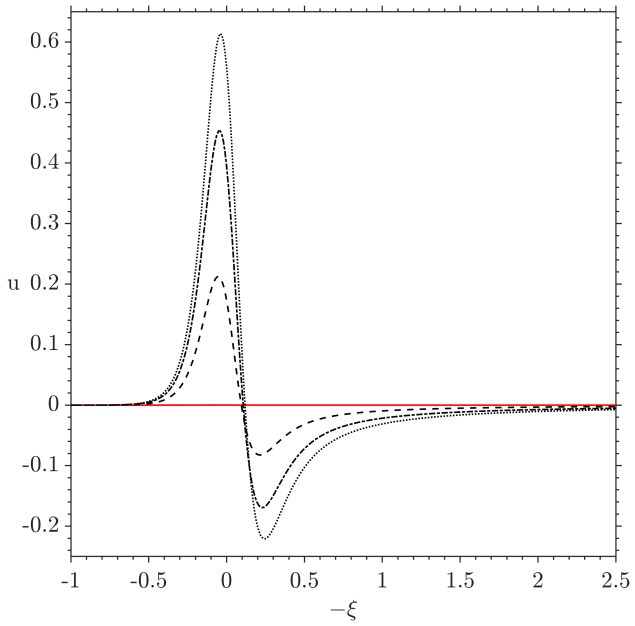

(a)

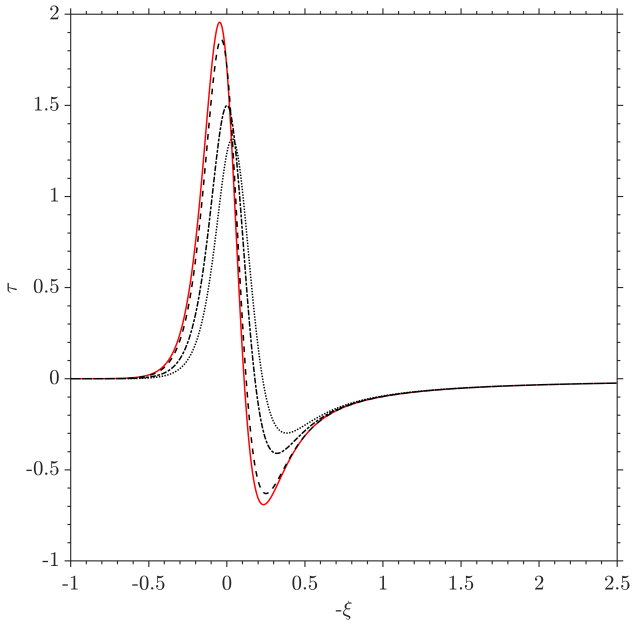

(b)

Figure 2.14: (a) Time series of velocities, u, and (b) bed shear stresses, τ, with $\epsilon = 0.2$ (LW boundary condition). Impermeable condition (red solid line), $\sigma = 0.0062$ ($K' = 0.1$ (m/s)) (black dashed line), $\sigma = 0.0311$ ($K' = 0.5$ (m/s)) (black dash-dotted line), $\sigma = 0.062$ ($K' = 1.0$) (m/s)) (black dotted line).

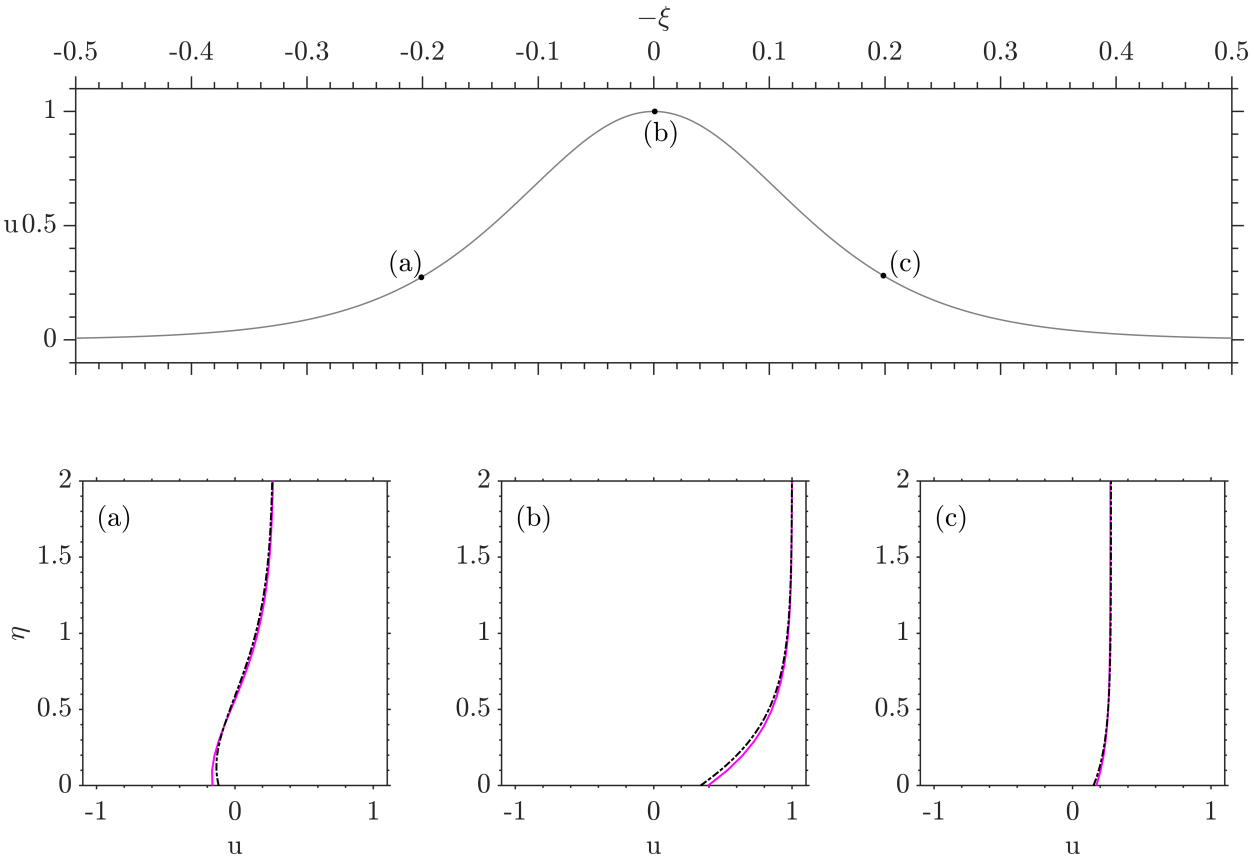

Figure 2.15: Velocity profiles for different locations along the solitary wave signal. LW boundary condition (analytical results: solid magenta line). BJ boundary condition (numerical results: dash-dotted black line). $\epsilon = 0.2$ and σ =0.0311 ($K' = 0.5$ (m/s)).

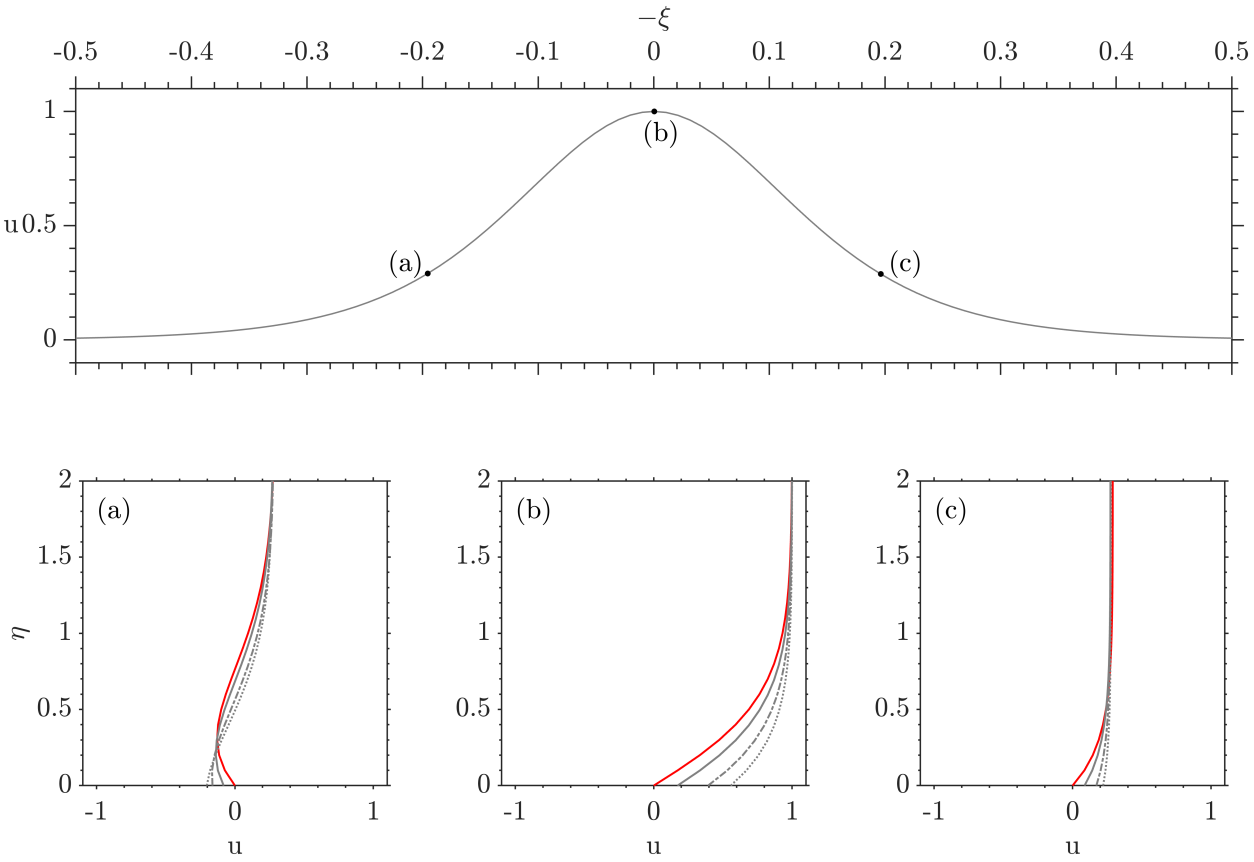

Figure 2.16: Velocity profiles for $\epsilon = 0.2$ (LW boundary condition) for different values of hydraulic conductivity. Impermeable condition (red solid line), $\sigma = 0.0062$ ($K' = 0.1$ (m/s)) (gray solid line), $\sigma = 0.0311$ ($K' = 0.5$ (m/s)) (gray dash-dotted line), $\sigma = 0.062$ ($K' = 1.0$) (m/s)) (gray dotted line).

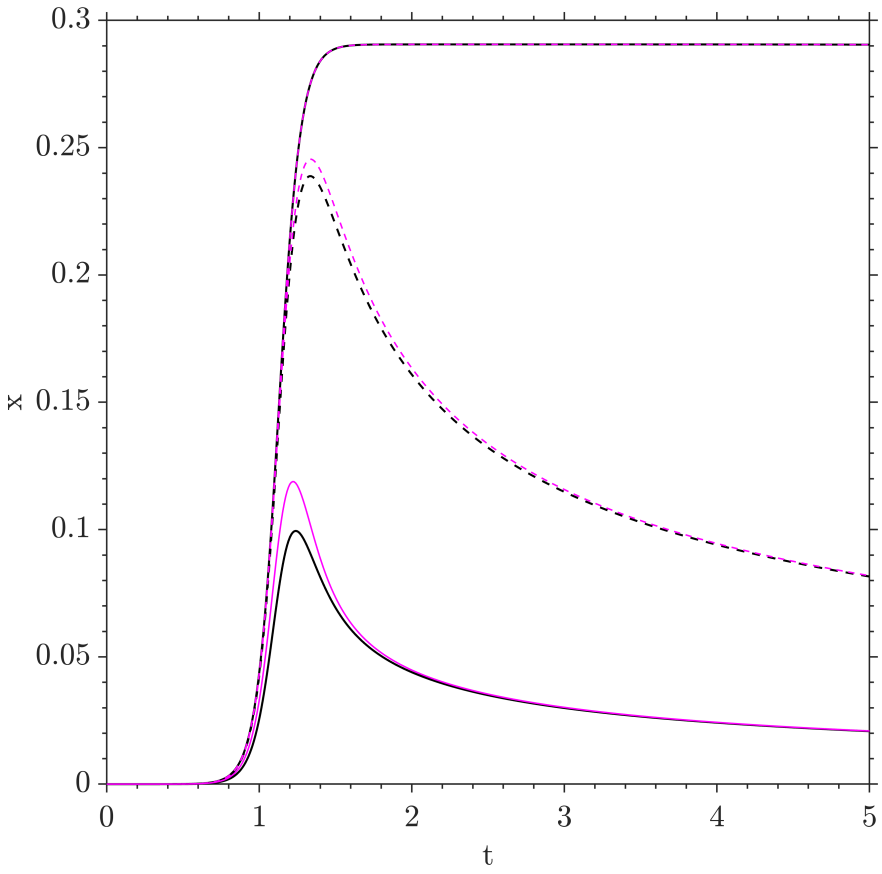

Figure 2.17: Net horizontal water particles displacements for $\epsilon = 0.2$ at different η elevations. Impermeable sea bed (black line), and permeable sea bed with $\sigma = 0.0311$ ($K' = 0.5$ (m/s)) (magenta line). $\eta = 0.25$ (solid lines), $\eta = 1.0$ (dashed lines), and $\eta = 10$ (dotted-dashed lines).

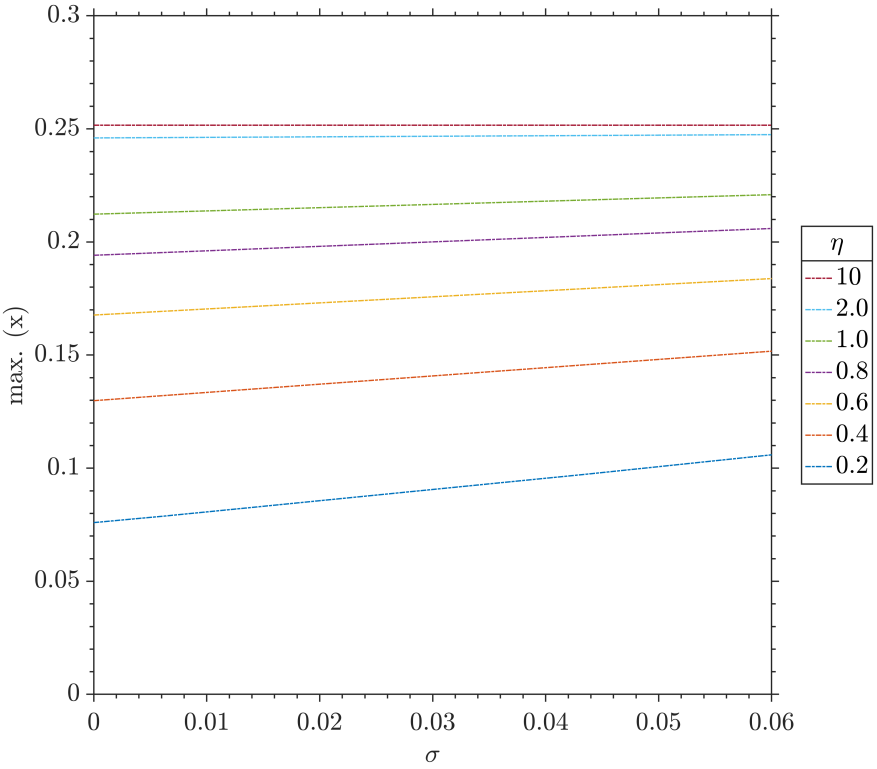

Figure 2.18: Maximum net horizontal water particles displacements for several values of σ. $\epsilon = 0.2$ (LW analytical solution).

Chapter 3

HYDRODYNAMICS OF WAVE-SWASH INTERACTIONS

3.1. Introduction

Water waves continuously shape sandy coastlines through sediment transport across a wide range of timescales, from sediment suspension events caused by individual waves to beach morphology changes that occur over seasons or longer (e.g., Martínez et al. (2018); Toimil et al. (2020)). Hydrodynamically, waves transformation near the coast is classified into several subregions such as the surf zone and swash zone (Dean and Dalrymple, 2004; Holthuijsen, 2007; Jackson and Short, 2020). In the swash zone, flow begins with the shoreward acceleration of the shoreline with the arrival and collapse of each wave, and is characterised by the movement of water up and down the beach, delimited by a cycle of upwash and backwash, otherwise referred to as a swash event (Brocchini and Baldock, 2008). In particular, wave-swash interactions are events where incoming waves collide with the upwash or backwash flows of the previous swash event. Wave-swash interactions have been qualitatively described in the field (e.g., Hughes and Moseley (2007); Erikson et al. (2005)) and hypothesized to be an important mechanism for sediment transport (e.g., Puleo et al. (2000); Elfrink and Baldock (2002); Puleo and Butt (2006); Alsina et al. (2009); Puleo and Torres-Freyermuth (2016)) for some time.

The qualitative descriptions and types of wave-swash interactions include: (a) Wave-upwash interactions, where the upwash flow of a wave catches the upwash flow of the previous wave; (b) Weak wave-backwash interactions, where the upwash flow of a wave catches with the backwash flow of the previous wave, with the result that the flow is again pushed shoreward; and (c) Strong wave-backwash interactions, which are physically similar to weak wave-backwash interactions, but

with result that the interaction induces a stop or receding of the incoming flow, often accompanied by a stationary hydraulic jump. In many field scenarios, the development of 'free swash events' (no interactions) tend to occur on the upper beach, whereas wave-swash interactions are common in the lower beach. For an incident wave train with constant wave heights, the time between wave crests relative to the timescale of the swash event has been used to understand these interactions (Baldock and Holmes, 1999; Lo et al., 2013; Pujara et al., 2015b), but this has been insufficient to understand the broad class of wave-swash interactions observed in the field for irregular waves (Chardón-Maldonado et al., 2016). Chen et al. (2023), in their recent extensive review of sediment transport models, concluded that even though there is an acceptance that wave-swash interactions play a critical role in the sediment transport in the swash zone, there are no parameters to determine the interaction type or the resulting sediment transport.

Controlled experiments are developed in a wave flume to find quantitative descriptions of wave-swash interactions. The methodology presented here considers the generation solitary waves since they travel with a permanent form (ignoring small viscous losses Liu et al. (2007b)) and generate large swash events whose properties can be understood in terms of a small set of input parameters (Pujara et al., 2015a). By generating two consecutive solitary wave events, we can set the strength of the first swash event through the wave height of the first wave and set the wave height and arrival time of the second wave through its height and separation from the first wave, thereby providing full control of the wave-swash interaction.

This approach complements previous experiments using regular waves, bi-chromatic waves, solitary waves, and dam-break bores to understand and flow and transport in the swash zone (Alsina et al., 2009; O'Donoghue et al., 2010; Sou and Yeh, 2011; Alsina et al., 2012; Kikkert et al., 2012; Lo et al., 2013; Pujara et al., 2015b; Alsina et al., 2016; O'Donoghue et al., 2016; Alsina et al., 2018; Wu et al., 2021; Barranco and Liu, 2021; Pintado-Patiño et al., 2021). By mimicking the interactions observed in the field, we analyze the main kinematic properties of wave-swash interactions, focusing in particular on the vertical accelerations and their correlation with the flow

evolution. We find that there are large upward-directed vertical accelerations for certain interactions that cluster together when mapped onto two dimensionless parameters that can also predict different wave-swash interaction types.

3.2. Laboratory Experiments

3.2.1. Wave Flume Setup

Experiments were conducted in a wave flume at the Water Science and Engineering Laboratory (WSEL) of the University of Wisconsin-Madison (Figure 3.1). The WSEL flume (39 m length, 0.9 m width, and 1.1 m height) is equipped with a piston-type wavemaker controlled by AwaSys (Aalborg University, Denmark) at one end and an impermeable smooth beach with slope 1:10 at the other end. The water depth was kept constant throughout the experiments at $h = 0.3$ m. Swash events and wave-swash events were generated using solitary waves. We place the origin of the lab coordinate system at a distance of 23.5 m from the wave paddle at the still water line (SWL) on the beach with x pointing onshore and z pointing upwards against gravity.

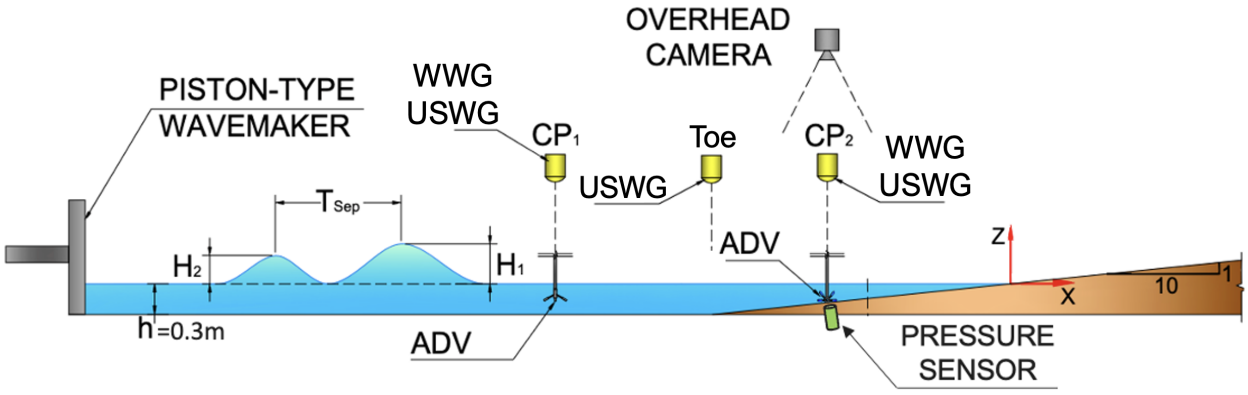

Figure 3.1: Wave flume definition sketch with locations of the different sensors.

Measurements of both the free-surface displacement ζ and the flow velocity (u, v, w) were taken at two control points, one in a constant depth at $x = -8.83$ m (CP_1) and one in the wave-swash interaction zone at $x = -0.3$ m (CP_2), and additional measurements of the free-surface displacement were taken at the toe of the beach ($x = -3$ m). The free-surface displacement

was measured at CP_1 and CP_2 using ultrasonic acoustic wave gauges (USWG; Senix ToughSonic-3 with 1 mm accuracy) and wire wave gauges (WWG, HR Wallingford with 0.1 mm accuracy) whereas only an ultrasonic wave gauge was used at the beach toe. The WWG calibration is prone to drift and thus the WWGs were calibrated at the start of every day when experiments were run whereas the USWG calibration is much more stable and only required calibration once before the start of the experiments. While both sensor types can be expected to give reliable data in the offshore regions where the wave slopes are mild, the WWG has better accuracy and is able to reliably measure the free-surface displacement with steep wave slopes due to wave breaking at CP_2 that the USWG is unable to measure. However, the WWG has a non-linear calibration response for shallow depths ($(\eta + h_{CP_2}) \leq 2$ cm), so data below this threshold water depth was removed, where $h_{CP_2} \sim 3$ cm. In the analysis below, we use the WWG data at CP_1 and CP_2 and the USWG data at the beach toe.

Acoustic Doppler velocimeters (ADVs, Nortek Vectrino Plus with accuracy of 1% FS) were used to measure all three components of the flow velocity at CP_1 (down-looking probe) and CP_2 (side-looking probe) with a sampling frequency of 50 Hz, and sampling volumes positioned at 15 cm and 0.75 cm above the bed, respectively. For data quality and control, we only report data with a signal-to-noise ratio (SNR) greater than 12 and a correlation value (CORR) greater than 70. Finally, at CP_2, a custom pressure transducer (Omega PX409 series with accuracy of 0.08% FS) was installed with the sensor face flush with the beach surface to measure the bed pressure and two overhead cameras (JAI GO-5100-USB, 2464 x 2056 px, 8 bit resolution) fitted with 8 mm lenses (Thor labs) were mounted above the flume to record images over a combined field of view (FOV) of $x = [-70, 10]$ cm at 33.3 Hz. Data collection from all instruments were synchronized with the start of the wave paddle motion.

3.2.2. Wave Conditions

Single and consecutive solitary waves were used in the experiments to generate single swash events and wave-swash interaction events, respectively. The wave paddle trajectory for single solitary waves uses Goring's theory (Goring, 1979), but the paddle trajectory for consecutive solitary

waves was calculated by AwaSys using Boussinesq wavemaker theory backward in time to create the desired free-surface elevation timeseries at a specified location. As an input to this system, we constructed a timeseries of consecutive solitary waves to be realised at CP_1 using the Boussinesq solution for solitary waves (Boussinesq, 1872) with the wave peaks separated by a nominal separation time, T_{sep}. Measurements of the free-surface displacement and flow velocity at CP_1 compared well with the Boussinesq solution, which showed that the wave generation was robust for producing single and consecutive solitary waves. Additionally, we assessed the experimental repeatability by repeating specific cases covering different wave-swash interaction types five times, which showed the data were very repeatable, as has been previously observed in these type of experiments (Pujara et al., 2015b).

The final set of wave conditions covered single solitary waves with wave heights H=[0.1, 0.2, 0.3, 0.4]h and consecutive solitary waves with $H_{1,2}$=[0.1, 0.2, 0.3, 0.4]h and T_{sep}=[0.75, 1.0, 1.25, 1.50, 1.75, 2.0]T_{H_1} where H_1 is the wave height for the first wave, H_2 is the wave height for the second wave, and T_{H_1} is the (effective) wave period of the first wave. There are four cases of single solitary waves and 60 cases of consecutive solitary waves (summarized in Table (3.2) below).

3.3. Vertical acceleration theory

We inferred the (total) vertical accelerations at CP_2 using data of the bed pressure and surface elevation. To do so, we start with the vertical component of the Navier-Stokes equation

$$\frac{Dw}{Dt} = -\frac{1}{\rho}\frac{\partial p}{\partial z} - g + \nu\nabla^2 w, \tag{3.1}$$

where w is the velocity in the z (vertical) direction, g is the gravitational acceleration, ρ is the fluid density, and ν is the kinematic viscosity. The viscous term ($\nu\nabla^2 w$) was neglected under the assumptions that its influence is small over the bulk of the water column except in thin boundary layers adjacent to the bed and the free surface. Next, assuming that the pressure varied linearly with depth in the shallow swash flow at CP_2, the vertical pressure gradient was approximated in

terms of the difference between the surface pressure and bed pressure. Together, these assumptions reduce Eq. 3.1 to

$$\frac{Dw}{Dt} \approx -\frac{1}{\rho}\frac{(p_{surface} - p_{\text{bed}})}{(\zeta + h_{\text{CP}_2})} - g = \frac{p_{\text{bed}}}{\rho(\zeta + h_{\text{CP}_2})} - g, \tag{3.2}$$

where $p_{surface} = 0$ in gauge pressure, p_{bed} is the bed pressure, and $(\zeta + h_{\text{CP}_2})$ is the total local water depth at CP_2. Thus, we can infer the total vertical accelerations from simultaneous measurements of the total water depth and the bed pressure. Note, only non-hydrostatic pressure distributions lead to vertical accelerations since the vertical acceleration vanishes ($Dw/Dt = 0$) if the pressure distribution is hydrostatic ($p_{\text{bed}} = \rho g(\zeta + h_{\text{CP}_2})$).

3.4. Generation of solitary waves in the wave flume

The piston-type wavemaker in the flume is controlled by Awasys® software, which follows Goring's theory (Goring, 1979) for the solitary wave generation in the wave flume. Due to its in-built functions, the software is limited to generating single solitary waves only. According to this feature, we input an arbitrary time series of surface elevations generated following the Boussinesq wave theory, which the software converts to wave paddle trajectories for the consecutive solitary wave generation. Figures (3.2a and 3.2b) depicts the performance of the wavemaker for the generation of single and double solitary waves, respectively. The time series shows that the wave paddle trajectory for a single wave event (from the in-built software function) matches the one associated with the first wave of a successive wave generation. Then, the wavemaker trajectory for a successive solitary wave case can be seen as a signal composed of two single waves separated by a specific period. According to this, it is possible to infer that the development of two consecutive waves is achieved and appropriate.

3.4.0.1 Validation against Boussinesq and Grimshaw theory

To assess and validate the waves generated in the wave flume, we compare single solitary waves against the Boussinesq and Grimshaw theoretical solutions for small amplitude solitary waves

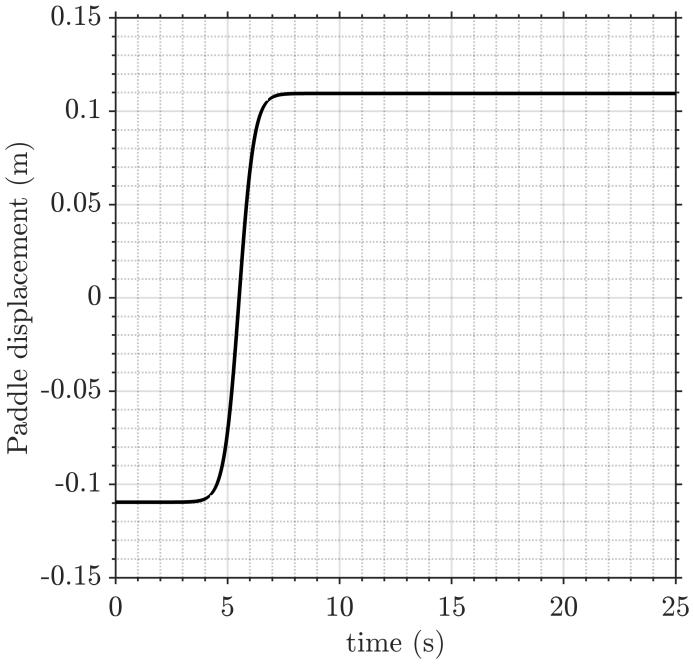

(a)

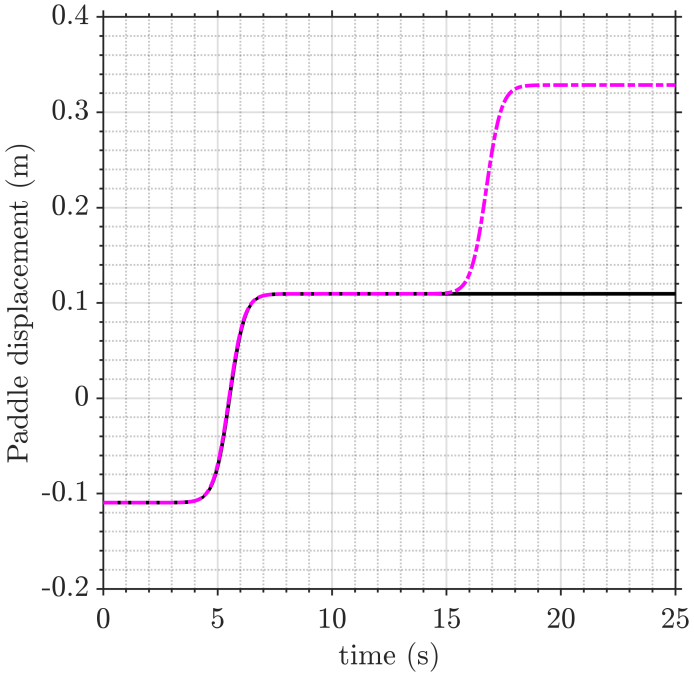

(b)

Figure 3.2: Wave paddle trajectories for solitary waves. (a) Single solitary wave. (b) Double solitary wave compared to a single solitary wave.

(Boussinesq, 1872; Grimshaw, 1970). Figure (3.3) displays the agreement between the measured surface elevations and horizontal velocities from experimental conditions at CP_1, compared to the theoretical solution of these quantities. These direct comparisons show that the generation is appropriate for reproducing single-wave events with high accuracy.

3.4.1. Single Solitary Wave

We run single wave events to understand the variability and difference of wave periods at different measuring locations along the wave flume, which are listed in Table (3.1). As our analysis and estimations focus on the swash zone, we consider using the period measured in the swash (T_{swash}) as the time scale for the separation time between consecutive wave events. To estimate T_{swash}, images were collected at a rate of 33.3Hz for the entire propagation of single wave events along the wave flume. Figures (3.4, 3.5, 3.6, and 3.7) show the field of view of the camera for the specific times where these two moments occur for the wave cases analyzed. We consider these estimated times to be representative of a complete swash cycle.

Table 3.1: Single solitary wave periods estimated at different locations along the wave flume.

Location/Wave	$H = 0.1$h	$H = 0.2$h	$H = 0.3$h	$H = 0.4$h
CD	2.26 s	1.90 s	1.70 s	1.54 s
Toe	2.60 s	2.18 s	2.02 s	1.84 s
CP_2	4.12 s	3.40 s	3.14 s	2.92 s
Swash	4.20 s	4.47 s	4.77 s	5.13 s

We use the results of single solitary wave experiments to extract information of single swash events that can be used as a baseline to understand the wave-swash events driven by consecutive solitary waves. Figure (3.8) shows data of the wave period measured at different cross-shore locations for single solitary wave experiments. At CP_1, beach toe, and CP_2, the wave period is estimated as the time over which the free-surface displacement timeseries is above a small threshold (2.5 mm for $H/h = [0.1, 0.2, 0.3]$ and 4 mm for $H/h = 0.4$). In the constant depth region, beach

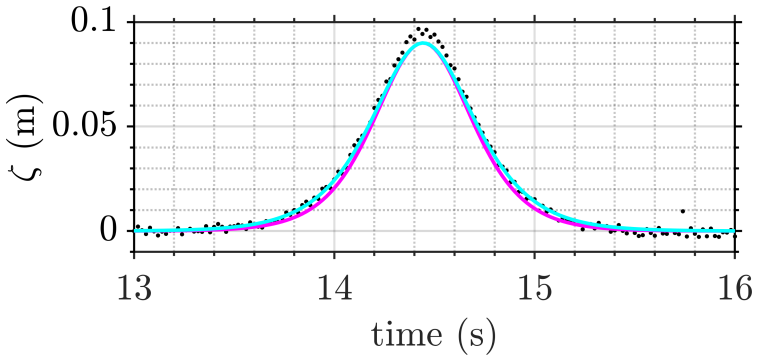

(a)

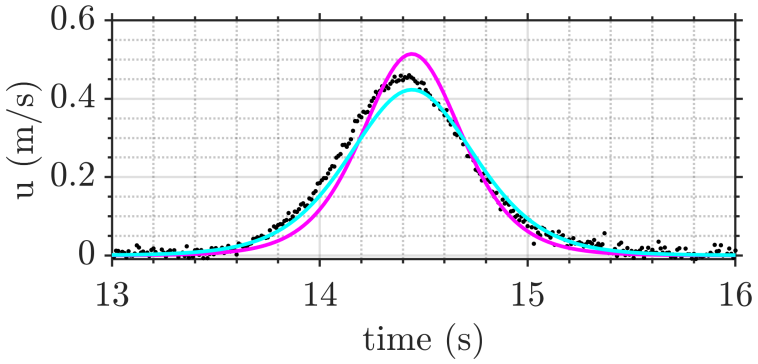

(b)

Figure 3.3: Solitary waves comparisons. Experimental measurements (black dots), Boussinesq theory (magenta solid line) and Grimshaw theory (cyan solid line). Surface elevations (left) and horizontal velocities (right).

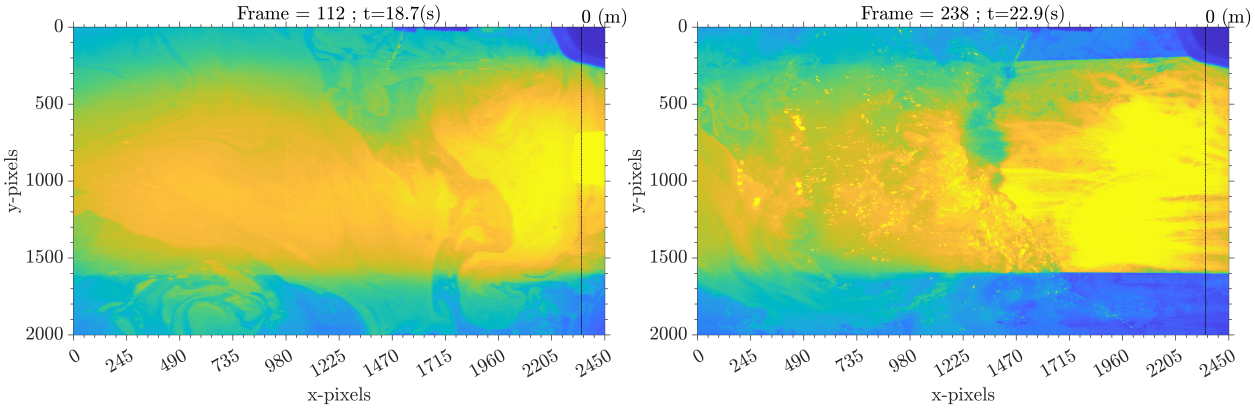

(a) (b)

Figure 3.4: Single wave event $H = 0.1h$. (a) Time at the first shoreward movement of the still water line (18.7 s). (b) Time at the beginning of the hydraulic jump in the swash (22.9 s). Estimated $T_{\text{swash}} = 4.20$ (s).

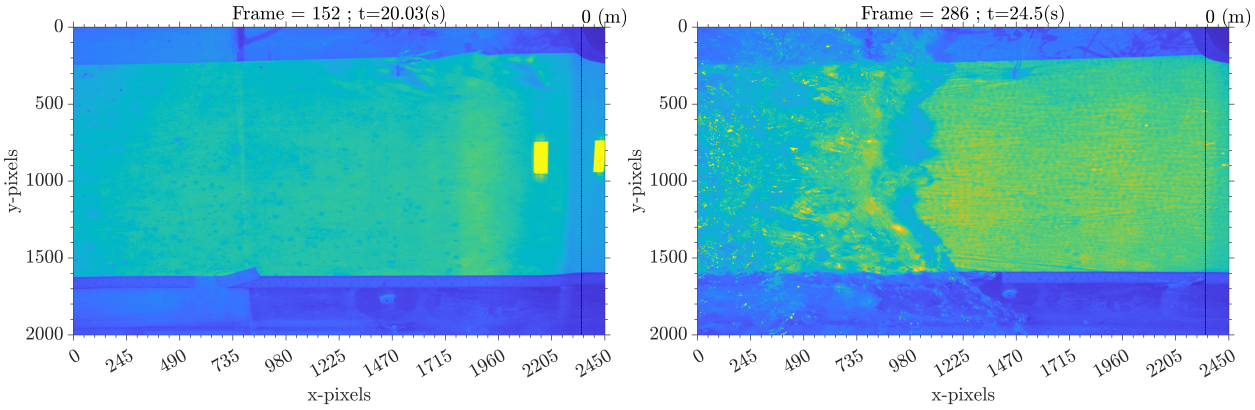

(a) (b)

Figure 3.5: Single wave event $H = 0.2h$. (a) Time at the first shoreward movement of the still water line (20.03 s). (b) Time at the beginning of the hydraulic jump in the swash (24.5 s). Estimated $T_{\text{swash}} = 4.47$ (s).

toe, and at CP_2, the period decreases with increasing wave height. This decrease can be understood in terms of the mechanics of solitary waves, where the wave height and the wavelength are linked. In particular, it is well known that solitary waves become narrower as the wave height increases (Madsen et al., 2008).

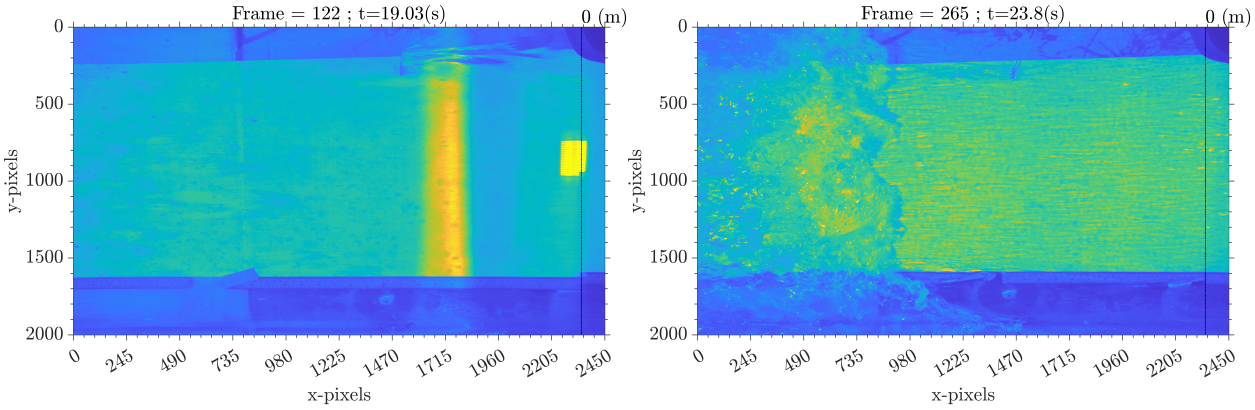

(a) (b)

Figure 3.6: Single wave event $H = 0.3h$. (a) Time at the first shoreward movement of the still water line (19.03 s). (b) Time at the beginning of the hydraulic jump in the swash (23.8 s). Estimated $T_{\text{swash}} = 4.77$ (s).

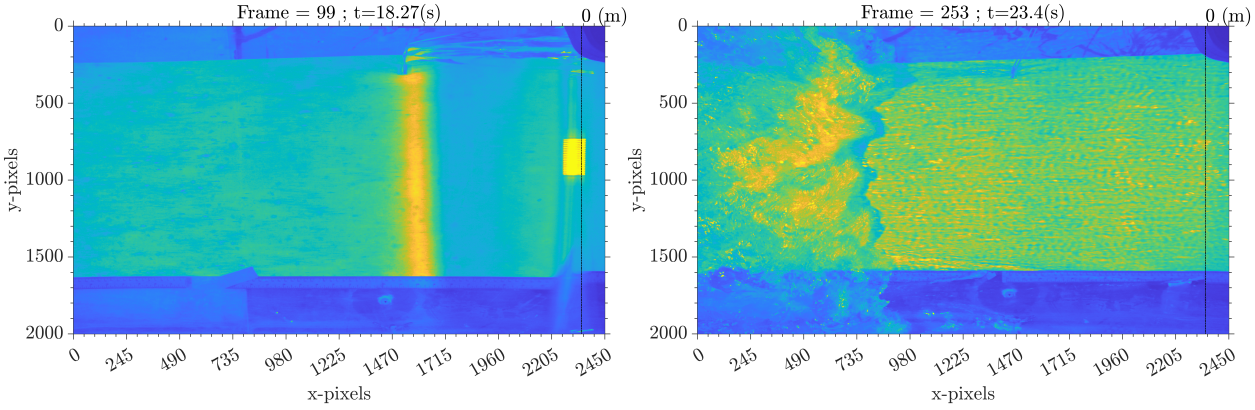

(a) (b)

Figure 3.7: Single wave event $H = 0.4h$. (a) Time at the first shoreward movement of the still water line (18.27 s). (b) Time at the beginning of the hydraulic jump in the swash (23.4 s). Estimated $T_{\text{swash}} = 5.13$ (s).

These results of decreasing wave period with increasing wave height are counter intuitive for the swash event. It is expected, and observed, that waves of larger wave height generated larger swash events that reached a higher run-up and took longer to complete the uprush-backwash swash

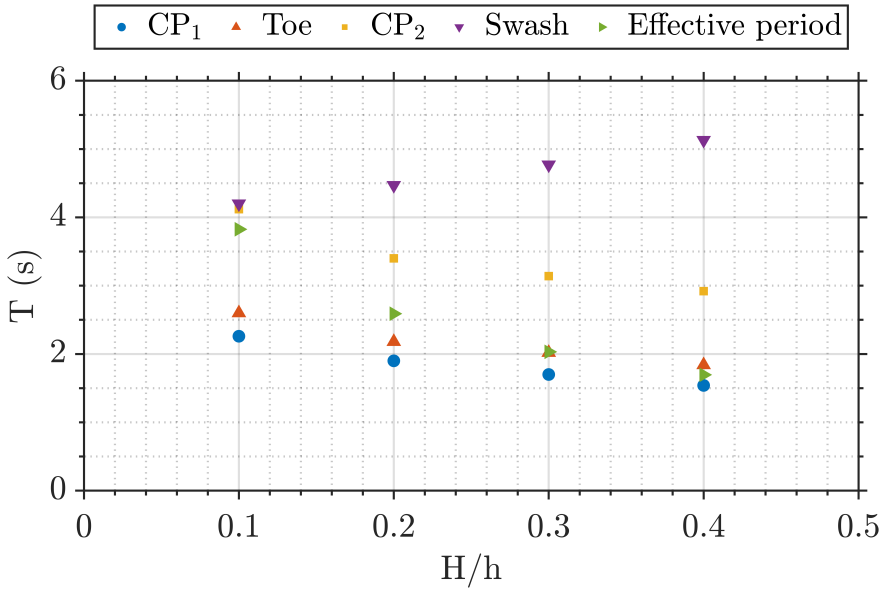

Figure 3.8: Wave periods measured at different locations along the flume. See main text for explanation of how the period at each location was found.

cycle. Thus, it is clear that the wave periods measured offshore of the SWL do not provide a good measure of the period of the swash event. To estimate the true swash period, we used the camera images to find the time between when the shoreline at the still water line first begins to move during the uprush to when a hydraulic jump begins to form during the downrush. This swash period, shown in Figure (3.8), supports basic intuition and observations: the swash period increases with incident wave height. This result also underscores the importance of measuring the swash period directly. In the analysis of wave-swash interactions presented below, we emphasise the importance of this swash period, T_{swash}. In particular, the quantity $T_{\text{sep}}/T_{\text{swash}}$ is the dynamically important dimensionless separation time between consecutive swash events.

Figure (3.9) shows the upward-directed peak vertical accelerations measured at CP_2 (as described in Section (3.3) for single solitary wave experiments as a function of wave height. These peak vertical accelerations occur before the wave crest during the passage of the wave front. As the wave height increases, we observe larger vertical accelerations with values close to gravity for the largest wave tested. The Boussinesq theory of solitary waves (Boussinesq, 1872) allows to predict how the maximum vertical acceleration varies with the wave height in the constant depth region.

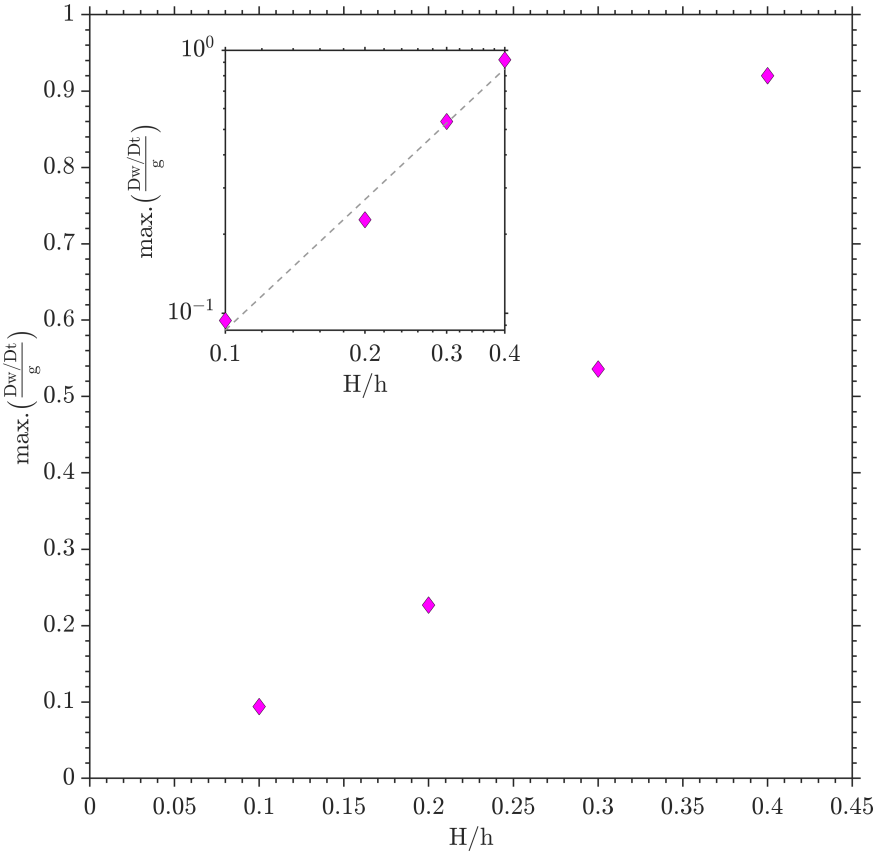

Figure 3.9: Peak upward-directed vertical accelerations at CP_2 as a function of incident solitary wave height. Inset shows the same data with a power-law fit where the best-fit power law exponent is found to be 1.65.

The total vertical acceleration in a constant depth is calculated using the velocities given in Eqs. (1.12 and 1.13). Thus, the total vertical vertical acceleration given by

$$\frac{Dw}{Dt}(x,z,t) = \frac{\partial w}{\partial t} + u\frac{\partial w}{\partial x} + w\frac{\partial w}{\partial z} \tag{3.3}$$

is rewriten in terms of the corresponding velocities and derivatives of the vertical velocity components resulting in the following expression

$$\begin{aligned}\frac{Dw}{Dt}(x,z,t) = Ukc\sqrt{3\epsilon}\left(\frac{z+h}{h}\right)\Big[2\text{sech}^2[k(x-ct)]\tanh^4[k(x-ct)] - \text{sech}^4[k(x-ct)]\Big] - \\ U^2k\sqrt{3\epsilon}\Big[2\text{sech}^4[k(x-ct)]\tanh^2[k(x-ct)] - \text{sech}^6[k(x-ct)]\Big] + \\ U^2(3\epsilon)\left(\frac{z+h}{h^2}\right)\Big[\text{sech}^4[k(x-ct)]\tanh^2[k(x-ct)]\Big],\end{aligned} \tag{3.4}$$

where $U = \epsilon\sqrt{gh}$ is the maximum fluid velocity occurring under the wave crest, with ϵ, k, c, and g defined in Section (1.4.2).

It is easily shown that the peak vertical acceleration follows $Dw/Dt \sim (H/h)^{3/2}$ to leading order and that this scaling comes from the local time derivative ($\partial w/\partial t$) which dominates over the advective acceleration ($u \cdot \nabla w$). The inset in Figure (3.9) shows that the peak vertical acceleration at CP_2 follows a power law with a power-law exponent that is empirically found to be 1.65. The similarity of this value with the predicted value of 1.5 using solitary wave theory in constant depth suggests the peak vertical accelerations for wave crests during their climb of a sloping beach can be understood in terms of incident wave properties, even up to very shallow water depths where the wave shape has evolved significantly during shoaling. It also suggests that shoaling of a wave crest in otherwise quiescent water is insufficient to generate vertical accelerations that exceed the acceleration of gravity.

3.4.2. Consecutive Solitary Waves

3.4.2.1 Validation against Boussinesq theory

To validate the generation of the consecutive solitary waves, we compare the surface elevations and fluid velocity measurements at CP_1 with the Boussinesq theoretical solution for small amplitude solitary waves (Boussinesq, 1872). This comparison is to verify the accuracy of the wave generation, as the surface elevations given to the wavemaker are generated based on Boussinesq theory. Figure (3.10) shows the match between the measurements and the theoretical quantities. The comparison indicates that the wave generation is robust for reproducing the successive solitary waves. In this analysis, we do not include the data from Grimshaw's theory for two main reasons. Firstly, wave generation considers Boussinesq theory, and second, there is an observed discrepancy in the arrival of the second wave to CP_1. This latter is associated with the higher-order terms considered in Grimshaw's theory, which presents peak wave periods and wavelengths slightly different in magnitudes from Boussinesq's theory, making the generation time of the second wave different.

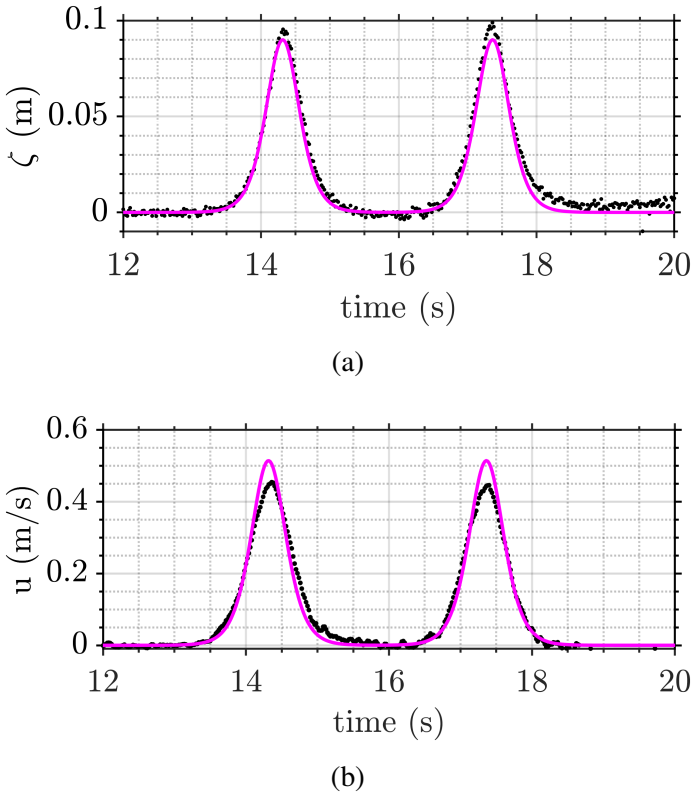

Figure 3.10: Solitary waves comparisons. Experimental measurements (black dots) and Boussinesq theory (magenta solid line). Surface elevations (left) and horizontal velocities (right).

3.4.2.2 Wave-swash Interaction Types and Interaction Zones

Table 3.2: Experimental cases, wave parameters, characteristic ratios at different locations, and type of interaction observed. The interaction types, as described by Hughes and Moseley (2007), include wave-uprush interaction (WUI), weak wave-backwash interaction (WWBI), and strong wave-backwash interaction (SWBI)

Cases	$(H_2/H_1)_{toe}$	$(T_{\text{sep}}/T_{\text{swash}})_{toe}$	$(H_2/H_1)_{CP_2}$	$(T_{\text{sep}}/T_{\text{swash}})_{CP_2}$	Type
$H_1 = 0.1h; H_2 = 0.4h; T_{\text{sep}} = 0.75T_{H_1}$	3.2	0.4	3.2	0.3	WUI
$H_1 = 0.2h; H_2 = 0.3h; T_{\text{sep}} = 0.75T_{H_1}$	1.4	0.3	3.3	0.5	WUI
$H_1 = 0.2h; H_2 = 0.4h; T_{\text{sep}} = 0.75T_{H_1}$	1.7	0.3	3.4	0.8	WUI
$H_1 = 0.2h; H_2 = 0.4h; T_{\text{sep}} = 1.00T_{H_1}$	1.8	0.4	1.8	1.0	WUI
$H_1 = 0.3h; H_2 = 0.3h; T_{\text{sep}} = 0.75T_{H_1}$	1.0	0.3	1.8	1.2	WUI
$H_1 = 0.3h; H_2 = 0.4h; T_{\text{sep}} = 0.75T_{H_1}$	1.2	0.3	2.3	1.4	WUI
$H_1 = 0.3h; H_2 = 0.4h; T_{\text{sep}} = 1.00T_{H_1}$	1.3	0.4	1.5	0.4	WUI
$H_1 = 0.4h; H_2 = 0.3h; T_{\text{sep}} = 0.75T_{H_1}$	0.8	0.3	1.6	0.6	WUI
$H_1 = 0.4h; H_2 = 0.4h; T_{\text{sep}} = 0.75T_{H_1}$	1.0	0.3	1.5	0.7	WUI
$H_1 = 0.4h; H_2 = 0.4h; T_{\text{sep}} = 1.00T_{H_1}$	1.1	0.3	1.5	0.9	WUI
$H_1 = 0.1h; H_2 = 0.4h; T_{\text{sep}} = 1.00T_{H_1}$	3.3	0.6	0.7	1.1	WWBI
$H_1 = 0.1h; H_2 = 0.4h; T_{\text{sep}} = 1.25T_{H_1}$	3.4	0.9	0.6	1.2	WWBI
$H_1 = 0.2h; H_2 = 0.2h; T_{\text{sep}} = 0.75T_{H_1}$	1.1	0.4	1.7	0.3	WWBI
$H_1 = 0.2h; H_2 = 0.2h; T_{\text{sep}} = 1.00T_{H_1}$	1.1	0.6	1.9	0.5	WWBI
$H_1 = 0.2h; H_2 = 0.2h; T_{\text{sep}} = 1.25T_{H_1}$	1.1	0.7	1.9	0.6	WWBI
$H_1 = 0.2h; H_2 = 0.3h; T_{\text{sep}} = 1.00T_{H_1}$	1.5	0.5	1.8	0.8	WWBI
$H_1 = 0.2h; H_2 = 0.3h; T_{\text{sep}} = 1.25T_{H_1}$	1.5	0.6	1.7	0.9	WWBI
$H_1 = 0.2h; H_2 = 0.3h; T_{\text{sep}} = 1.50T_{H_1}$	1.5	0.8	0.7	1.1	WWBI
$H_1 = 0.2h; H_2 = 0.4h; T_{\text{sep}} = 1.25T_{H_1}$	2.2	0.5	1.9	0.3	WWBI
$H_1 = 0.2h; H_2 = 0.4h; T_{\text{sep}} = 1.50T_{H_1}$	1.8	0.7	2.1	0.4	WWBI
$H_1 = 0.2h; H_2 = 0.4h; T_{\text{sep}} = 1.75T_{H_1}$	2.1	0.8	2.1	0.5	WWBI
$H_1 = 0.3h; H_2 = 0.2h; T_{\text{sep}} = 0.75T_{H_1}$	0.8	0.4	2.1	0.7	WWBI
$H_1 = 0.3h; H_2 = 0.2h; T_{\text{sep}} = 1.00T_{H_1}$	0.8	0.5	1.9	0.8	WWBI
$H_1 = 0.3h; H_2 = 0.2h; T_{\text{sep}} = 1.25T_{H_1}$	0.8	0.6	1.3	1.0	WWBI

Continued on next page

Table 3.2 – continued from previous page

Cases	$(H_2/H_1)_{toe}$	$(T_{\text{sep}}/T_{\text{swash}})_{toe}$	$(H_2/H_1)_{CP_2}$	$(T_{\text{sep}}/T_{\text{swash}})_{CP_2}$	Type
$H_1 = 0.3h; H_2 = 0.3h; T_{\text{sep}} = 1.00T_{H_1}$	1.1	0.4	1.2	0.4	WWBI
$H_1 = 0.3h; H_2 = 0.3h; T_{\text{sep}} = 1.25T_{H_1}$	1.1	0.5	1.2	0.5	WWBI
$H_1 = 0.3h; H_2 = 0.3h; T_{\text{sep}} = 1.50T_{H_1}$	1.1	0.6	1.3	0.7	WWBI
$H_1 = 0.3h; H_2 = 0.4h; T_{\text{sep}} = 1.25T_{H_1}$	1.4	0.5	1.0	0.8	WWBI
$H_1 = 0.3h; H_2 = 0.4h; T_{\text{sep}} = 1.50T_{H_1}$	1.3	0.6	0.9	0.9	WWBI
$H_1 = 0.3h; H_2 = 0.4h; T_{\text{sep}} = 1.75T_{H_1}$	1.3	0.7	0.6	1.0	WWBI
$H_1 = 0.3h; H_2 = 0.4h; T_{\text{sep}} = 2.00T_{H_1}$	1.3	0.8	1.4	0.3	WWBI
$H_1 = 0.4h; H_2 = 0.2h; T_{\text{sep}} = 0.75T_{H_1}$	0.6	0.4	1.4	0.4	WWBI
$H_1 = 0.4h; H_2 = 0.2h; T_{\text{sep}} = 1.00T_{H_1}$	0.6	0.5	1.5	0.5	WWBI
$H_1 = 0.4h; H_2 = 0.2h; T_{\text{sep}} = 1.25T_{H_1}$	1.0	0.6	1.5	0.7	WWBI
$H_1 = 0.4h; H_2 = 0.3h; T_{\text{sep}} = 1.00T_{H_1}$	0.9	0.4	1.3	0.8	WWBI
$H_1 = 0.4h; H_2 = 0.3h; T_{\text{sep}} = 1.25T_{H_1}$	0.9	0.5	1.4	0.9	WWBI
$H_1 = 0.4h; H_2 = 0.3h; T_{\text{sep}} = 1.50T_{H_1}$	0.9	0.6	1.4	0.3	WWBI
$H_1 = 0.4h; H_2 = 0.3h; T_{\text{sep}} = 1.75T_{H_1}$	0.9	0.6	1.6	0.4	WWBI
$H_1 = 0.4h; H_2 = 0.4h; T_{\text{sep}} = 1.25T_{H_1}$	1.1	0.4	1.6	0.5	WWBI
$H_1 = 0.4h; H_2 = 0.4h; T_{\text{sep}} = 1.50T_{H_1}$	1.1	0.5	1.7	0.6	WWBI
$H_1 = 0.4h; H_2 = 0.4h; T_{\text{sep}} = 1.75T_{H_1}$	1.1	0.6	1.5	0.7	WWBI
$H_1 = 0.4h; H_2 = 0.4h; T_{\text{sep}} = 2.00T_{H_1}$	1.1	0.7	1.4	0.8	WWBI
$H_1 = 0.1h; H_2 = 0.4h; T_{\text{sep}} = 1.50T_{H_1}$	3.4	1.1	1.0	0.4	SWBI
$H_1 = 0.2h; H_2 = 0.2h; T_{\text{sep}} = 1.50T_{H_1}$	1.1	0.9	1.1	0.5	SWBI
$H_1 = 0.2h; H_2 = 0.2h; T_{\text{sep}} = 1.75T_{H_1}$	1.1	1.0	1.0	0.6	SWBI
$H_1 = 0.2h; H_2 = 0.2h; T_{\text{sep}} = 2.00T_{H_1}$	1.2	1.2	0.8	0.7	SWBI
$H_1 = 0.2h; H_2 = 0.3h; T_{\text{sep}} = 1.75T_{H_1}$	1.5	0.9	0.9	0.8	SWBI
$H_1 = 0.2h; H_2 = 0.3h; T_{\text{sep}} = 2.00T_{H_1}$	1.6	1.1	0.9	0.9	SWBI
$H_1 = 0.2h; H_2 = 0.4h; T_{\text{sep}} = 2.00T_{H_1}$	1.9	1.0	1.2	0.3	SWBI
$H_1 = 0.3h; H_2 = 0.2h; T_{\text{sep}} = 1.50T_{H_1}$	0.8	0.7	1.2	0.4	SWBI
$H_1 = 0.3h; H_2 = 0.2h; T_{\text{sep}} = 1.75T_{H_1}$	0.8	0.8	1.2	0.5	SWBI
$H_1 = 0.3h; H_2 = 0.2h; T_{\text{sep}} = 2.00T_{H_1}$	0.8	0.9	1.3	0.6	SWBI
$H_1 = 0.3h; H_2 = 0.3h; T_{\text{sep}} = 1.75T_{H_1}$	1.1	0.7	1.1	0.7	SWBI
$H_1 = 0.3h; H_2 = 0.3h; T_{\text{sep}} = 2.00T_{H_1}$	1.1	0.9	0.9	0.8	SWBI

Continued on next page

Table 3.2 – continued from previous page

Cases	$(H_2/H_1)_{toe}$	$(T_{\text{sep}}/T_{\text{swash}})_{toe}$	$(H_2/H_1)_{\text{CP}_2}$	$(T_{\text{sep}}/T_{\text{swash}})_{\text{CP}_2}$	Type
$H_1 = 0.4h; H_2 = 0.2h; T_{\text{sep}} = 1.50T_{H_1}$	0.7	0.6	1.2	0.3	SWBI
$H_1 = 0.4h; H_2 = 0.2h; T_{\text{sep}} = 1.75T_{H_1}$	1.1	0.8	1.4	0.3	SWBI
$H_1 = 0.4h; H_2 = 0.2h; T_{\text{sep}} = 2.00T_{H_1}$	0.6	0.8	1.3	0.4	SWBI
$H_1 = 0.4h; H_2 = 0.3h; T_{\text{sep}} = 2.00T_{H_1}$	0.9	0.7	1.4	0.5	SWBI
$H_1 = 0.1h; H_2 = 0.4h; T_{\text{sep}} = 1.75T_{H_1}$	3.6	1.3	1.3	0.6	No Interaction
$H_1 = 0.1h; H_2 = 0.4h; T_{\text{sep}} = 2.00T_{H_1}$	3.6	1.5	1.1	0.7	No Interaction

By using consecutive solitary waves controlling the height of each wave and the separation between them, it was possible to produce different wave-swash interactions types as observed, categorized, and described by Hughes and Moseley (2007) and others in the field. These are wave-uprush interaction (WUI), where the second wave crest has delayed breaking and collapse as it propagates further onshore over a layer of uprush flow generated by the swash of the first wave crest; weak wave-backwash interaction (WWBI), where the second wave crest encounters the backwash flow of the swash of the first wave, inducing accelerated breaking and collapse; and strong wave-backwash interaction (SWBI), where a stationary bore is generated by sudden breaking of the second wave crest as it encounters the strong backwash flow of the swash of the first wave.

Table (3.2) presents a complete list of the 60 cases of consecutive solitary wave experiments. For each case, we list the observed wave-swash interaction type, the wave height ratio (H_2/H_1) measured at the beach toe and at CP_2 and the dimensionless separation time ($T_{\text{sep}}/T_{\text{swash}}$) measured at CP_2. The wave height and separation time measurements were made by first using a Gaussian kernel low pass filter (Mordant et al., 2004; Pujara et al., 2021) to the surface elevation measurements to reduce noise and simplify finding the peak of the free-surface displacement signal. Figure (3.11) shows an example of the estimation for these quantities at the toe of the beach and at CP_2. Figure (3.12) shows three interacting cases observed in the field and reproduced experimentally. Pictures show a snapshot of the second incoming wave at the moment of the interaction. Some

characteristic differences exist for each interacting case. In the wave-upwash interaction case, the second incoming wave overturning takes longer to develop as it propagates further onshore over a layer of upwash flow generated by the first wave event. Contrarily, in the weak wave-backwash interaction, the second wave encounters a backwash flow of the first wave, inducing a faster overturning of the second incoming wave. It is observed that in this type of interaction the curl of the second wave is flatter compared to the one caused by the wave-upwash interaction. The strong wave-backwash interaction shows a clear bore generated by a sudden overturning of the second wave and due to a fast instability of the wave curl induced by the strong backwash flow of the first wave event.

From camera recordings, it was possible to map the region of influence for the interactions associated with each experimental case. Figure (3.13) maps out the typical stages of a wave-swash interaction with examples of each interaction type. From the camera images, we observed that wave-swash interactions consistently displayed three stages: First, the approaching wave crest's overturning created a jet which struck the water ahead of it ("jet slamming"). Second, this breaker jet created a splash that altered the shallow flow ahead of the breaker ("splash-induced flow"). Finally, this interaction between the breaker and the swash of the preceding wave showed signs of fluid instabilities that quickly transitioned into highly turbulent flow ("fully 3D turbulent flow"). Some aspects of these observations have also been reported in the inner surf and swash zones of plunging breaker regular waves (Sou and Yeh, 2011; Sumer et al., 2013). However, the location of where the interaction takes place, as well as the spatial extent where these three stages occur, varies for different wave-swash interaction types, which has not been previously reported in laboratory studies. As Figure (3.13) shows, the interaction zone moves offshore for wave-backwash interactions compared with wave-uprush interactions and there is less overlap in the spatial extent of the three stages for strong wave-backwash interactions compared with weak wave-backwash interactions. Using the maps of the regions of influence per interaction can give potential relevant information to sediment transport analysis, as the sediment direction and consequently its deposition to the SWL, is influenced by the type of wave-swash interaction event, as noted by Cáceres and Alsina (2012).

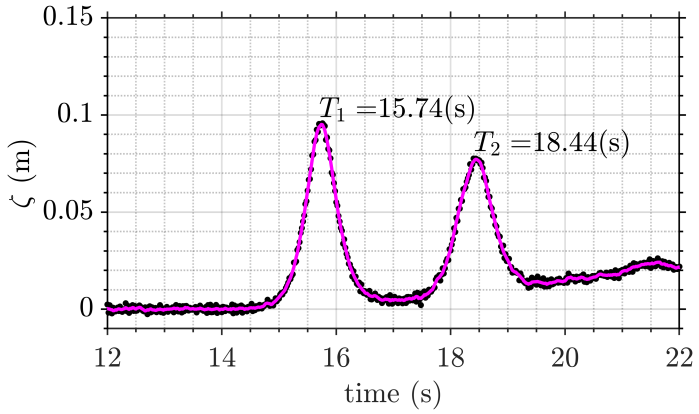

(a)

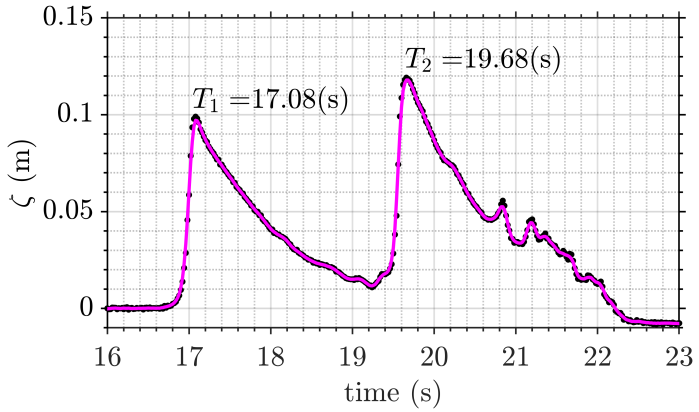

(b)

Figure 3.11: Estimation of T_{sep} from surface elevation measurements. Case: $H_1 = 0.3h$; $H_2 = 0.2h$; $T_{\text{sep}} = 1.0T_{H_1}$. (a) Toe of the beach. (b) Measuring point CP_2. Experimental measurements (black dots) and fitted signal (magenta solid line).

3.5. Hydrodynamics of Wave-swash Interactions

While the qualitative wave-swash interaction types and stages described above are useful for classification purposes, they do not reveal any information of the underlying hydrodynamics. Thus, we now tackle the quantitative analysis of wave-swash interactions. Figures (3.14)-(3.16) show the typical timeseries at CP_2 for wave-upwash, weak wave-backwash, and strong wave-backwash interactions, respectively. Gaps in the data are related to quality control procedures described in

(a)

(b)

(c)

Figure 3.12: Types of wave-swash interactions from laboratory experiments. (a) Wave-upwash interaction. (b) Weak wave-backwash interaction. (c) Strong wave-backwash interaction.

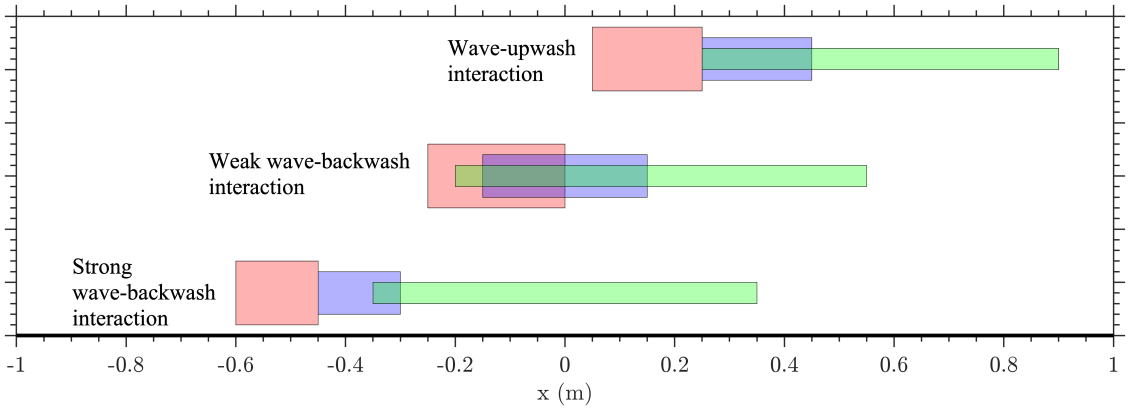

Figure 3.13: Spatial extent of wave-swash interactions and their different stages: jet slamming (red), splash-induced flow (purple), and fully 3D turbulent flow (green). Wave-upwash interaction ($H_1 = 0.2h$; $H_2 = 0.4h$; $T_{\text{sep}} = 1.0T_{H_1}$); weak wave-backwash interaction ($H_1 = 0.3h$; $H_2 = 0.3h$; $T_{\text{sep}} = 1.5T_{H_1}$); and strong wave-backwash interaction ($H_1 = 0.3h$; $H_2 = 0.2h$; $T_{\text{sep}} = 1.5T_{H_1}$).

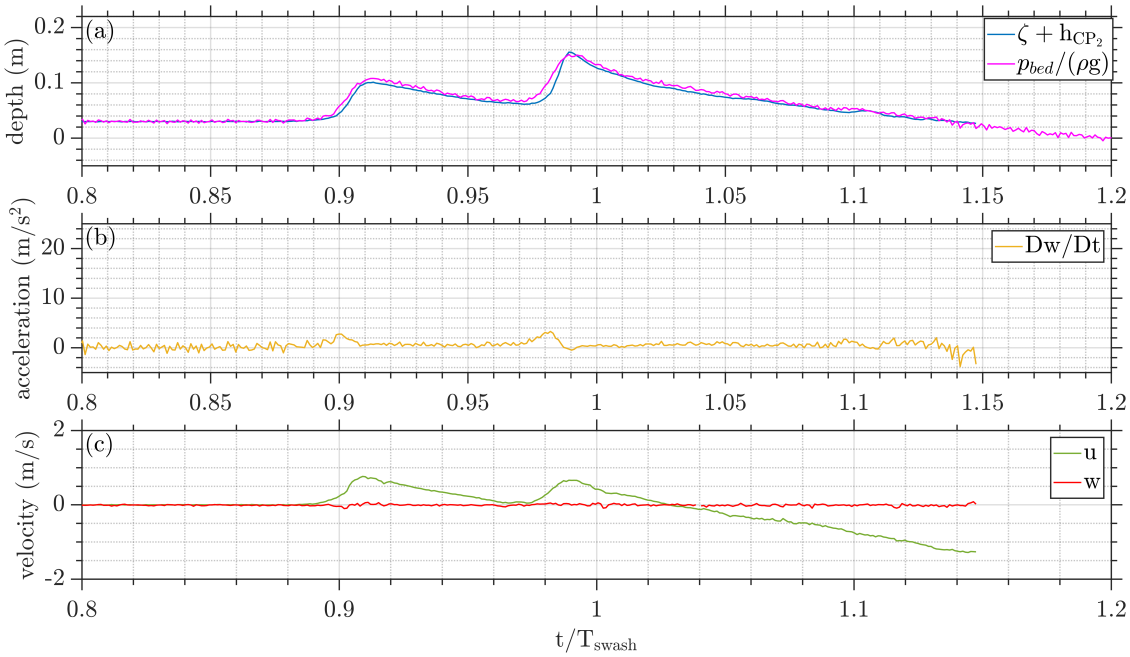

Figure 3.14: Time series of elevations, bottom pressures converted to elevations, and estimated total vertical accelerations. Wave-upwash interactions. Case: $H_1 = 0.2h$; $H_2 = 0.3h$; $T_{\text{sep}} = 0.75T_{H_1}$ ($H_2/H_1 = 1.5$; $T_{\text{sep}} = 0.084T_{\text{swash}}$).

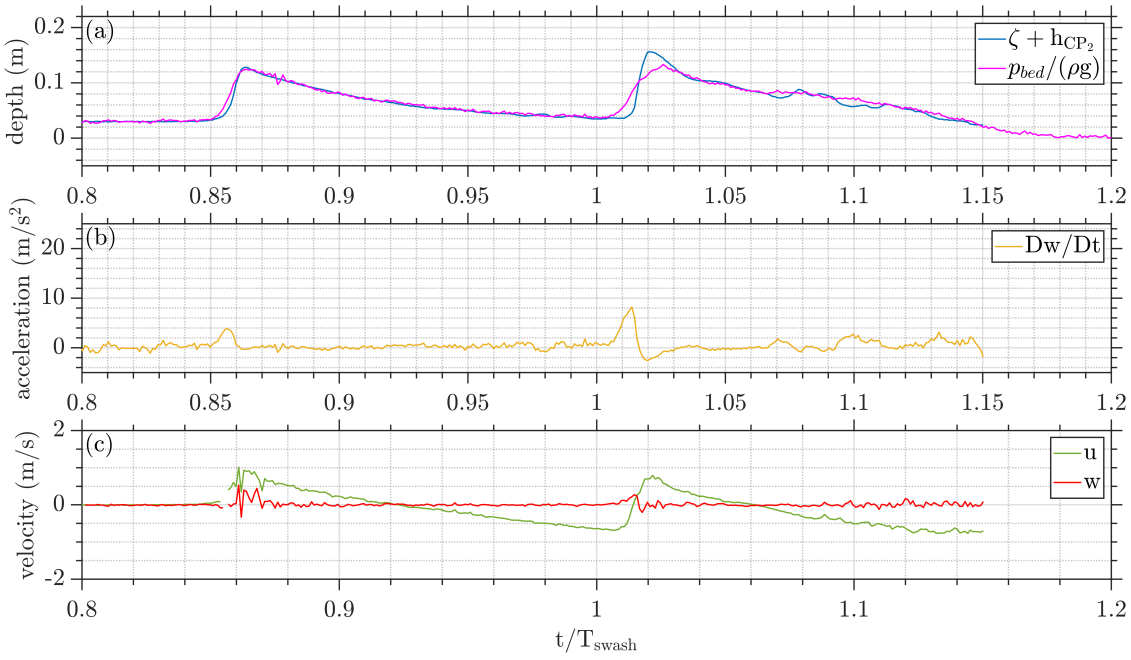

Figure 3.15: Time series of elevations, bottom pressures converted to elevations, and estimated total vertical accelerations. Weak wave-backwash interactions. Case: $H_1 = 0.3h$; $H_2 = 0.2h$; $T_{\text{sep}} = 1.25T_{H_1}$ ($H_2/H_1 = 0.667$; $T_{\text{sep}} = 0.128T_{\text{swash}}$).

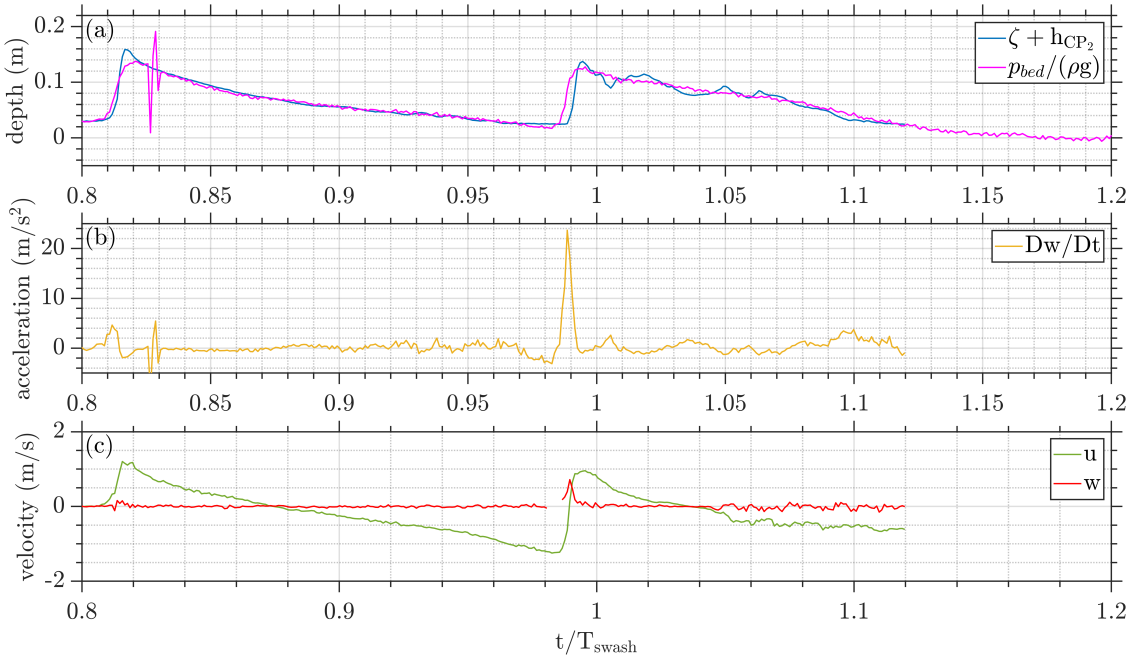

Figure 3.16: Time series of elevations, bottom pressures converted to elevations, and estimated total vertical accelerations. Strong wave-backwash interactions. Case: $H_1 = 0.4h$; $H_2 = 0.2h$; $T_{\text{sep}} = 1.50T_{H_1}$ ($H_2/H_1 = 0.5$; $T_{\text{sep}} = 0.137T_{\text{swash}}$).

Section (3.2.1). In the bed pressure data, there are large fluctuations after the passage of the first wave crest. These are associated with beach vibrations induced by the jet slamming of the first wave and are therefore experimental artifacts.

The top panels in these figures show the total water depth and bed pressure in units of depth together, which when compared with the vertical accelerations in the middle panel, show how the vertical accelerations result from a non-hydrostatic pressure distribution. Focusing on the vertical accelerations, it is evident that the passage of a shoaling wave crest into quiescent water generates accelerations of magnitude up to that of gravity, whereas the wave crest interacting with the swash event of the previous wave results in larger acceleration with values far exceeding gravity. The velocity data in the bottom panel shows that the peak vertical acceleration in the wave-swash interaction is near concurrent with the peak positive horizontal and vertical velocities. Though we do not show it explicitly, the velocity data also show that, in contrast to single solitary wave data, the local time derivative of the vertical velocity ($\partial w/\partial t$) is insufficient to explain the inferred vertical accelerations, suggesting that the advective part of the vertical acceleration ($u \cdot \nabla w$) is important. Finally, we note that the qualitative wave-swash interaction types do not necessarily predict the hydrodynamics, but the advantage of our experimental setup is that the wave height ratio H_2/H_1 and the dimensionless separation time $T_{\text{sep}}/T_{\text{swash}}$ provide a quantitative parameter space in which we can map out the hydrodynamics. We assess the experimental reproduction by repeating specific cases of each wave-swash interaction five times, allowing us to verify the degree of accuracy in the experimental results.

3.5.1. Experimental reproduction

Figures (3.17) to (3.19) show the repeatability for different types of interaction. Plots presents the time series of surface elevations, bottom pressures converted to elevations, and the estimated vertical accelerations. It is possible to observe that the variability between the repetitions is small, indicating the reliability of the experiments and associated results.

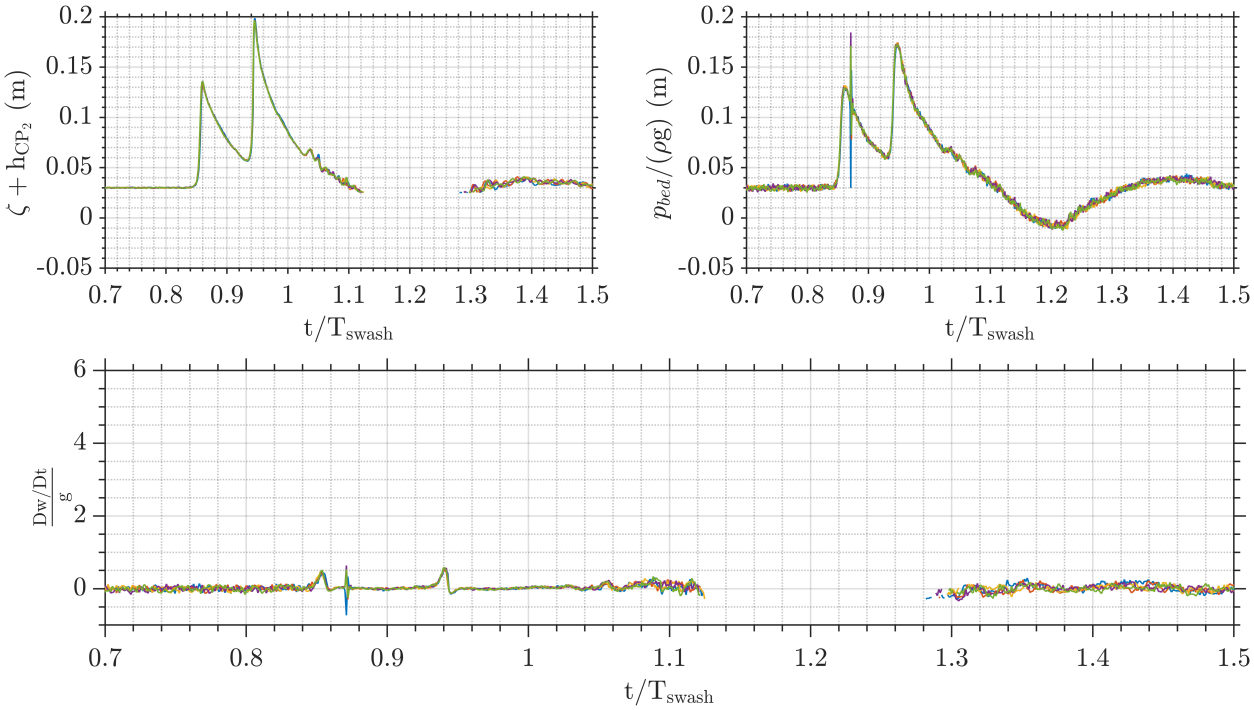

Figure 3.17: Repeatability of wave-upwash interactions. $H_2/H_1 = 1.33$; $T_{sep} = 0.102T_{swash}$.

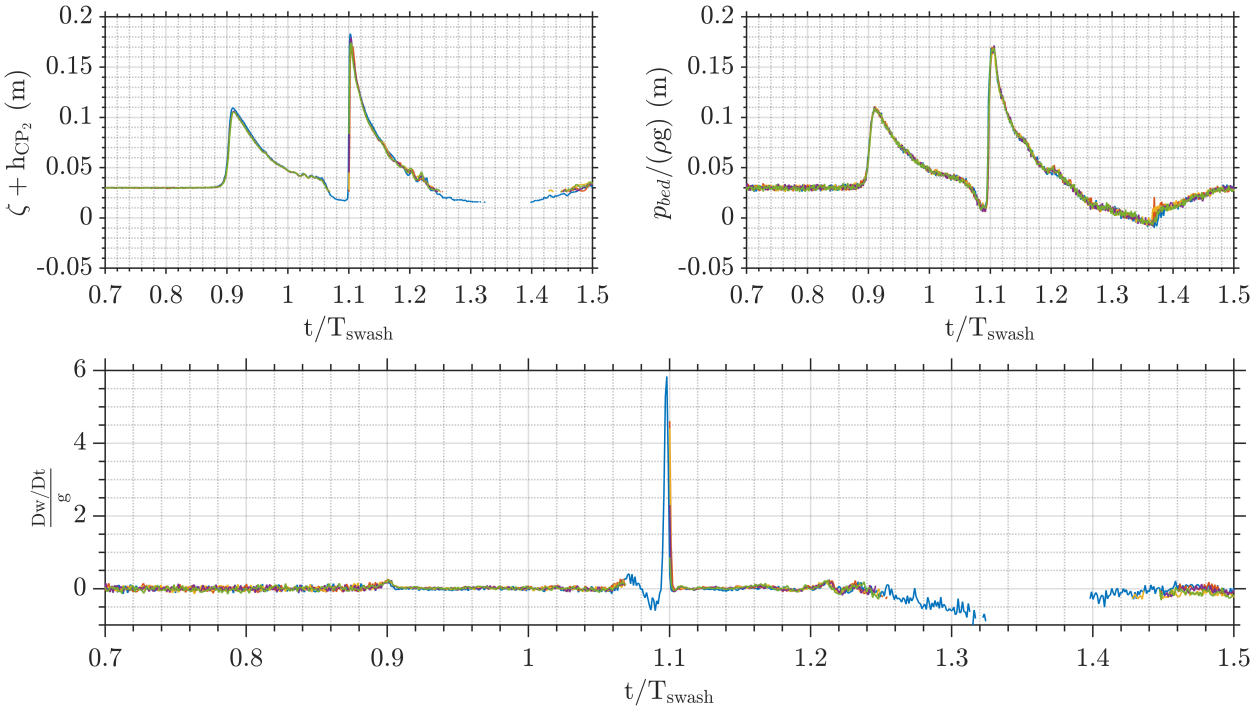

Figure 3.18: Repeatability of weak wave-backwash interactions. $H_2/H_1 = 2.0$; $T_{sep} = 0.1962T_{swash}$.

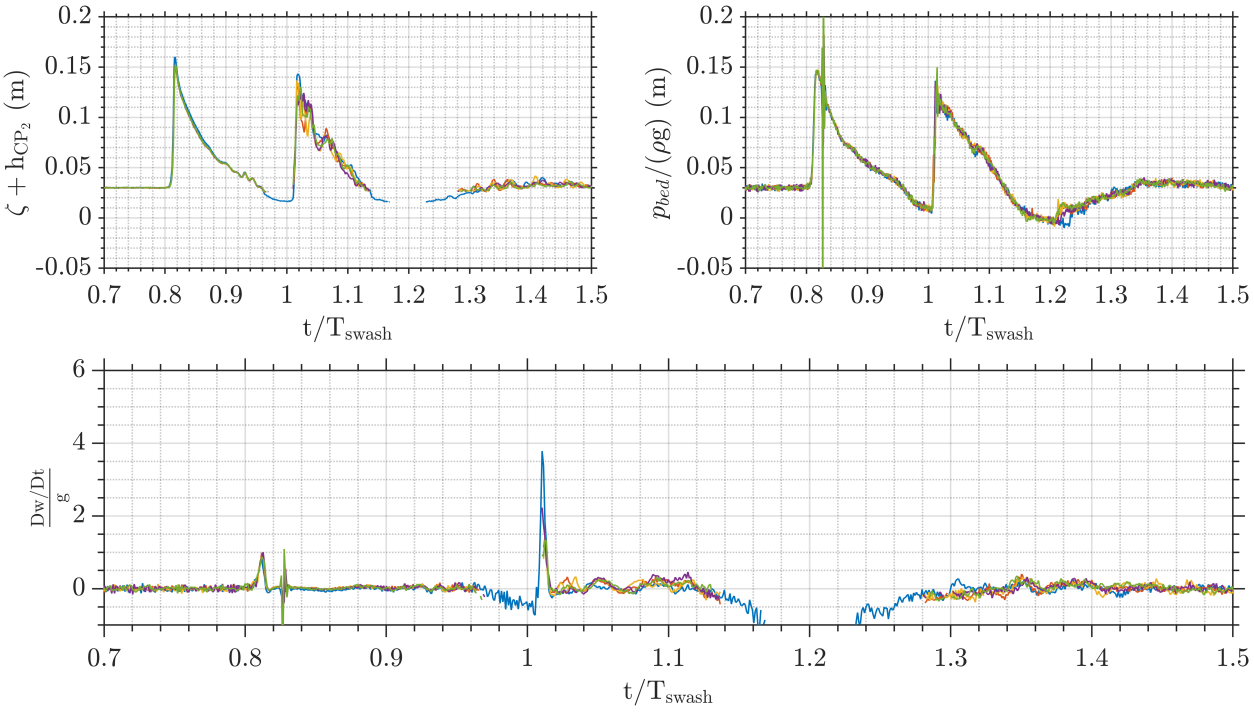

Figure 3.19: Repeatability of strong wave-backwash interactions. $H_2/H_1 = 0.5$; $T_{sep} = 0.160T_{swash}$.

3.5.2. Swash-interactions mapping

Figure (3.20) shows the distribution of the wave-swash interactions as a function of H_2/H_1 and $T_{\text{sep}}/T_{\text{swash}}$ as measured at CP_1 (panel a) and CP_2 (panel b). Observed qualitative interaction types cluster together: Wave-uprush interactions are towards the top (and slightly left), weak wave-backwash interactions are in the middle, and strong wave-backwash interactions are towards the bottom (and slightly towards the right). The differences between the panels, which depend on the location where the wave heights and separation time are measured, are also instructive. Based on the 'far-field' measurements at CP_1, the separation time between consecutive wave crests is apparently more significant for predicting the interaction type than the wave height ratio. In contrast, for values of $H_2/H_1 < 1$, the 'local' measurements at CP_2 show that the type of interaction is almost exclusively strong wave-backwash. Since the main interest lies in understanding the flow and accelerations in the wave-swash interaction zone, the following analyses and figures will focus on measurements from CP_2. However, 'far field' plots at CP_1 are also included to exemplify the variability of the interactions and the associated accelerations and velocities when the characteristic ratios are constructed from measurements collected at this location.

Figure (3.21) presents the main results of this study: the peak upward-directed vertical acceleration magnitude as a function of H_2/H_1 and $T_{\text{sep}}/T_{\text{swash}}$ at CP_2. We observe that while the peak accelerations are larger for wave-backwash interactions (whether weak or strong) compared with wave-uprush interactions, it is not necessarily the case that strong wave-backwash interactions produce larger accelerations than weak wave-backwash interactions. The data show that there is a region of the parameter space, approximately $0.5 < H_2/H_1 < 2$ and $0.6 < T_{\text{sep}}/T_{\text{swash}} < 1.2$, where the peak accelerations are the largest. Physically, this corresponds to situations where the strength of the backwash flows generated by the swash of the first wave collide with an incoming wave front with approximately equal and opposite velocities. The peak vertical acceleration in the interaction is not particularly large if the velocity in either the backwash of the first wave or the wave front of the second wave dominates over the other.

In Figure (3.22), we investigate the time of the peak vertical acceleration, T_{peak}, to understand how it relates to the swash period T_{swash} and the magnitude of the acceleration peak. The timing of

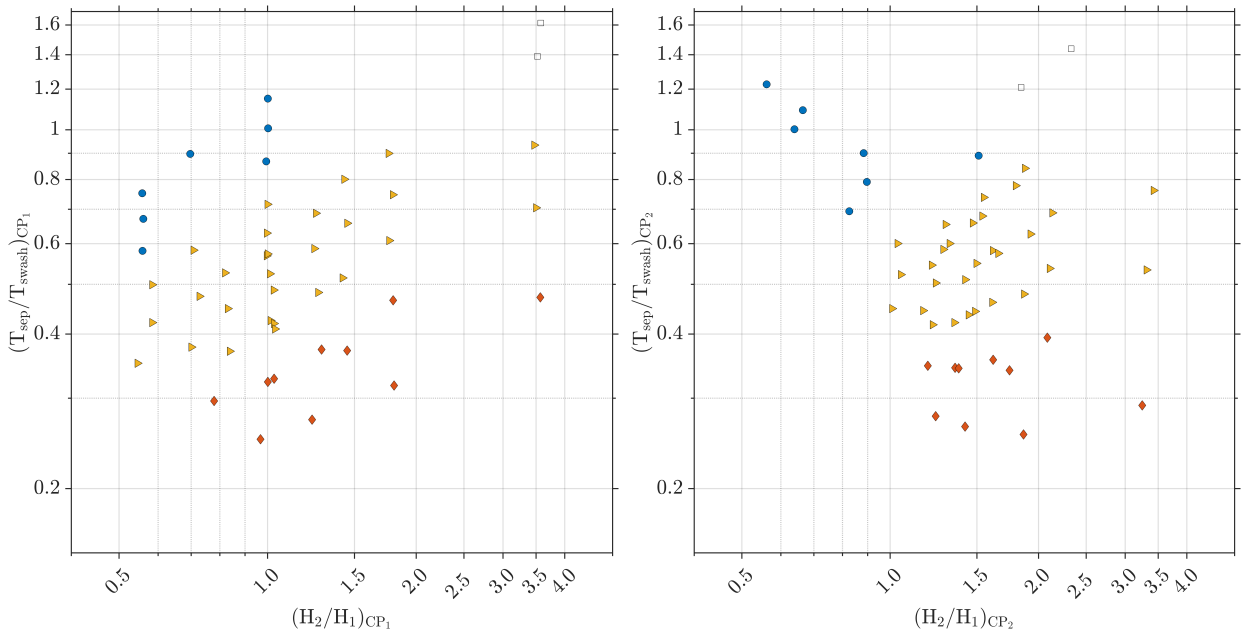

Figure 3.20: Wave-swash interactions mapping according to ratios H_2/H_1 and $T_{\text{sep}}/T_{\text{swash}}$. (a) Measurements at CP_1. (b) Measurements at CP_2. Wave-upwash interaction (diamonds), weak wave-backwash interaction (triangles), strong wave-backwash interaction (circles), no interaction (blank squares).

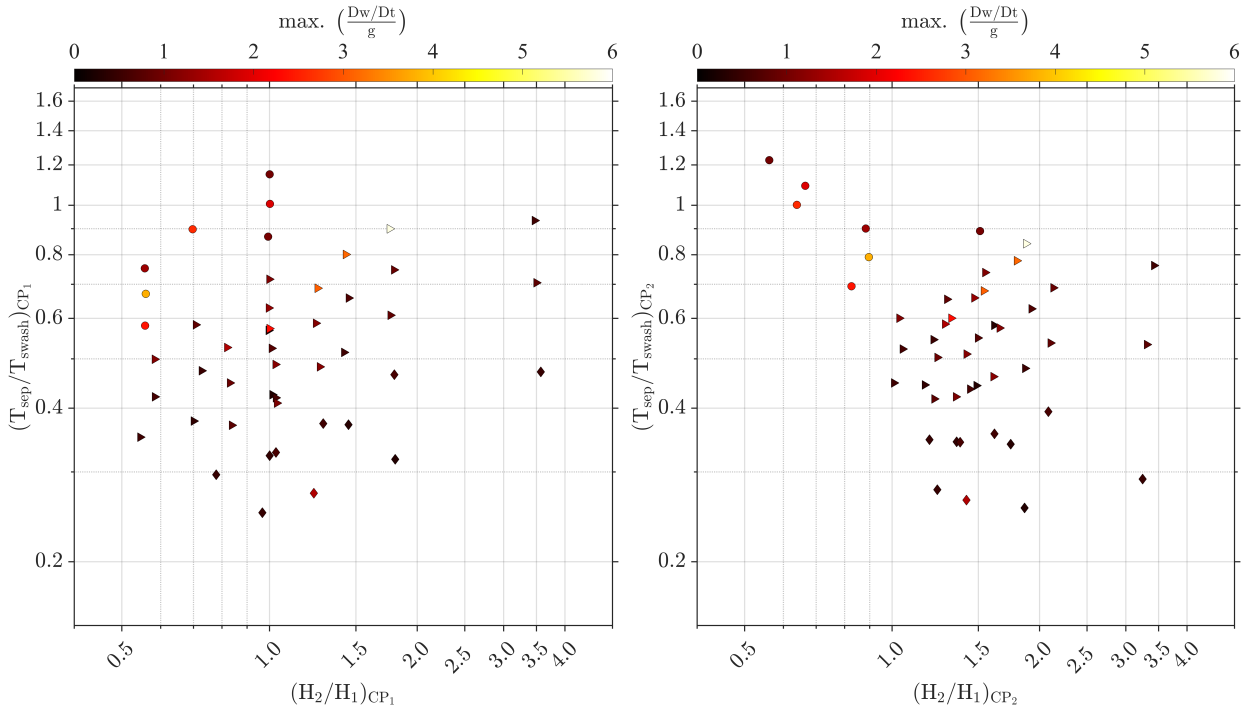

Figure 3.21: Distribution of maximum total vertical accelerations for different wave-swash interactions. (a) Measurements at CP_1. (b) Measurements at CP_2. Wave-upwash interaction (diamonds), weak wave-backwash interaction (triangles), strong wave-backwash interaction (circles).

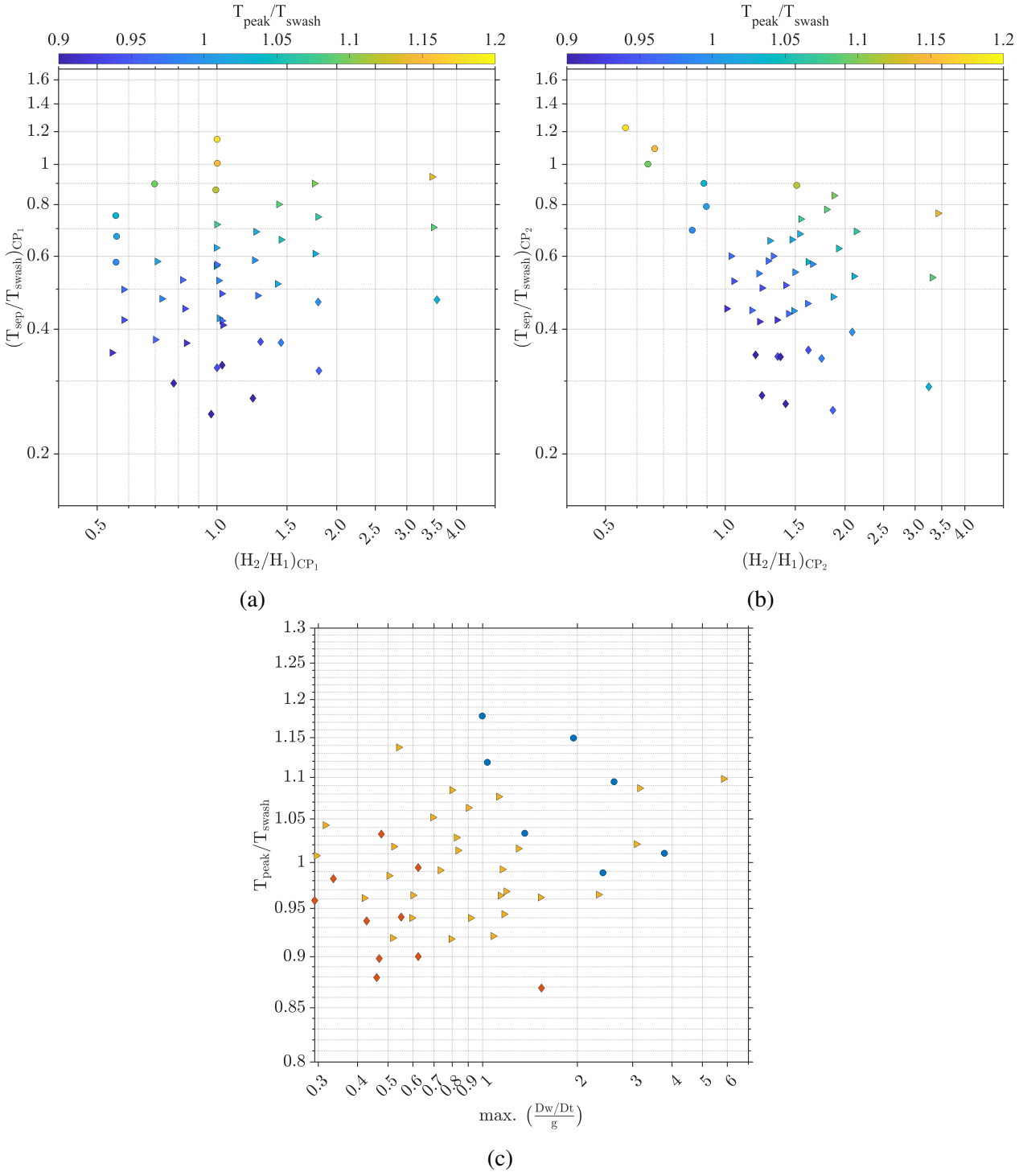

Figure 3.22: Wave-swash interactions mapping Distribution of peak time for different wave interactions. (a) Measurements at CP_1. Measurements at CP_2. (c) Maximum accelerations vs. T_{peak}/T_{swash}. Wave-upwash interaction (diamonds), weak wave-backwash interaction (triangles), strong wave-backwash interaction (circles).

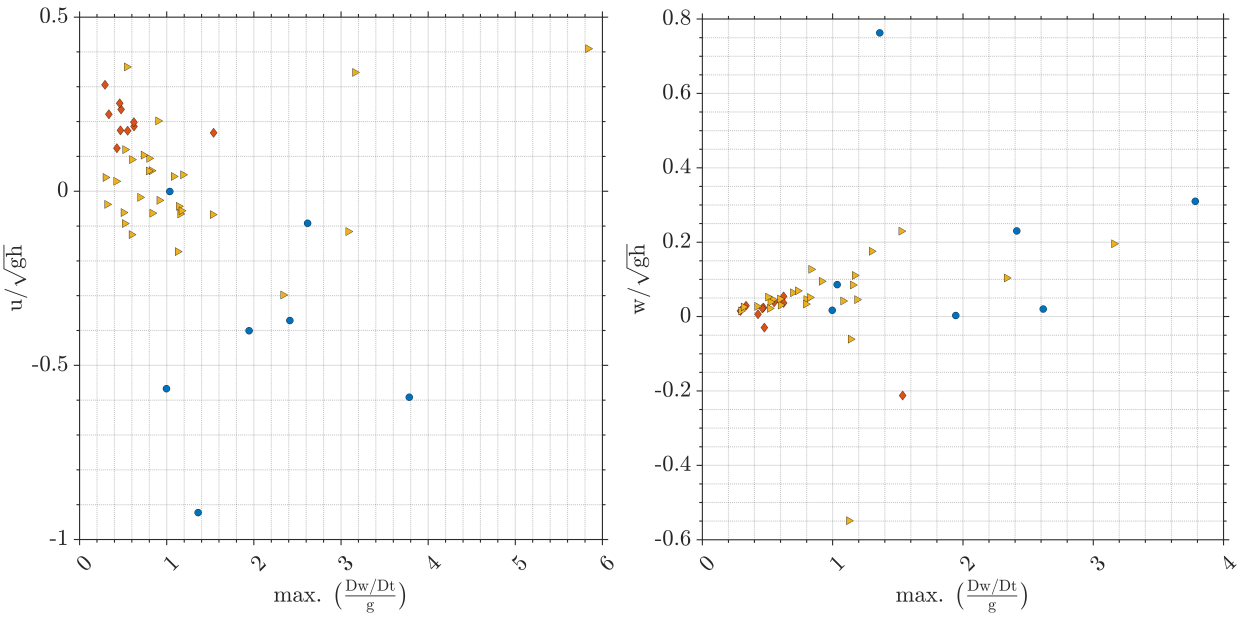

Figure 3.23: Distribution of wave-swash interactions for maximum total vertical accelerations and fluid velocities. (a) Horizontal velocity component. (b) Vertical velocity component. Wave-upwash interaction (diamonds), weak wave-backwash interaction (triangles), strong wave-backwash interaction (circles).

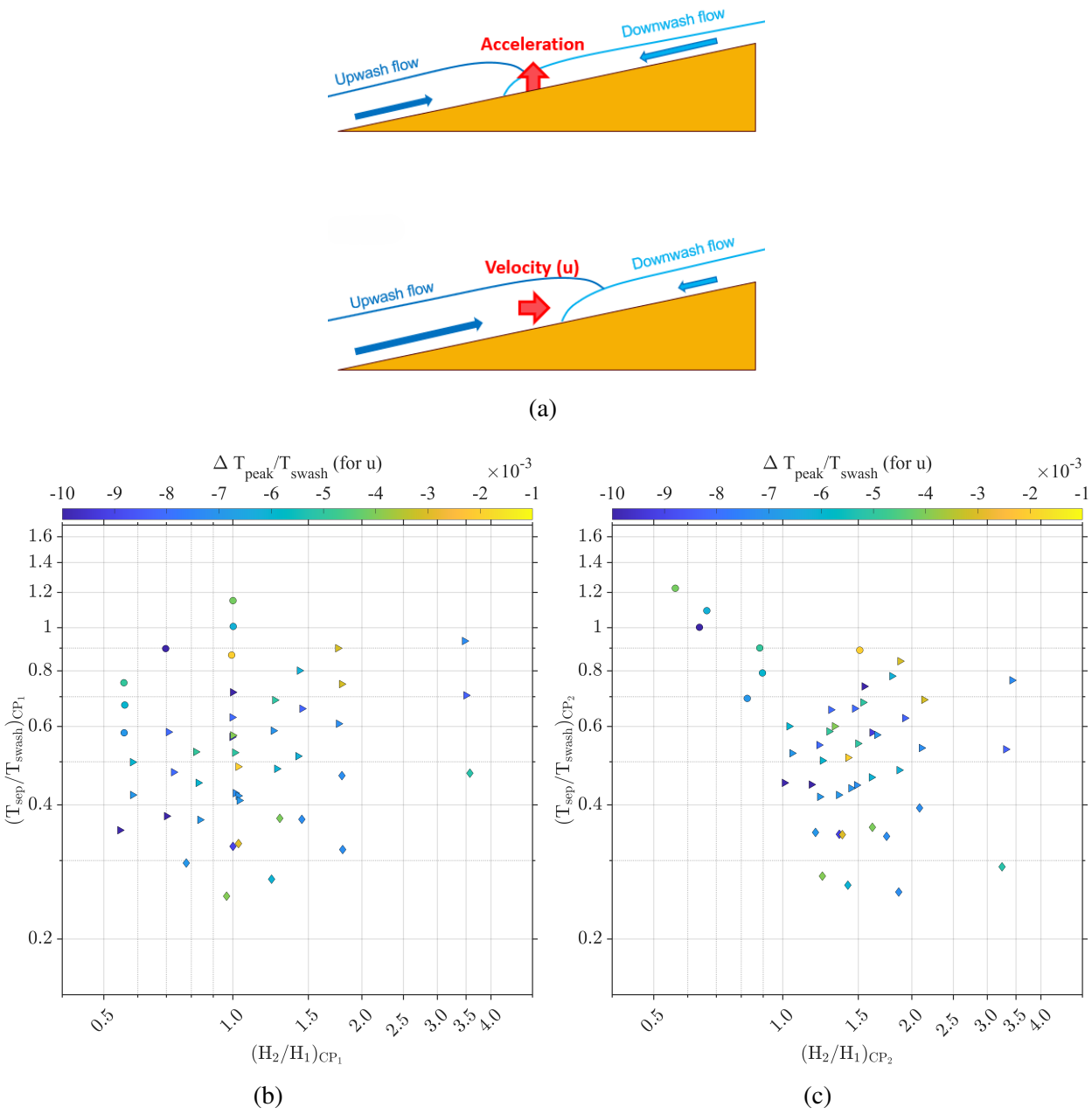

Figure 3.24: Time lag distribution between maximum total horizontal accelerations and maximum velocities for different interactions. Positive values indicate that the peak positive velocity precedes the peak positive acceleration, whereas negative values indicate that the peak acceleration precedes the peak velocity. (a) Scheme of the peak accelerations followed by horizontal velocities. (b) Measurements at CP_1. (c) Measurements at CP_2. Wave-upwash interaction (diamonds), weak wave-backwash interaction (triangles), strong wave-backwash interaction (circles).

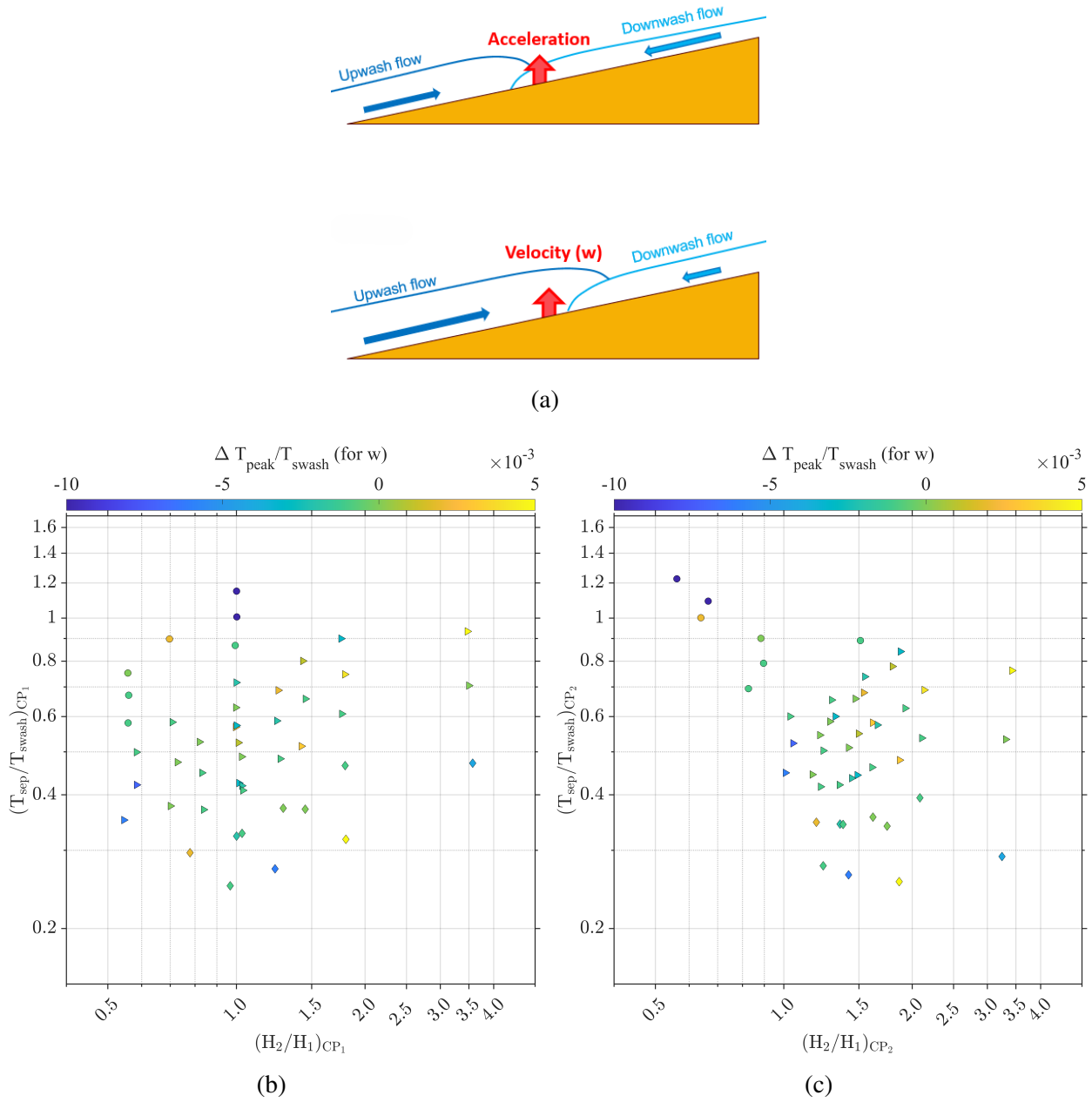

Figure 3.25: Time lag distribution between maximum total vertical accelerations and maximum velocities for different interactions. Positive values indicate that the peak positive velocity precedes the peak positive acceleration, whereas negative values indicate that the peak acceleration precedes the peak velocity. (a) Scheme of the peak accelerations followed by vertical velocities. (b) Measurements at CP_1. (c) Measurements at CP_2. Wave-upwash interaction (diamonds), weak wave-backwash interaction (triangles), strong wave-backwash interaction (circles).

the peak is not necessarily solely dependent on T_{sep} (panels a and b), but the largest peak accelerations occur during the later stages of the swash flow associated with the first wave ($T_{\text{peak}}/T_{\text{swash}} \approx 1$) (panel c).

The final analysis relates to the correlations between the peak vertical accelerations and the flow velocities. Since our interest in vertical accelerations stems from the possibility of inducing large material suspension events, it is important to consider the direction and magnitude of the flow velocity at the same time since that will influence the speed and direction in which suspended material is advected. Figure (3.23) shows the velocity extracted at the time of peak vertical accelerations. The correlation between the peak vertical acceleration and the horizontal velocity is very weak, but interestingly, the vertical velocity at the time of peak vertical acceleration shows a (weak) positive correlation, suggesting that if large vertical accelerations destabilize a sediment bed or flush pore water with dissolved materials out of the bed, the flow field would act to transport that material upwards into the water column.

While the fluid velocity at the time of the vertical acceleration peak is important, the timeseries data in Figures (3.14-3.16) also show that the peak positive horizontal and vertical velocities occur either shortly before or shortly after the peak acceleration. To quantify this, the time lag between the peak upward vertical acceleration and the peak positive fluid velocity is calculated for both components in Figures (3.24-3.25). Positive values indicate that the peak positive velocity precedes the peak positive acceleration whereas negative values indicate that the peak acceleration precedes the peak velocity. The results show that in most cases, the peak vertical acceleration precedes the peak positive (onshore directed) horizontal velocity, suggesting that even if there is not a strong correlation between the horizontal velocity and the vertical acceleration at the moment when the peak acceleration occurs, any material suspended into the water column by the vertical dynamics is prone to be transported onshore shortly after by the horizontal flow.

3.6. Concluding Remarks

In a set of controlled laboratory experiments, solitary waves have been used to generate isolated single swash events (single solitary wave) and wave-swash interactions (consecutive solitary waves). By specifying the wave heights for consecutive solitary waves and the separation between them, it was possible to reproduce the wave-swash interactions found in the field, such as wave-upwash, weak wave-backwash, and strong wave-backwash interactions. The dimensionless parameters that control the wave-swash interactions in our experiments are the ratio of wave heights for consecutive solitary waves (H_2/H_1) and the time separation between them made dimensionless by the swash period of the first wave ($T_{\text{sep}}/T_{\text{swash}}$). When mapped onto this parameter space (H_2/H_1 vs. $T_{\text{sep}}/T_{\text{swash}}$), the different qualitative wave-swash interaction types formed distinct clusters, suggesting that these dimensionless parameters are sufficient to capture the observed variations in the field.

The main focus of the study was on the vertical accelerations, which were estimated from the differences between the depth measured with a surface wave gauge and the depth inferred from pressure measurements at the bed. While large vertical accelerations were associated with strong wave-backwash interactions, it was found that weak wave-backwash interactions were associated with equally large vertical accelerations. The largest vertical accelerations were associated with wave-swash interactions that spanned $0.5 < H_2/H_1 < 2$ and $0.6 < T_{\text{sep}}/T_{\text{swash}} < 1.2$, where the vertical accelerations commonly exceeded the acceleration of gravity.

Finally, the time lag between the maximum vertical acceleration and the maximum onshore horizontal and upward vertical velocity was analyzed. The peak values of the vertical accelerations lead the peak onshore velocities and tend to be almost concurrent with the peak upward velocities. This suggests that wave-swash interactions may be an effective mechanism by which material such as sediment or solutes within sediment pores is suspended into the water column by the vertical dynamics before being advected onshore by the horizontal dynamics.

Overall, the findings presented in this work show that non-hydrostatic effects, which are typically ignored in modeling coastal flows in the very shallow waters of the inner-surf and swash

zones, are important in wave-swash interactions. Further, the analyses and results lead to hypothesize that these vertical accelerations are sufficiently large such that they could lead to local liquefaction of sediment and hence produce large sediment transport events that may have an outsized influence on the net erosion or accretion of the beach foreshore region. Laboratory (Alsina et al., 2018) and field (Florence et al., 2022) studies have shown sediment suspension and transport consistent with this mechanism. Our framework of analyzing isolated wave-swash interaction events, understanding their region of influence, and quantifying the vertical accelerations provide a framework with which to investigate the possibility of sediment liquefaction and large sediment suspension events in the laboratory.

Future work on this matter could investigate how the dynamics observed in these experiments vary across the inner surf and swash zones, as our data is from a single control point. Including sediment in the experiments is a central goal for future studies to directly observe sediment suspension events triggered by wave-swash interactions, which can be significant.

Experimentally, modifying the forcing conditions to model interactions with different waves could extend the understanding of wave-swash interactions. Analysis and characterization of wave-swash interactions associated with irregular waves generated by some specific wave spectra could reveal and demonstrate that the relations between successive wave amplitudes and separation times are also extensible and functional for these kinds of waves.

Information on runups developed after wave-swash interactions is not quantified in this work. However, observing how the runups distribute in terms of the proposed characteristic ratios can hint at new experimental formulations for runups associated with successive solitary waves on planar slopes.

Computational Fluid Dynamics modelling could help to extend the investigations presented here to include different beach conditions, such as slopes and roughnesses, forcing conditions to try multiple wave amplitudes and several types of waves (regular, irregular, more than two consecutive solitary waves, etc.) with associated separation times. The data presented in this dissertation are considered high-quality experimental information, which can be helpful for the calibration and

validation of the numerical experiments. Future works can make use of this initial experimental set of data to be implemented numerically and later modified to include different conditions.

Chapter 4

RUNUP INDUCED BY A TRAIN OF SUCCESSIVE SOLITARY WAVES IN A DIRECTIONAL WAVE BASIN

4.1. Introduction

It has been observed that wave-swash interactions are continuously present on the coast and can initiate different physical processes, whose understanding and analyses are a matter of study. As incoming waves can arrive at nearshore areas with different angles, the behavior and characteristics of the wave-swash interactions can be modified only by the wave obliquity, modifying the flows and coastal processes (i.e. Cross and long-shore sediment transport).

Following the considerations presented previously, experiments comprising wave-swash interactions generated with different angles of incidence are run in the directional wave basin of Oregon State University. The experimental cases consider wave trains of two (2) successive solitary waves with different amplitudes and variations in the separation times of the consecutive events. These experimental cases, which correspond to weak wave-backwash interactions (WWBI), were combined with two (2) different angles of incidence for the transient waves, 0° and 15°. Similarly to the works performed by Lo et al. (2013) and Wu et al. (2021, 2022), the analysis of the developed runup conditions after the interaction in the swash for different angles of incidence is presented. Flows and runups generated by the wave-swash interactions reaching the coast with different angles of incidence are analyzed and quantified in terms of two dimensionless ratios constructed from the surface elevations of the consecutive waves and their separation time.

4.2. Experimental setup

The experiments were performed in the directional wave basin of the Oregon State University, whose dimensions are 48.8 m in length, 26.5 m in width, and 2.1 m in height. The basin was equipped with a snake-type wave maker system, which is made of 29 boards with up to 2.1 m long stroke each. At the other end, the basin has a beach of slope 1:10 made of concrete, over which an arrangement of synchronized instruments was set to collect the information of the wave conditions, such as surface elevations and flow velocities (Figure (4.1)). Wire wave gauges (WG) OSU In-House built, and Ultrasonic Wave Gauges (USWG; Senix ToughSonic-3 with 1 mm accuracy) were located at different depths of the basin. For these instruments, a calibration was performed daily to ensure good quality in the data acquisition.

In the swash, wave gauges were co-located with side-looking Acoustic Doppler Velocimeters (ADVs; Nortek Vectrino Plus with an accuracy of 1% FS) with a sampling frequency of 100 Hz. Figure (4.2) shows the location of the instruments in the basin. For these instruments, the signal-to-noise ratio (SNR = 13) and correlation value (CORR=18) were considered high enough to account with reliable data for the analyses across cases.

Two (2) cameras were also configured to record videos of each experimental realization. At the wave generation the water depth $h = 0.8$ (m) (constant depth). The origin of the left-handed coordinate system used in the experimental setup is set at the still water line (SWL) on the beach, here x points to the north (N, or onshore according to the top view of the wave basin), y points East (E), and z pointing upwards. The control point at the swash for the collection of surface elevations (ζ), and velocities (u, v, w), is located at ADV$_1$ ($x = -1.092$ (m) to the SWL), before the first wave breaks. A second control point for surface wave elevation (ζ) is located at WG2 ($x = -11.998$ (m) to the SWL). This location is to assess the performance of the wave generation. The experimental cases considered in this work are presented in Table (4.1), which presents the parameters in dimensional and dimensionless form. For all four (4) cases, the first wave remains the same, and the interactions in the swash correspond to weak wave-backwash interactions.

Figure 4.1: Image of the instrument arrangement in the directional wave basin.

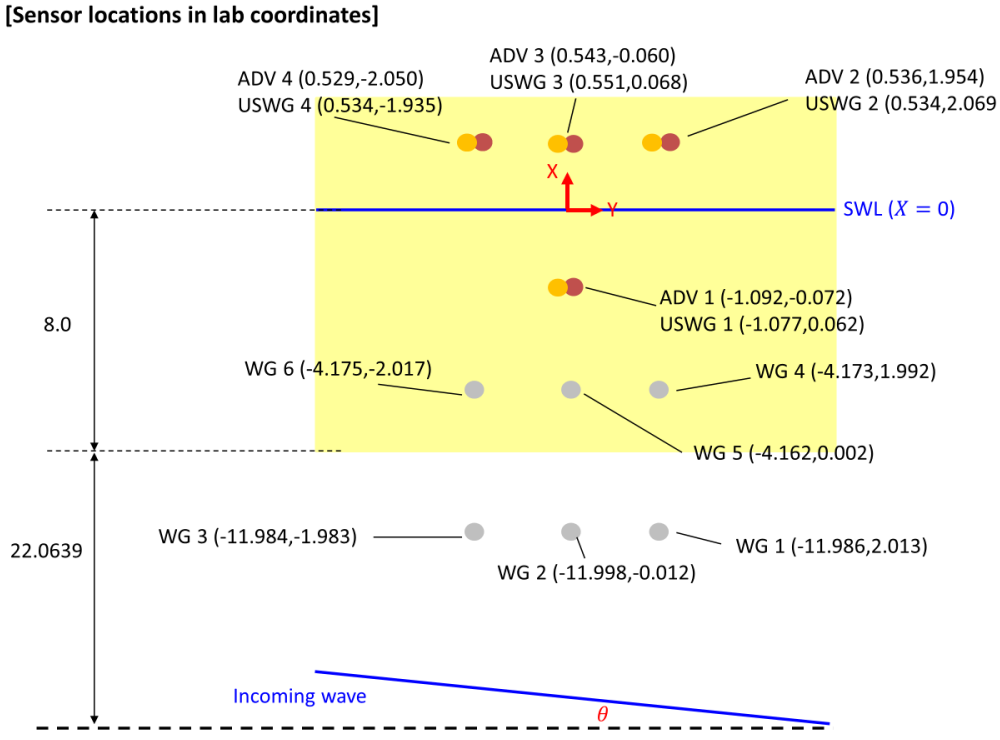

Figure 4.2: Experimental setup in the directional wave basin.

Table 4.1: Experimental cases.

Case	H_1 (m)	H_2 (m)	T_{sep} (s)	H_1/h	H_2/h	$T_{sep}/\sqrt{h/g}$	θ (deg)	s	Type
1	0.16	0.24	3.54	0.2	0.3	12.4	0	1/10	WWBI
2	0.16	0.24	3.54	0.2	0.3	12.4	15	1/10	WWBI
3	0.16	0.32	3.14	0.2	0.4	11.0	0	1/10	WWBI
4	0.16	0.32	3.14	0.2	0.4	11.0	15	1/10	WWBI

4.3. Validation and data reproduction

To assess the performance of the wave generation for the waves in the directional wave basin, the surface elevation of consecutive solitary waves at a constant depth (WG_2) was compared against the theoretical results of solitary wave considering Boussinesq theory for small amplitude solitary waves (Boussinesq, 1872). Figure (4.3) shows the comparison of the surface elevations at WG2, which presents an excellent agreement between the signals. This validation of the wave generation ensures reliability to the wave-swash interactions development in the swash.

Each experimental case was repeated ten (10) times to verify the reproducibility of the surface elevations and fluid velocites. Figure (4.4-4.5) shows the time series of measurements for these quantities in the swash (ADV_1). No significant discrepancies are observed in the repetitions of the time series, confirming reliability and robustness in the experimental reproduction. Ensembled surface elevations and velocities were constructed by averaging the time series across repetitions to obtain a single representative time series for each experimental case. Figure (4.6) shows an example of the ensembled time series of elevations and velocities over all the trials performed for experimental case 1.

4.4. Wave-swash interactions-induced flows

Flows induced by the wave-swash interactions are analyzed and quantified in terms of the characteristic wave and temporal ratios, H_2/H_1, and $T_{sep}/\sqrt{h/g}$, constructed from the experimental

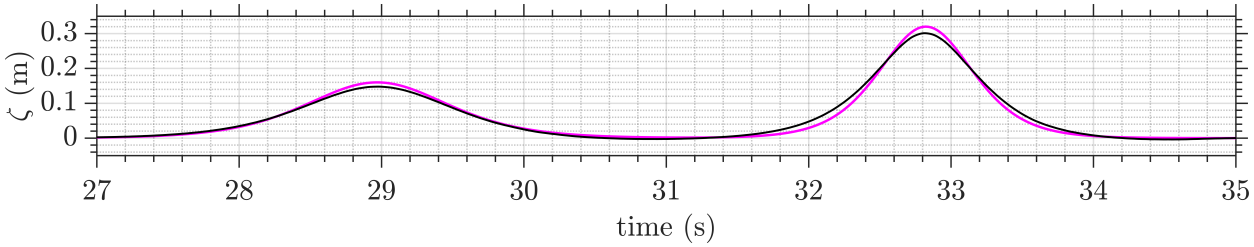

Figure 4.3: Wave generation performance. Boussinesq theoretical surface elevation (black solid line), measured surface elevation (magenta solid line).

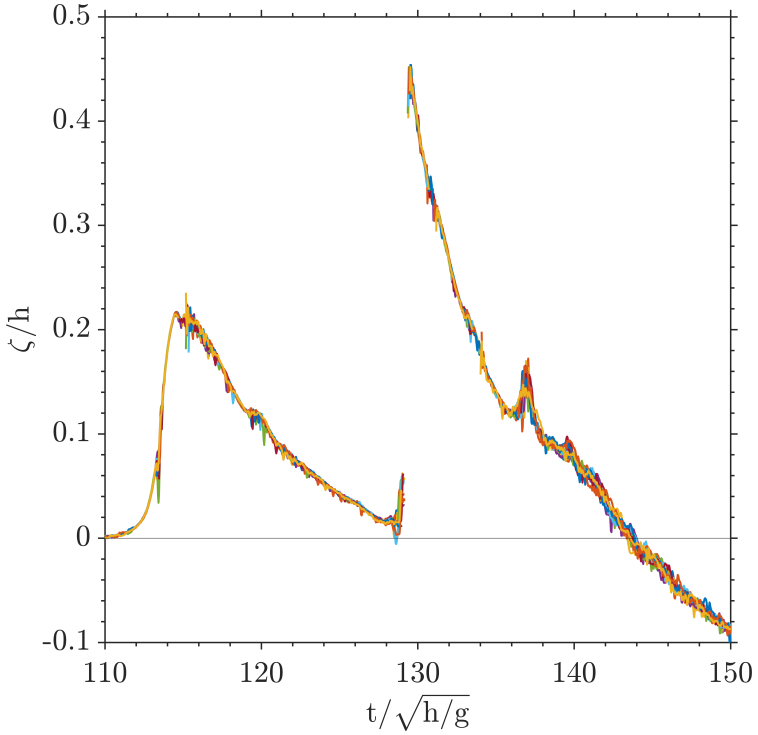

Figure 4.4: Experimental repetitions of surface elevations measured at ADV_1 for Case 1.

parameters. For the analyses, the time series of the ensembles are considered in the analyses as they are representative of the flows for the different experimental cases. To improve the quality of the time series, a despiking method stated by Goring and Nikora (2002) was applied, eliminating unrealistic spikes from the time series. Figure (4.7) shows the surface elevations for the different experimental cases after the despiking process. From the signals, there is a noticeable reduction

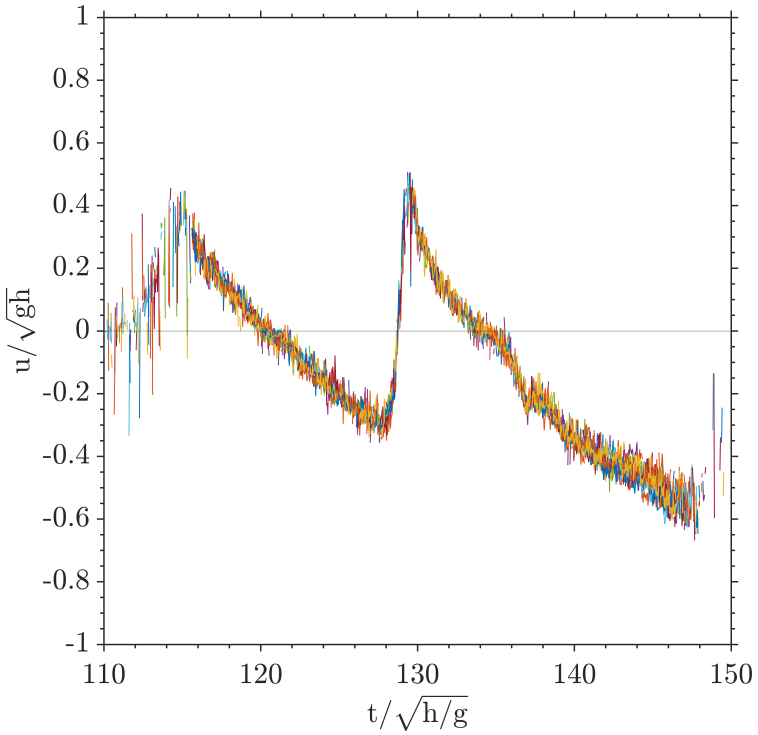

Figure 4.5: Experimental repetitions of fluid velocities measured at ADV_1 for Case 1.

in the wave amplitude as the wave angle increases, remarking an energy loss due to the wave obliquity. However, this is more evident when $T_{sep}\sqrt{h/g}$ is longer.

Cross-shore, long-shore, and vertical velocities are shown in Figures (4.8-4.11). For interactions with the same wave and temporal ratios, it is possible to observe how the velocity magnitudes decrease at the arrival of the second wave as the wave angle increases, especially for the cross-shore velocity, $u/\sqrt{gh}$. Conversely, long-shore velocities present increasing positive magnitudes at the moment of the interaction associated with wave obliquity. This latter hints at a potential increment in the sediment transport alongshore related to the angle of incidence. Even when the behavior is not clear, vertical accelerations display some positive trend at the moment of the interaction, which is more noticeable for cases with no obliquity.

Maximum fluid velocities and local accelerations at the moment of the wave-swash interactions are shown in terms of the characteristic ratios in Figures (4.12-4.13). Accelerations were calculated from the positive velocity slope at the arrival of the second wave. For specific interacting

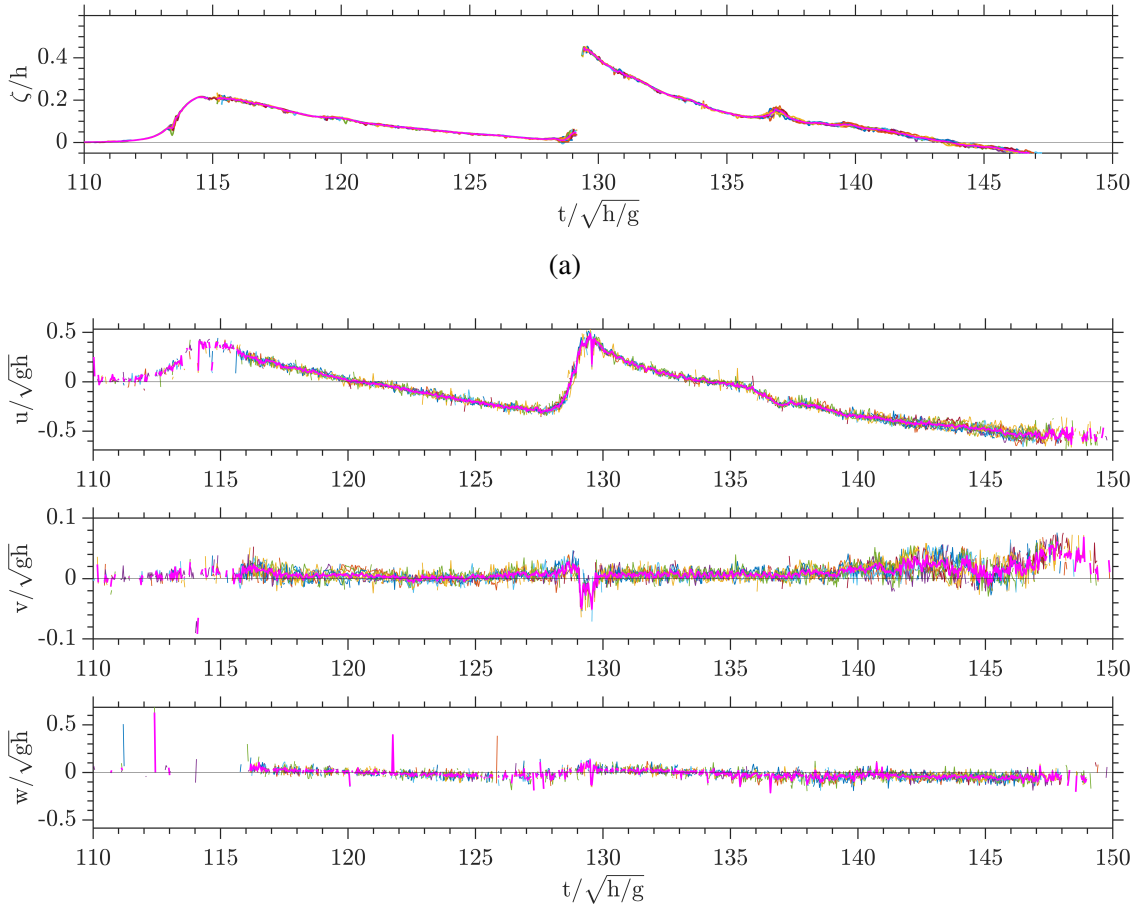

(a)

(b)

Figure 4.6: Ensembles of surface elevations (a) and fluid velocities (b) at ADV_1. Case: $H_2/H_1 = 1.5$; $T_{sep}/\sqrt{h/g} = 12.4$; $\theta = 0°$.

cases, maximum cross-shore velocities and accelerations decrease with an increasing angle of incidence, but larger magnitudes are associated with shorter separation times and larger wave height ratios. It is important mentioning that the observed decrease in the magnitudes is an effect of the wave refraction. On the other hand, long-shore and vertical velocities and accelerations present a remarked augment with wave obliquity. In general, the velocities exhibit that higher magnitudes are associated with shorter separation times and larger wave height ratios, showing the influence of amplitude of the second wave.

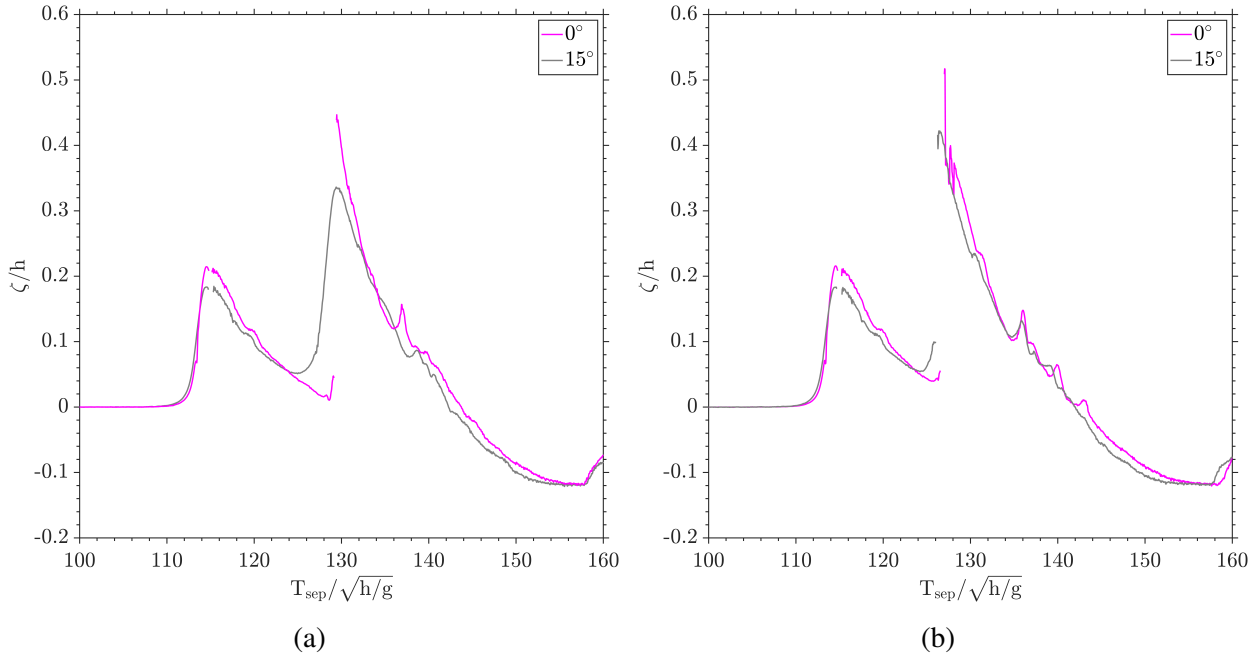

Figure 4.7: Surface elevations measured at ADV$_1$. (a) $H_2/H_1 = 1.5$; $T_{sep}\sqrt{h/g} = 12.4$, (b) $H_2/H_1 = 2.0$; $T_{sep}\sqrt{h/g} = 11.0$.

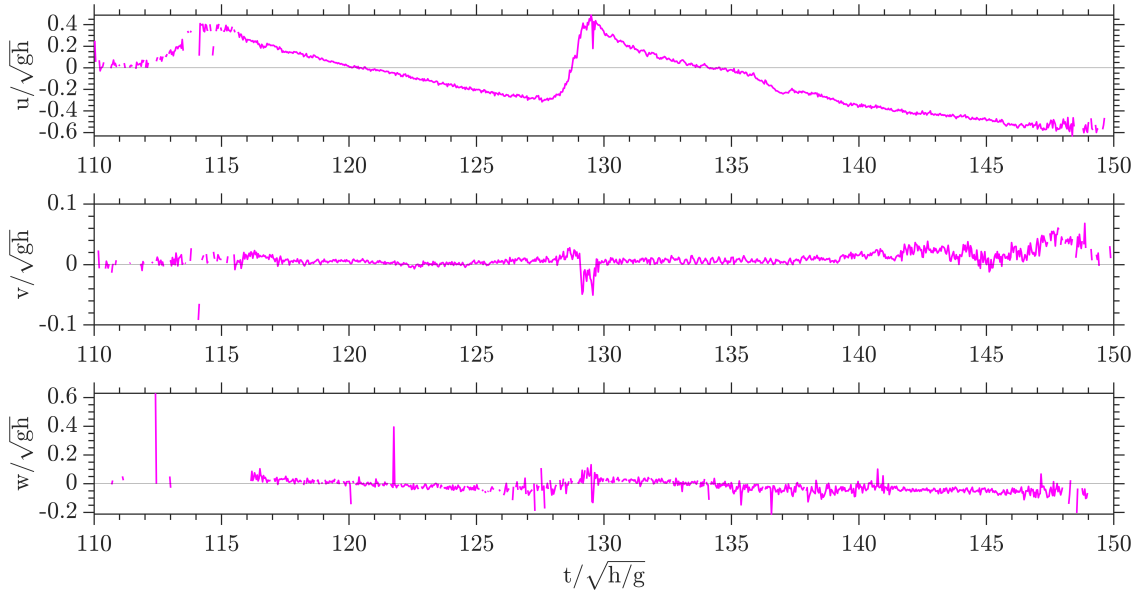

Figure 4.8: Velocities at ADV$_1$. $H_2/H_1 = 1.5$; $T_{sep}/\sqrt{h/g} = 12.4$; $\theta = 0°$.

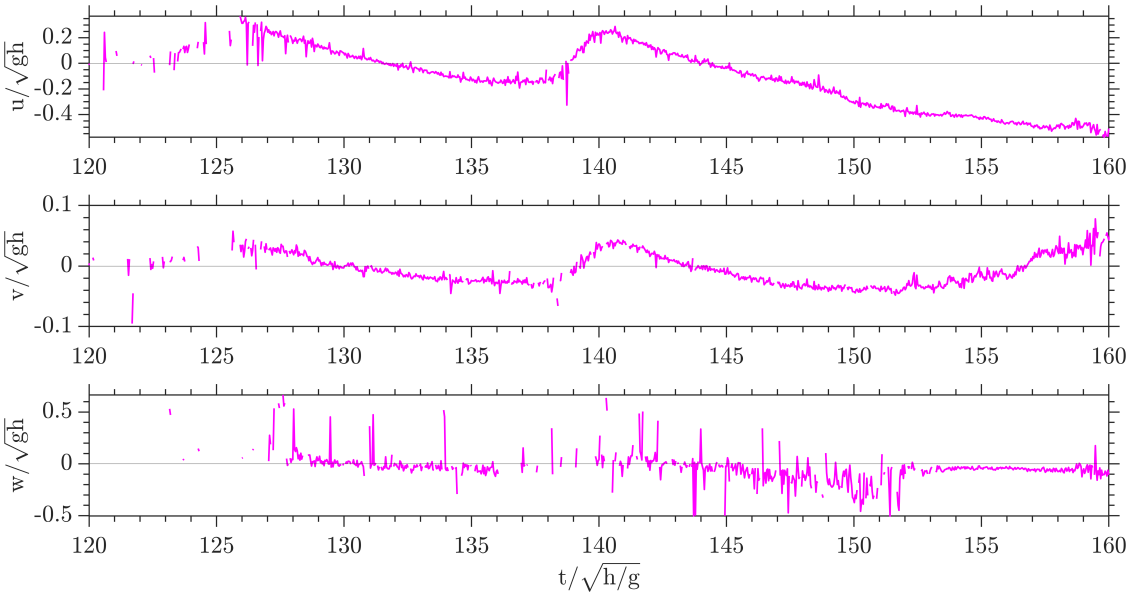

Figure 4.9: Velocities at ADV$_1$. $H_2/H_1 = 1.5$; $T_{sep}/\sqrt{h/g} = 12.4$; $\theta = 15°$.

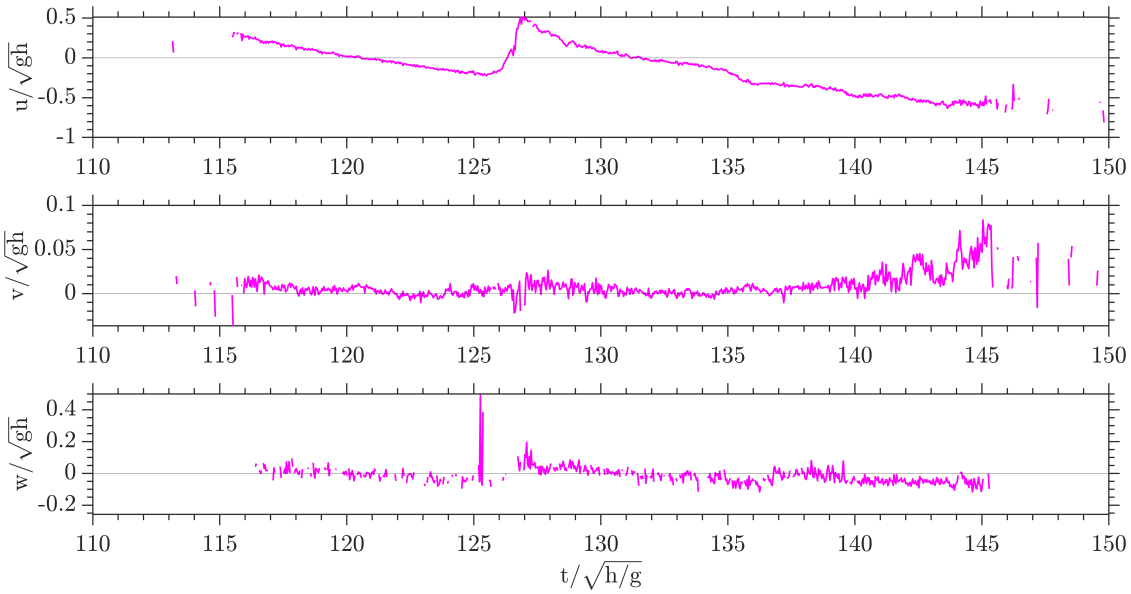

Figure 4.10: Velocities at ADV$_1$. $H_2/H_1 = 2.0$; $T_{sep}/\sqrt{h/g} = 11.0$; $\theta = 0°$.

4.5. Runup estimation

For the experiments, runup is calculated using image analysis from video recordings. Images of size 1280 x 720 pixels are extracted from video recordings to generate image stacks covering

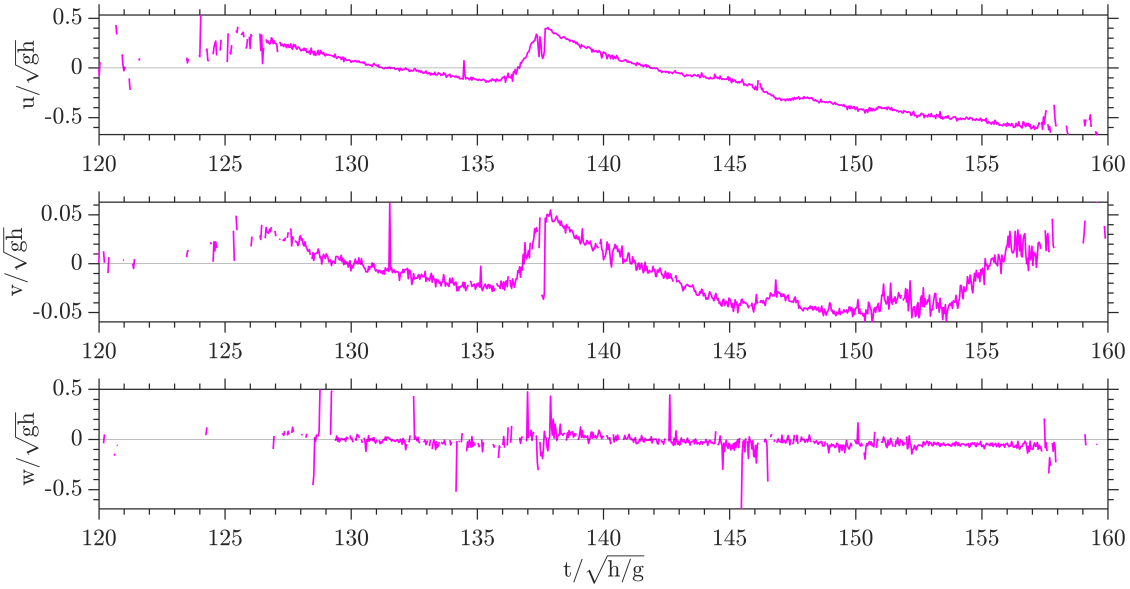

Figure 4.11: Velocities at ADV$_1$. $H_2/H_1 = 2.0$; $T_{sep}/\sqrt{h/g} = 11.0$; $\theta = 15°$.

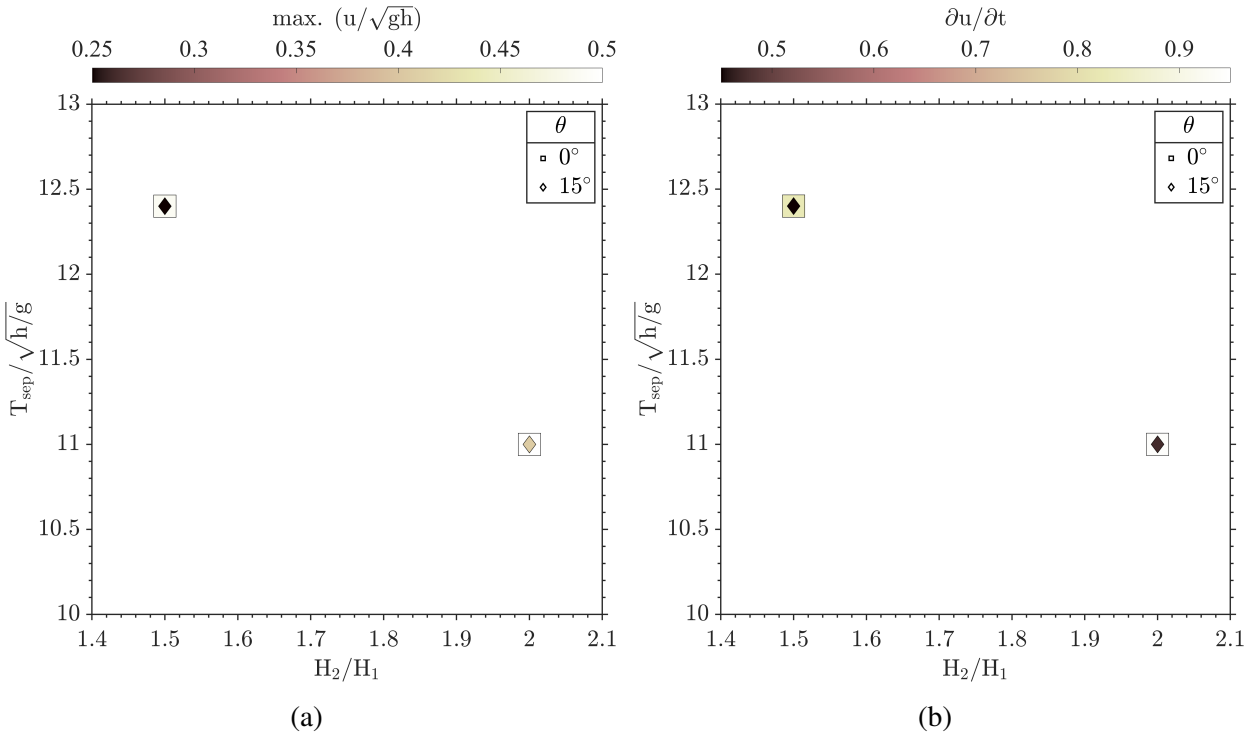

Figure 4.12: Maximum cross-shore velocities (a) and local accelerations (b) for H_2/H_1 vs. $T_{sep}/\sqrt{h/g}$.

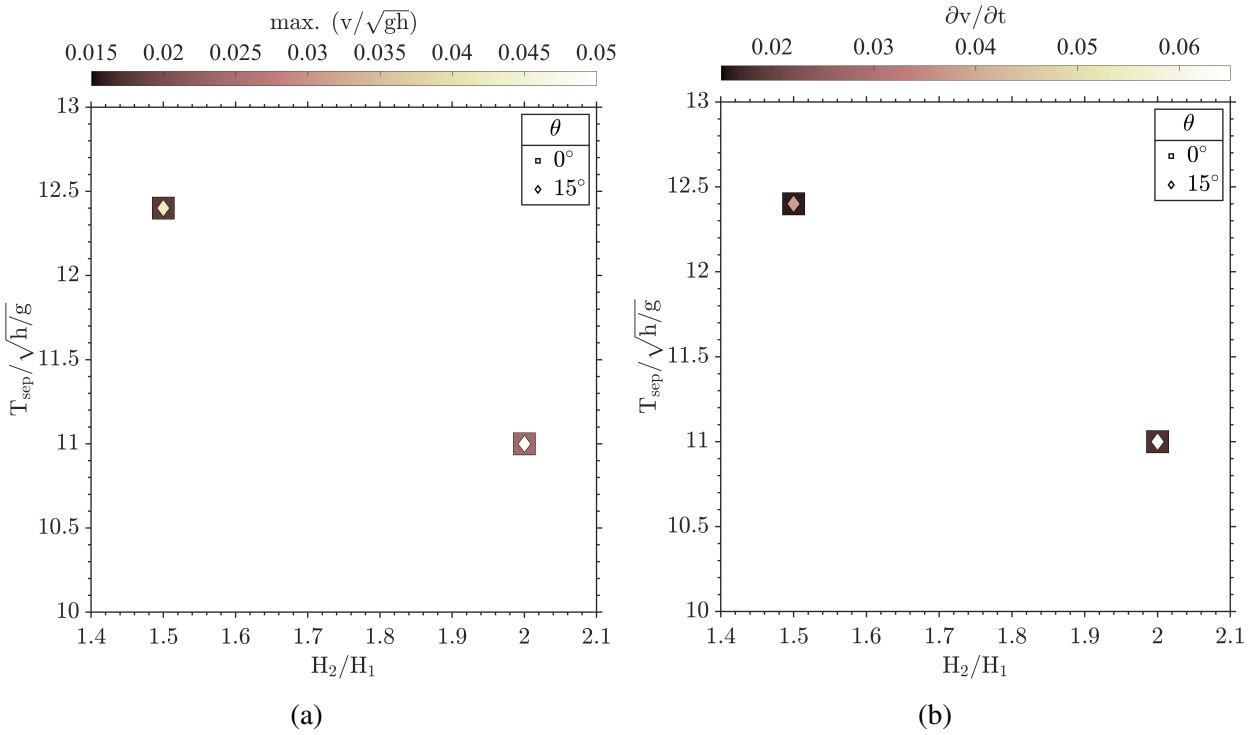

Figure 4.13: Maximum long-shore velocities (a) and local accelerations (b) for H_2/H_1 vs. $T_{\text{sep}}/\sqrt{h/g}$.

the whole runup-rundown process, which is identified later by inspection. In the figures, each pixel is equivalent to 1 (cm) by 1 (cm), allowing a fine resolution to estimate the runups accurately. Figure (4.15) shows the maximum runup over the beach after the arrival of the first and second solitary waves for experimental case 3. It is possible to notice that the raw pictures (from the videos) are collected from a side-looking position to the swash, difficulting the correct estimation of the distance traveled by the water over the beach from the still water line (SWL). To overcome this, a rectification process is applied to each image to obtain an orthogonal top view of the swash (Brown, 1992). With this, it is possible to obtain a top view of the pictures.

Figures (4.16) and (4.17) present an example of the rectification process for the first and second runup for experimental case 3. Table (4.2) presents the results of the runups for all the experimental cases.

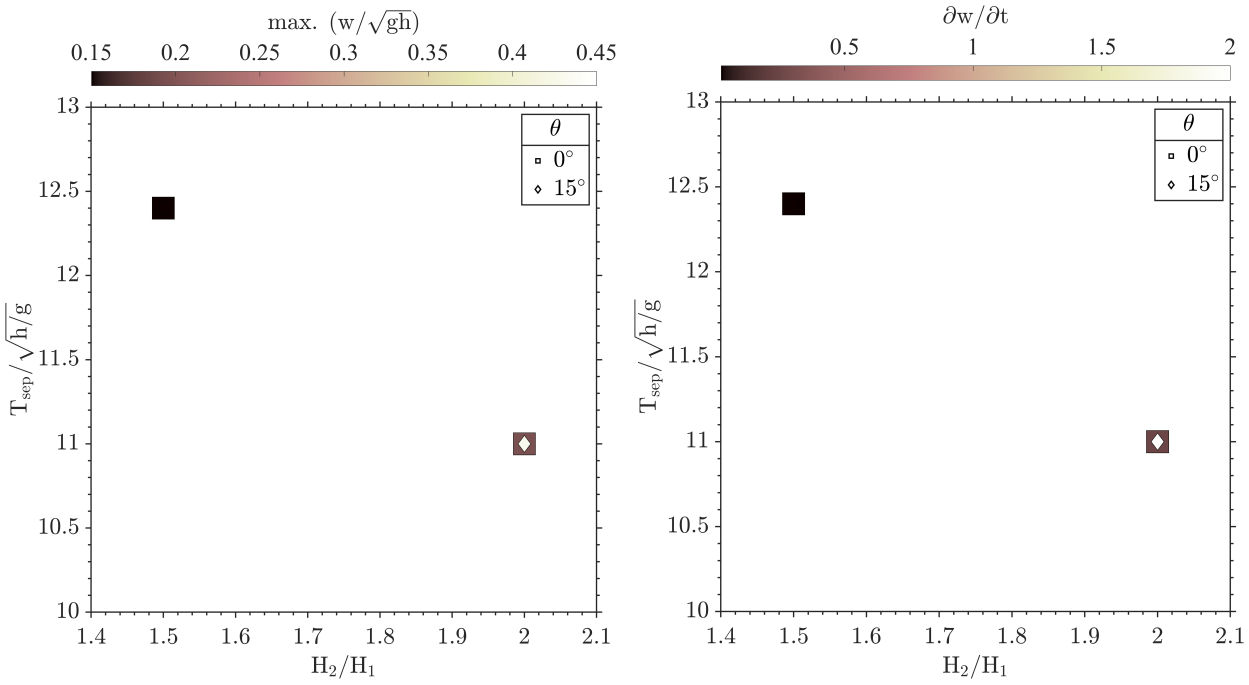

Figure 4.14: Maximum vertical velocities (a) and local accelerations (b) for H_2/H_1 vs. $T_{\text{sep}}/\sqrt{h/g}$.

Table 4.2: Experimental runups.

Case	H_1/h	H_2/h	$T_{\text{sep}}/\sqrt{h/g}$	θ°	R_1/h	R_2/h
1	0.2	0.3	12.4	0	0.649	0.644
2	0.2	0.3	12.4	15	0.580	0.580
3	0.2	0.4	11.0	0	0.635	0.636
4	0.2	0.4	11.0	15	0.556	0.555

4.5.1. Runup comparison against theoretical formulations

There is an interest in understanding the breaking conditions for the first wave of the train of solitary waves. Following the criteria stated by Lo et al. (2013), the surf similarity parameter for solitary waves corresponds to

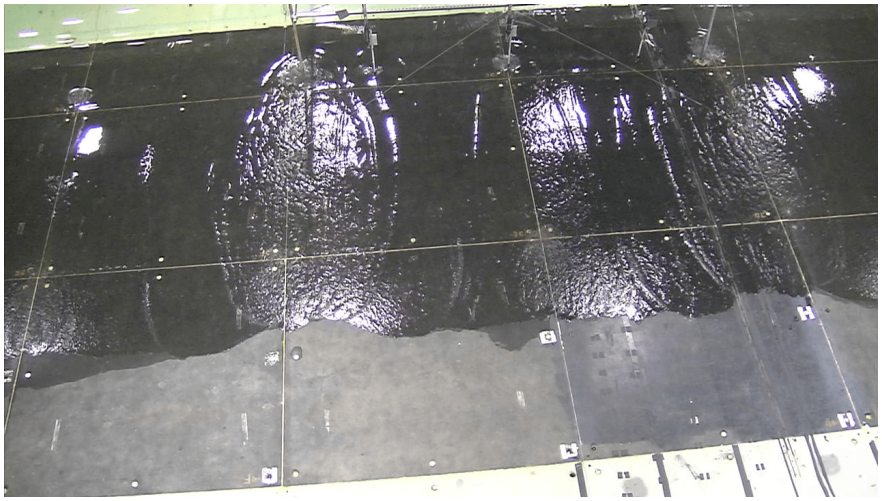

(a)

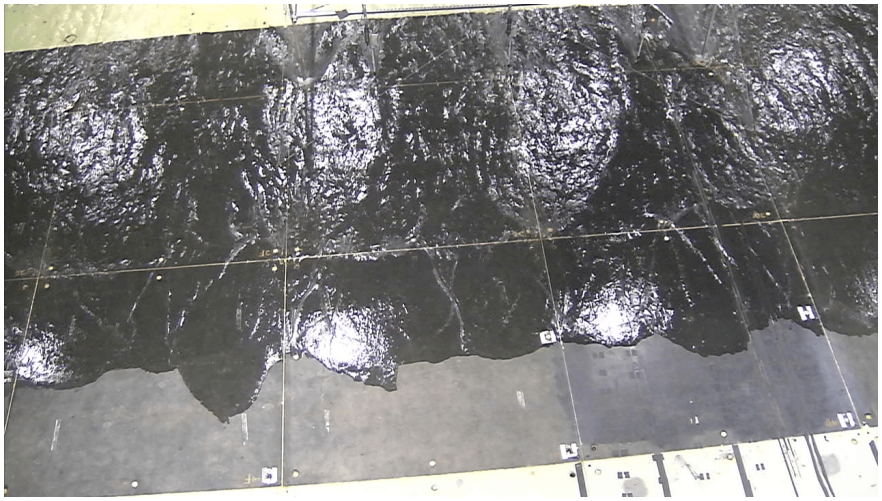

(b)

Figure 4.15: First (a) and second (b) wave runups recorded for the experimental $H_2/H_1 = 2.0$; $T_{sep}/\sqrt{h/g} = 11.0$; $\theta = 15°$ (Case 3).

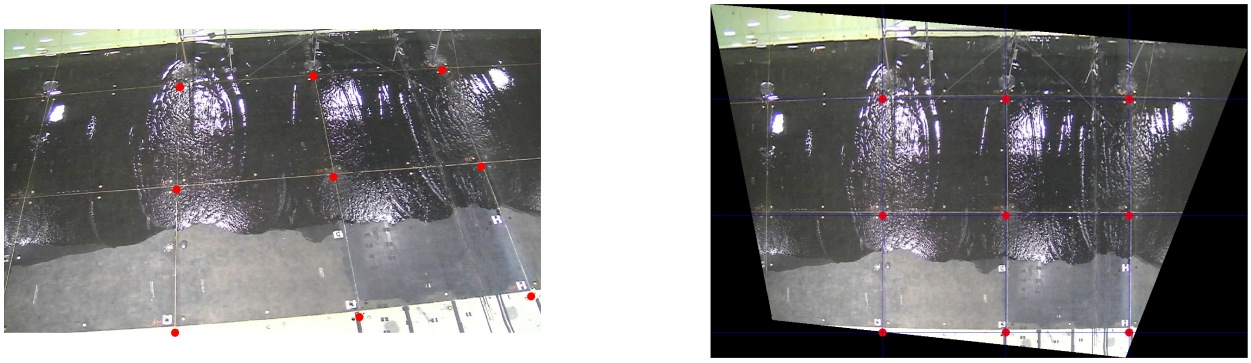

Figure 4.16: Experimental case $H_2/H_1 = 2.0$; $T_{sep}/\sqrt{h/g} = 11.0$; $\theta = 15°$ (Case 3). First wave runup. Unprocessed image (left), rectified image (right).

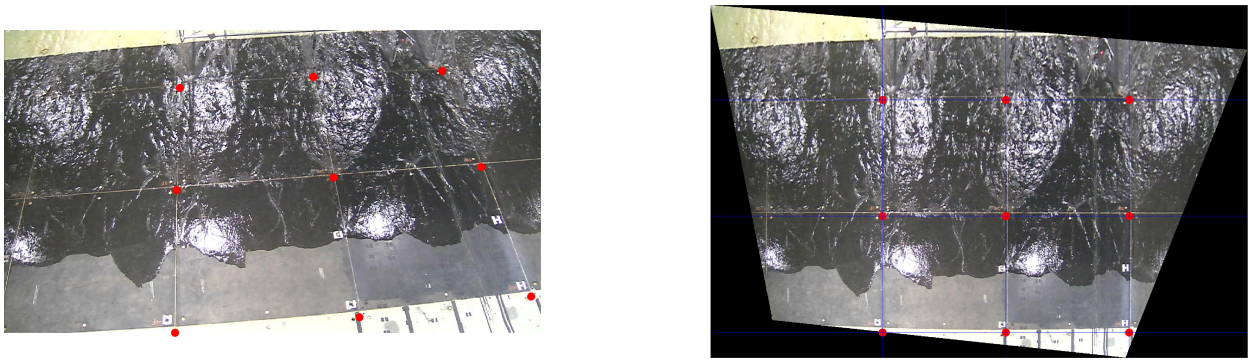

Figure 4.17: Experimental case $H_2/H_1 = 2.0$; $T_{sep}/\sqrt{h/g} = 11.0$; $\theta = 15°$ (Case 3). Second wave runup. Unprocessed image (left), rectified image (right).

$$\xi_s = s\left(\frac{H_1}{h}\right)^{-\frac{9}{10}} \tag{4.1}$$

where s stands for the beach slope, and H_1 and h are the constant depth wave height and depth. It is straightforward calculate that for all the experimental cases tried here the first incoming wave are breaking, and $\xi_s = 0.426$.

To understand the validity of the measurements, the experimental runups are compared against the formulation for breaking solitary waves on rough slopes proposed by Wu et al. (2018)

$$\frac{R_1}{\gamma H_1} = \frac{4.50(\xi_s)^{1.52}}{0.04 + (\xi_s)^{1.19}}, \tag{4.2}$$

valid for a surf similarity parameter $\xi_s < 1.2$, according to Synolakis (1987). Assuming a roughness height of 0.5 mm for the beach made of concrete, a the reduction factor $\gamma = 0.94$ is considered. The theoretical and experimental runup estimations for the first incoming wave are presented in Table (4.3).

Table 4.3: Experimental and theoretical runups.

Case	θ°	R_1/H_1	$R_1/\gamma H_1$ (Eq. (4.2))	Diff. (R_1) (%)
1	0	3.245	3.058	5.76
2	15	2.90	3.058	-5.45
3	0	3.175	3.058	3.69
4	15	2.78	3.058	-10.0

Results show that even in the cases where the same waves propagate with no obliquity (Cases 1 and 3), there is a reduction in the runup of about $\sim$2.1% when they are expected to be similar. According to Lo et al. (2013), it is assumed the separation time elapsed between the solitary waves can influence the runup of the first wave. However, the magnitude of the second incoming wave can modify a previously defined separation time, so its consideration can also contribute to the observed differences. Based on this, the runup associated with the second wave after the interaction is calculated from the following equation proposed by (Lo et al., 2013) for successive waves, which includes the separation time. The formulation considered is as follows

$$R_2 = [f(\xi_s) + 1]R_1, \tag{4.3}$$

where

$$f(\xi_s) = \frac{175\xi_s^{-0.22} - 199\xi_s^{-0.16}}{1 + 169\xi_s^{5.5}} \tag{4.4}$$

and

$$\xi_s = s\left(\frac{H_1}{h}\right)^{-\frac{9}{10}}\left(\frac{T_{\text{sep}}}{\sqrt{h/g}}\right). \tag{4.5}$$

According to this formulations, the runup associated with the second wave are estimated and presented in Table (4.4).

Table 4.4: Experimental and theoretical runup for the second wave.

Case	θ°	R_2/H_2	R_2/H_2 (Eq. (4.3))	Diff. (R_2) (%)
1	0	2.147	1.916	12.05
2	15	1.933	1.916	-0.88
3	0	1.590	1.437	10.64
4	15	1.388	1.437	-3.53

Figure 4.18 presents the runup variability in terms of the angle of incidence θ. The differences are mainly attributed to the fact that waves dissipate energy due to diffraction in the propagation process, reducing the wave height before the breaking, and restricting the flow to advance longer distances over the beach slope to reach higher runup elevations. A summary of the estimated runups and their relation is presented in Table (4.5). According to these findings, a modification of the proposed runup equation to include the effects of the obliquity will be necessary for a more accurate runup estimation.

Table 4.5: Summary of the measured runups and their relation.

Case	θ°	R_1/H_1	R_2/H_2	R_2/R_1
1	0	3.245	2.147	0.9924
2	15	2.90	1.933	0.9998
3	0	3.175	1.590	1.0015
4	15	2.78	1.388	0.9985

4.5.2. Runups after the wave-swash interaction

Runups for the first and second incoming waves are analyzed in terms of the characteristic ratios H_2/H_1, and $T_{\text{sep}}/\sqrt{h/g}$ to observe the potential relation to the wave-swash interactions and angles of incidence. Runups for the two incoming solitary waves are analyzed independently, displaying similar magnitudes. From Figure (4.19), it is possible to observe that higher runup

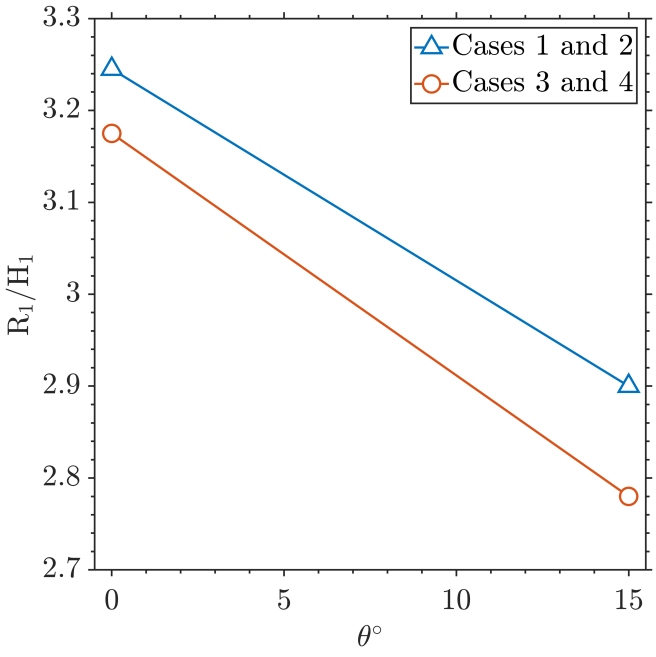

(a)

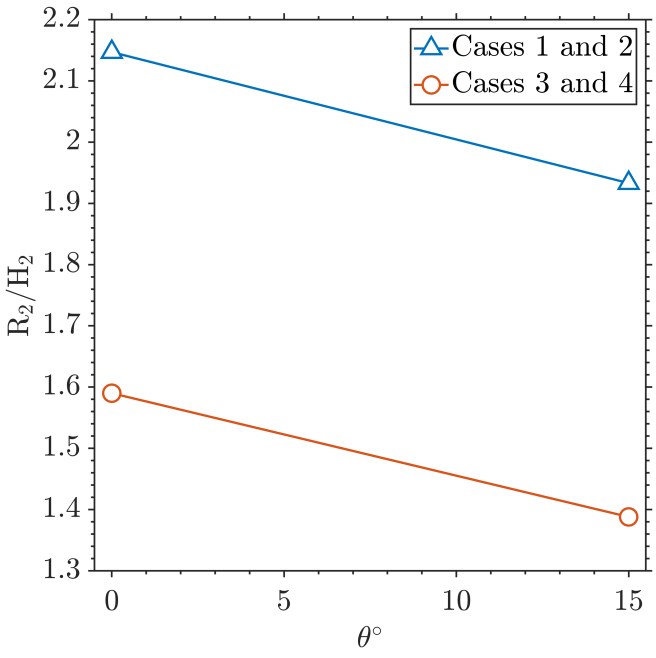

(b)

Figure 4.18: Runup as function of the wave obliquity. Solitary wave 1 (a) and solitary wave 2 (b).

elevations are mainly associated with wave trains with no wave obliquity, regardless of the wave height or separation time ratios. For these cases, however, T_{sep} hints to be more significant on the maximum runup magnitude. Figure (4.20) shows the relation between the estimated runups.

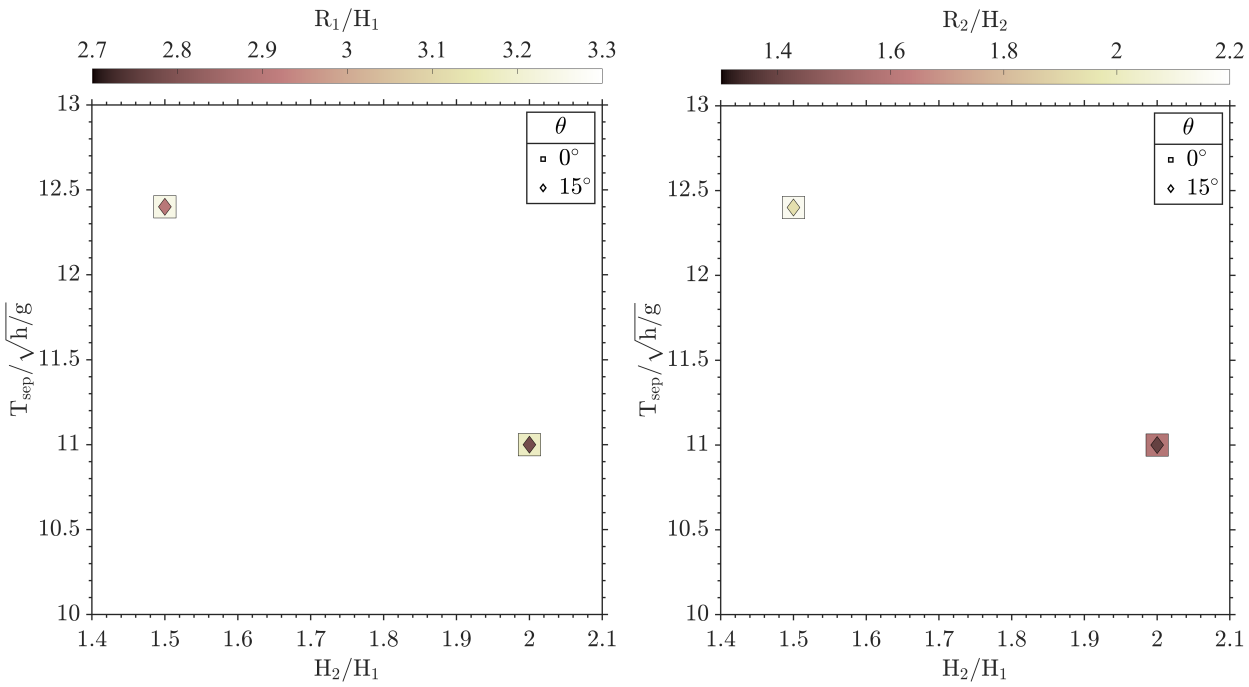

Figure 4.19: Runup for solitary wave 1 (a) and solitary wave 2 (b) in terms of the characteristic ratios.

4.6. Concluding remarks

A set of experiments was conducted at the directional wave basin of Oregon State University to analyze the influence of the wave obliquity on fluid flows and runups. The experiments consider controlled cases of two consecutive solitary waves of different amplitudes separated by a specific separation time. Each experimental case is combined with two angles of incidence, $\theta = 0°$ and $15°$. Fluid flows and surface elevations measured at the swash present consistency for each experimental realization, allowing the generation of a single ensembled signal representative of elevations and velocities to analyze.

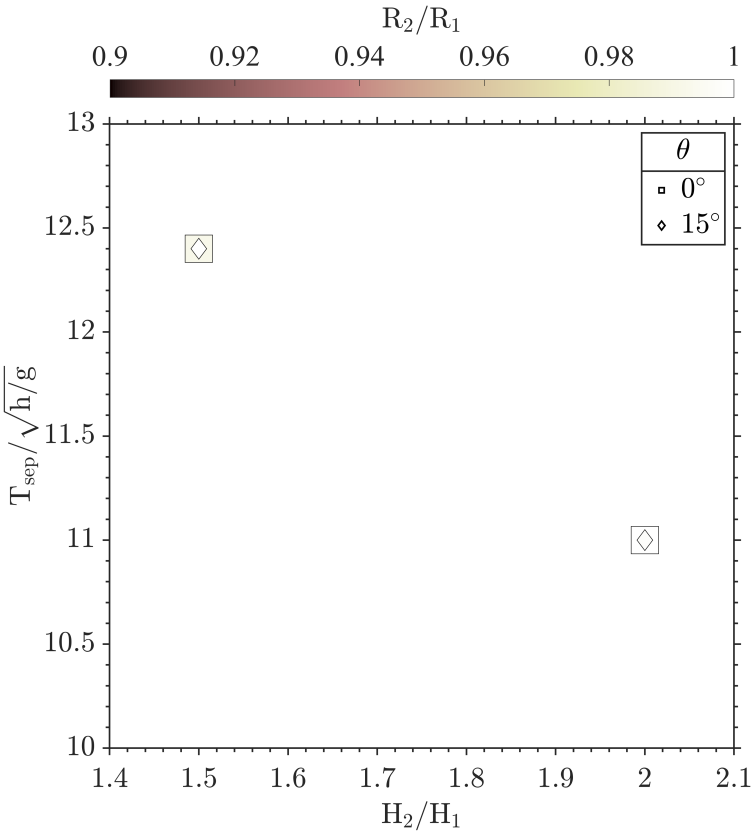

Figure 4.20: Normalized runups associated with the first (left) and second (right) wave.

Results show that higher fluid velocities and local accelerations are associated with higher wave height ratios and shorter separation times, hinting at a contribution of the magnitude of successive incoming waves. The angle of incidence of the wave train plays an important role in the magnitude of the directional flows. While cross-shore quantities reduce their magnitude with wave obliquity, long-shore, and vertical components increase. These latter quantities can contribute to building sediment transport along the coast in combination with sediment suspension.

Runups over the beach were estimated using image analysis, rectifying image frames from recorded videos of each experimental realization, and calculating the maximum distance traveled by the upwash flow over the beach for each incoming wave. The method is effective and accurate in obtaining the runups. Comparisons against theoretical experiments associated with the first and incoming wave show minor differences when no obliquity is considered. However, when the wave

angle increases, there is a reduction in the runup elevation due to wave diffraction. Similar behavior is observed in the runup generated by the second wave. However, the analyzed cases present that theoretical data are always lower than the measurements.

In general, results depict that higher angles of incidence induce both, lower maximum runups and lower cross-shore fluid velocities at the moment the wave-swash interaction occurs, variation attributed to the loss of energy the waves experience by the effect of the refraction as they propagate to the shallower region of the directional basin.

Future work could include increasing the number of experimental cases and combining different wave elevations, separation times, and angles of incidence to assess the flow and runup variations associated with the physical parameters of the waves and wave obliquity. Considering variations in wave angles in the characteristic ratios could give new understandings to characterize the wave-swash interactions quantitatively observed in the field.

Another extension of this investigation could consider including and measuring sediment transport induced by wave-swash interactions and associated directional flows. These experiments can reveal further insights into how the sediments distribute in different directions by joint action of cross-shore, long-shore, and vertical flows and accelerations.

In terms of the runups, theoretical formulations do not include the effect of wave obliquity in the runup calculation. From the experimental cases and measurements, it could be possible to extend state-of-art formulations to consider the angle of attack of the waves. This improvement could give more precise estimations of the runups for directional waves.

Numerical models, such as Computational Fluid Dynamics (CFD), can also be considered to replicate and model the experimental cases in a directional wave basin to extend the number of cases, forcing conditions, beach characteristics, and runup estimations.

Chapter 5

CONCLUSIONS

Boundary layers driven by oscillatory and solitary waves propagating over permeable sea beds have been estimated for sea floors with different hydraulic conductivities. The interfacial conditions were analyzed by implementing two boundary conditions commonly used in permanent flows according to the formulations proposed by Beavers and Joseph (1967) and Le Bars and Worster (2006), solved numerically and analytically, respectively.

Analytical solutions for oscillatory boundary layers flows were found with the implementation of the Le Bars and Worster boundary condition, extending the classical formulations for oscillatory flows over impermeable sea floors from Stokes (1880); Batchelor (2000); Svendsen (2006). Analytical results, which depend on an empirical parameter present an agreement with the numerical approach, validating the theory for the interfacial similarity between both boundary conditions.

Direct comparisons show that the analytical solutions are in good agreement with the empirical data, demonstrating the robustness of the solutions and revealing the importance of the transition zone within the porous layer, controlled by an empirical coefficient.

Error analysis of the solutions against the empirical data shows that the empirical coefficient needs to be modified to improve the fitting conditions. This coefficient is sensitive to the permeability of the porous media and controls the length of the transition zone. It is found that this coefficient is significant for accurate modeling of boundary layer flows, as it modifies the depth of the transition zone and thus, the structure of the boundary layer flows and bed shear stresses. One of the main findings of this work is that the transition zone scales with either the grain diameter or the hydraulic conductivity of the porous media.

Laboratory-generated wave-swash interactions in a wave flume were characterized quantitatively by parametrizing them in terms of wave height and temporal ratio H_2/H_1 and $T_{\text{sep}}/T_{\text{swash}}$, constructed from the successive solitary wave features. These quantifiers are functional not only to group them according to the type of interaction, which facilitates the generation of clusters for each interaction observed in the field, but also to associate other quantities to the type of interaction, such as accelerations and times at which the interactions occur.

Developing total vertical accelerations was obtained by applying a theoretical approach based on the vertical component of the Navier-Stokes equations, which considered the use of measured quantities, such as surface elevations and bottom pressures. Accelerations exhibit that strong and weak-wave backwash interactions are prone to develop higher magnitudes, reaching magnitudes higher than the acceleration of gravity. Analysis of the generated flows reveals a lag between the maximum vertical acceleration and the maximum horizontal and vertical components, for which peak velocities follow peak accelerations, hinting to a potential accelerated movement of the sediment particles, predisposed to be transported onshore or suspended by the velocity components.

The experimental work conducted provides an understanding of different aspects of the swash and the wave-swash interactions in this coastal zone, such as their region of influence, the quantitative characterization, which had not been provided previously by the scientific community, and the insights on the kinematic conditions developed by the interactions.

In the same line of research, it was observed that wave obliquity can affect the maximum velocities, local accelerations, and runup elevations over a beach when a train of solitary waves is considered. Cross-shore, long-shore, and vertical velocities show that higher magnitudes are linked to a higher wave height ratio in combination with a shorter separation time between the wave events. Runup developed by the first and second waves presents similarities when compared to theoretical estimations, exhibiting a considerable reduction with wave obliquity. Runups analyzed quantitatively show that higher wave amplitudes are associated with larger separation times and lower wave height ratios exhibiting dependence on the characteristics of the wave-swash interactions. Results present that wave obliquity is a significant factor that needs to be considered for the analysis of coastal processes.

Bibliography

B. Alazmi and K. Vafai. Analysis of fuid fow and heat transfer interfacial conditions between a porous medium and a fuid layer. *Int. J. Heat Mass Transf.*, 44:1375–1749, 2001.

J. M. Alsina, S. Falchetti, and T. E. Baldock. Measurements and modelling of the advection of suspended sediment in the swash zone by solitary waves. *Coast. Eng.*, 56:621–631, 2009.

J. M. Alsina, I. Cáceres, M. Brocchini, and T. Baldock. An experimental study on sediment transport and bed evolution under different swash zone morphological conditions. *Coast. Eng.*, 68:31–43, 2012.

J. M. Alsina, E. M. Padilla, and I. Cáceres. Sediment transport and beach profile evolution induced by bi-chromatic wave groups with different group periods. *Coast. Eng.*, 114:325–340, 2016.

J. M. Alsina, J. van der Zanden, I. Cáceres, and J. S. Ribberink. The influence of wave groups and wave-swash interactions on sediment transport and bed evolution in the swash zone. *Coast. Eng.*, 140:23–42, 2018.

P. Angot, B. Goyeau, and J. A. Ochoa-Tapia. A nonlinear asymptotic model for the inertial flow at a fluid-porous interface. *Adv. Water Resour.*, 149:1–11, 2021.

J. K. Arthur, D. W. Ruth, and M. F. Tachie. Porous medium flow and an overlying parallel flow: Piv interrogation area and overlaps, interfacial location, and depth ratio effects. *Transp. Porous Media*, 97:5–23, 2013.

T. Baldock, A. J. Baird, D. P. Horn, and T. Mason. Measurements and modeling of swash-induced pressure gradients in the surface layers of a sand beach. *J. Geophys. Res.*, 106, NO. C2:2653–2666, 2001.

T. E. Baldock and P. Holmes. Simulation and prediction of swash oscillations on asteep beach. *Coast. Eng.*, 36:219–242, 1999.

T. E. Baldock and M. G. Hughes. Field observations of instantaneous water slopes and horizontal pressure gradients in the swash-zone. *Cont. Shelf Res.*, 26(5):574–588, 2006.

I. Barranco and P. L.-F. Liu. Run-up and inundation generated by non-decaying dam-break bores on a planar beach. *J. Fluid Mech.*, 915:A81:1–29, 2021.

G. K. Batchelor. *An introduction to Fluid Dynamics*. Cambridge University Press, 2000.

J. Bear. *Dynamics of Fluids in Porous Media*. Dover, 1972.

G. S. Beavers and D. D. Joseph. Boundary conditions at a naturally permeable bed. *J. Fluid Mech.*, 30:197–207, 1967.

P. Blondeaux and G. Vittori. Revisiting the momentary stability analysis of the stokes boundary layer. *J. Fluid. Mech.*, 919:A36:1–15, 2021.

J. Boussinesq. Théorie des ondes et des remous qui se propagent le long d'un canal rectangulaire horizontal, en communiquant au liquide contenu dans ce canal des vitesses sensiblement pareilles de la surface au fond. *Journal de mathématiques pures et appliquées*, 17:55–108, 1872.

H. C. Brinkman. A calculation of the viscous force exerted by a flowing fluid on a dense swarm of particles. *Appl. Sci. Res.*, 1:27–34, 1949.

M. Brocchini and T. E. Baldock. Recent advances in modeling swash zone dynamics: Influence of surf-swash interaction on nearshore hydrodynamics and morphodynamics. *Rev. Geophys.*, 46: RG3003, 2008.

L. G. Brown. A survey of image registration techniques. *ACM Comput. Surv.*, 24:325–376, 1992.

P. C. Carman. Fluid flow through granular beds. *Transactions, Institution of Chemical Engineers, London*, 15:150–166, 1937.

P. Chardón-Maldonado, J. C. Pintado-Patiño, and J. A. Puleo. Advances in swash-zone research: Small-scale hydrodynamic and sediment transport processes. *Coast. Eng.*, 115:8–25, 2016.

W. Chen, J. J. van der Werf, and S. J. M. H. Hulscher. A review of practical models of sand transport in the swash zone. *Earth. Sci. Rev.*, 238:104355:1–17, 2023.

D. C. Conley and D. L. Inman. Ventilated oscillatory boundary layers. *J. Fluid Mech.*, 273: 261–284, 1994.

S. Corvaro, E. Seta, A. Mancinelli, and M. Brocchini. Flow dynamics on a porous medium. *Coast. Eng.*, 91:280–298, 2014.

I. Cáceres and J. M. Alsina. Intra-swash hydrodynamics and sediment flux for dambreak swash on coarse-grained beaches. *Cont. Shelf Res.*, 41:61–76, 2012.

Anthony MJ Davis and David F James. Penetration of shear flow into an array of rods aligned with the flow. *Can J Chem Eng.*, 82:1169–1174, 2004.

R. G. Dean and R. A. Dalrymple. *Coastal processes with engineering applications*. Cambridge University Press, 2004.

P. A. Domenico and F. W. Schwartz. *Physical and Chemical Hydrogeology*. John Wiley and Sons, 1990.

B. Elfrink and T. Baldock. Hydrodynamics and sediment transport in the swash zone: a review and perspectives. *Coast. Eng.*, 45:149–167, 2002.

L. Erikson, M. Larson, and H. Hanson. Prediction of swash motion and run-up including the effects of swash interaction. *Coast. Eng.*, 52:285–302, 2005.

J. J. Feng and Y.-N. Young. Boundary conditions at a gel-fluid interface. *Phys. Rev. Fluids*, 5: 124304: 1–13, 2020.

M. Florence, N. Stark, B. Raubenheimer, and S. Elgar. Nearshore vertical pore pressure gradients and onshore sediment transport under tropical storm forcing. *J. Waterway, Port, Coastal, Ocean Eng.*, 148(6), 04022023:1–7, 2022.

G. Fromant, D. Hurther, J. van der Zanden, D. A. van der A, I. Cáceres, T. O'Donoghue, and J. S. Ribberink. Wave boundary layer hydrodynamics and sheet flow properties under large-scale plunging-type breaking waves. *J. Geophys. Res. Oceans*, 124:75–98, 2019.

M. Ghisalberti. Obstructed shear flows: similarities across systems and scales. *J. Fluid Mech.*, 641:51–61, 2009.

A. Goharzadeh, A. Khalili, and B. B. Jørgensen. Transition layer thickness at a fluid-porous interface. *Phys. Fluids*, 17:057102:1–11, 2005.

D. G. Goring. *Tsunamis–The propagation of long waves onto a shelf*. Doctoral Thesis. California Institute of Technology, 1979.

D. G. Goring and V. I. Nikora. Despiking acoustic doppler velocimeter data. *J. Hydraul. Eng.*, 128:1:117–126, 2002.

B. Goyeau, D. Lhuillier, D. Gobin, and M.G. Velarde. The effect of a transition layer between a fluid and a porous medium: shear flow in a channel. *Int. J. Heat Mass Transf.*, 46:4071–4081, 2003.

R. Grimshaw. The solitary wave in water of variable depth. *J. Fluid Mech.*, 42. Part 3:639–656, 1970.

S. K. Gupte and S. G. Adavani. Flow near the permeable boundary of a porous medium: An experimental investigation using lda. *Exp. Fluids*, 22:408–422, 1997.

L. H. Holthuijsen. *Waves in oceanic and coastal Waters*. Cambridge University Press, 2007.

S. Hossain and N. E. Daidzic. The shear-driven fluid motion using oscillating boundaries. *J. Fluids Eng.*, 134(5): 051203:1–13, 2012.

M. G. Hughes and A. S. Moseley. Hydrokinematic regions within the swash zone. *Cont. Shelf. Res.*, 27:2000–2013, 2007.

M. G. Hughes, G. Masselink, and R. W. Brander. Flow velocity and sediment transport in the swash zone of a steep beach. *Marine Geology*, 138:91–103, 1997.

J. N. Hunt. On the damping of gravity waves propagated over a permeable surface. *J. Geophys. Res.*, 64:4:43779–442, 1959.

L. Issa. A simplified model for unsteady pressure driven flows in circular microchannels of variable cross-section. *Appl. Math. Model.*, 59:410–426, 2018.

D. W. T. Jackson and A. D. Short. *Sandy Beach Morphodynamics*. Elsevier, 2020.

D. F. James and A. M. J. Davis. Flow at the interface of a model fibrous porous medium. *J. Fluid Mech.*, 426:47–72, 2001.

S. Karmakar, R. Usha, G. Chattopadhyay, S. Millet, J. V. Ramana Redy, and P. Shukla. Stability of a plane poiseuille flow in achannel bounded by anisotropic porouswalls. *Phys. Fluids*, 34: 034103: 1–28, 2022.

G. A. Kikkert, T. O'Donoghue, D. Pokrajac, and N. Dodd. Experimental study of bore-driven swash hydrodynamics on impermeable rough slopes. *Coast. Eng.*, 60:149–166, 2012.

M. Le Bars and M. G. Worster. Interfacial conditions between a pure fluid and a porous medium: implications for binary alloy solidification. *J. Fluid Mech.*, 550:149–173, 2006.

L. Li, J. Zhang, Z. Xu, Y.-N. Young, J. J. Feng, and P. Yue. An arbitrary lagrangian-eulerian method for simulating interfacial dynamics between a hydrogel and a fluid. *J. Comput. Phys.*, 451:1–22, 2022.

P. L.-F. Liu. Damping of water waves over porous bed. *Journal of the Hydraulics Division*, 99: 2263–2271, 1973.

P. L.-F. Liu. Mass transport in water waves propagated over a permeable bed. *Coast. Eng.*, 1: 79–96, 1977.

P. L.-F. Liu and R. A. Dalrymple. The damping of gravity water-waves due to percolation. *Coast. Eng.*, 8:33–49, 1984.

P. L.-F. Liu and A. Orfila. Viscous effects on transient long–wave propagation. *J. Fluid Mech.*, 520:83–92, 2004.

P. L.-F. Liu and A. Orfila. Boundary layer flow and bed shear stress under a oscillatory wave. *J. Fluid Mech.*, 574:449–463, 2007a.

P. L.-F. Liu, M. Davis, and S. Downing. Wave–induced boundary layer flows above and in a permeable bed. *J. Fluid Mech.*, 325:195–218, 1996.

P. L.-F. Liu, Y. S. Park, and E. A. Cowen. Boundary layer flow and bed shear stress under a solitary wave. *J. Fluid Mech.*, 574:449–463, 2007a.

P. L.-F. Liu, Y. S. Park, and E. A. Cowen. Boundary layer flow and bed shear stress under a solitary wave. *J. Fluid Mech.*, 574:449–463, 2007b.

Q. Liu and A. Prosperetti. Pressure-driven flow in a channel with porous walls. *J. Fluid Mech.*, 679:77–100, 2011.

H.-Y. Lo, Y. S. Park, and P. L.-F. Liu. On the run-up and back-wash processes of single and double solitary waves — an experimental study. *Coast. Eng.*, 80:1–14, 2013.

M. Luhar, S. Coutu, E. Infantes, S. Fox, and H. Nepf. Wave-induced velocities inside a model seagrass bed. *J. Geophys. Res.*, 115:C12005:1–15, 2010.

P. A. Madsen, D. R. Fuhrman, and H. A. Schäffer. On the solitary wave paradigm for tsunamis. *J. Geophys. Res.*, 113:C12012, 2008.

G. Mancini, R. Briganti, R. McCall, N. Dodd, and F. Zhu. Numerical modelling of intra-wave sediment transport on sandy beaches using a non-hydrostatic, wave-resolving model. *Ocean Dyn.*, 71(1):1–20, 2021.

C. Martínez, M. Contreras-Lopez, P. Winckler, H. Hidalgo, E. Godoy, and R. Agredano. Coastal erosion in central chile: A new hazard? *Ocean Coast. Manag.*, 156:141–155, 2018.

B. Mason and H. Yeh. Sediment liquefaction: A pore-water pressure gradient viewpoint. *Bull. Seismol. Soc. Am.*, 106:1908–1913, 2016.

G. Masselink and J. A. Puleo. Swash-zone morphodynamics. *Cont. Shelf Res.*, 26:661–680, 2006.

G. Masselink, P. Russell, I. Turner, and C. Blenkinsopp. Net sediment transport and morphological change in the swash zone of a high-energy sandy beach from swash event to tidal cycle time scales. *Mar. Geol.*, 267:18–35, 2009.

G. Masselink, B. Castelle, T. Scott, G. Dodet, S. Suanez, D. Jackson, and F. Floc'h. Extreme wave activity during 2013/2014 winter and morphological impacts along the atlantic coast of europe. *Geophys. Res. Lett.*, 43 (5):2135–2143, 2016.

A. Mathieu, Z. Cheng, J. Chauchat, C. Bonamy, and T.-J. Hsu. Numerical investigation of unsteady effects in oscillatory sheet flows. *J. Fluid. Mech.*, 943:A7:1–33, 2022.

M. Mazzuoli, A. G. Kidanemariam, and M. Uhlmann. Direct numerical simulations of ripples in an oscillatory flow. *J. Fluid Mech.*, 863:572–600, 2019.

M. Mazzuoli, P. Blondeaux, G. Vittori, M. Uhlmann, J. Simeonov, and J. Calantoni. Interface-resolved direct numerical simulations of sediment transport in a turbulent oscillatory boundary layer. *J. Fluid Mech.*, 885:A28: 1–31, 2020.

C. R. McClain, N. E. Huang, and L. J. Pietrafesa. Application of a 'radiation-type' boundary condition to the wave porous bed problem. *J. Phys. Oceanogr.*, 7:6:823–835, 1977.

C. C. Mei, M. Stiassnie, and D. K.-P. Yue. *Theory and Applications of Ocean Surface Waves*. World Scientific, 2005.

C. Meza-Valle and N. Pujara. Flow in oscillatory boundary layers over permeable beds. *Phys. Fluids*, 34, 092112, 2022.

M. Minale. Momentum transfer within a porous medium. ii. stress boundary condition. *Phys. Fluids*, 26:123102: 1–15, 2014.

M. R. Morad and A. Khalili. Transition layer thickness in a fluid-porous medium of multi-sized spherical beads. *Exp. Fluids*, 46:323–330, 2009.

N. Mordant, A. M. Crawford, and E. Bodenschatz. Experimental lagrangian acceleration probability density function measurement. *Physica D*, 193:245–251, 2004. doi: 10.1016/j.physd.2004.01.041.

D. A. Nield. The beavers–joseph boundary condition and related matters: A historical and critical note. *Transp. Porous Med.*, 78:537–540, 2009.

J. A. Ochoa-Tapia and S. Whitaker. Momentum transfer at the boundary between a porous medium and a homogeneous fluid—i. theoretical development. *Int. J. Heat Mass Transf.*, 38:2635–2646, 1995a.

J. A. Ochoa-Tapia and S. Whitaker. Momentum transfer at the boundary between a porous medium and a homogeneous fluid—ii. comparison with experiment. *Int. J. Heat Mass Transf.*, 38:2647–2655, 1995b.

T. O'Donoghue, D. Pokrajac, and L. J. Hondebrink. Laboratory and numerical study of dambreak-generated swash on impermeable slopes. *Coast. Eng.*, 57:513–530, 2010.

T. O'Donoghue, G. A. Kikkert, D. Pokrajac andN. Dodd, and R. Briganti. Intra-swash hydrodynamics and sediment flux for dambreak swash on coarse-grained beaches. *Coast. Eng.*, 112: 113–130, 2016.

J. C. Pintado-Patiño, J. A. Puleo, D. Krafft, and A. Torres-Freyermuth. Hydrodynamics and sediment transport under a dam-break-driven swash: An experimental study. *Coast. Eng.*, 170: 103986: 1–18, 2021.

N. Pujara, P. L.-F. Liu, and H. Yeh. The swash of solitary waves on a plane beach: flow evolution, bed shear stress and run-up. *J. Fluid Mech.*, 779:556–597, 2015a.

N. Pujara, P. L.-F. Liu, and H. H. Yeh. An experimental study of the interaction of two successive solitary waves in the swash: A strongly interacting case and a weakly interacting case. *Coast. Eng.*, 105:66–74, 2015b.

N. Pujara, K. T. Du Clos, S. Ayres, E. A. Variano, and L. Karp-Boss. Measurements of trajectories and spatial distributions of diatoms (coscinodiscus spp.) at dissipation scales of turbulence. *Expt. Fluids*, 62:149, 2021. doi: 10.1007/s00348-021-03240-5.

J. A. Puleo and T. Butt. The first international workshop on swash-zone processes. *Cont. Shelf Res.*, 26:556–560, 2006.

J. A. Puleo and A. Torres-Freyermuth. The second international workshop on swash-zone processes. *Coast. Eng.*, 115:1–7, 2016.

J. A. Puleo, R. A. Beach, R. A. Holman, and J. S. Allen. Swash zone sediment suspension and transport and the importance of bore-generated turbulence. *J. Geophys. Res.*, 105:17,021–17,044, 2000.

J. A. Putnam. Loss of wave energy due to percolation in a permeable sea bottom. *Trans. Am. Geophys. Union*, 30:349–356, 1949.

N. G. Rangel-Buitrago, G. Anfuso, and A. T. Williams. Coastal erosion along the caribbean coast of colombia: Magnitudes, causes and management. *Ocean Coast. Manag.*, 156:141–155, 2015.

R. O. Reid and K. Kajiura. On the damping of gravity waves over a permeable sea bed. *Trans. Am. Geophys. Union*, 38:662–666, 1957.

L. Rosenhead. *Laminar Boundary Layers*. Dover, 1988.

G. Ruffini, R. Briganti, J. M. Alsina, M. Brocchini, N. Dodd, and R. McCall. Numerical modeling of flow and bed evolution of bichromatic wave groups on an intermediate beach using nonhydrostatic xbeach. *J. Waterway, Port, Coastal, Ocean Eng.*, 146(1), 04019034:1–17, 2020.

P. G. Saffman. On the boundary condition at the surface of a porous medium. *Stud. Appl. Maths*, L(2):93–101, 1971.

A. Samanta. Role of slip on the linear stability of a liquid flow through a porous channel. *Phys. Fluids*, 29:094103: 1–14, 2017.

P. Smit, G. Stelling, D. J. A. Roelvink, J. van Thiel de Vries, R. McCall, A. van Dongeren, C. Zwinkels, and R. Jacobs. *XBeach: Non-hydrostatic model: Validation, verification and model description*. Deltares Technical Report, 2010.

Y. Song and M. J. Rau. Viscous fluid flow inside an oscillating cylinder and its extension to stokes' second problem. *Phys. Fluids*, 32, 043601, 2020.

I. M. Sou and H. Yeh. Laboratory study of the cross-shore flow structure in the surf and swash zones. *J. Geophys. Res.*, 116, C03002:1–15, 2011.

N. Stark, P. Mewis, B. Reeve, M. Florence, J. Piller, and J. Simon. Vertical pore pressure variations and geotechnical sediment properties at a sandy beach. *Coast. Eng.*, 172, 104058:1–15, 2022.

G. G. Stokes. *Mathematical and Physical Papers, Volume I.* Cambridge University Press, 1880.

B. M. Sumer. *Liquefaction around marine structures*. World scientific, 2014.

B. M. Sumer, H. Guner, and N. M. Hansen. Laboratory observations of flow and sediment transport induced by plunging regular waves. *J. Geophys. Res.: Oceans*, 118:6161–6182, 2013. doi: 10.1002/jgrc.20450.

I. A. Svendsen. *Introduction to Nearshore Hydrodynamics*. Advanced Series on Ocean Engineering, 2006.

C. E. Synolakis. The runup of solitary waves. *J. Fluid Mech.*, 185:523–545, 1987.

N. Tilton and L. Cortalezzi. Linear stability analysis of pressure-driven flows in channels with porous walls. *J. Fluid Mech.*, 604:411–445, 2008.

A. Toimil, P. Camus, I. J. Losada, G. Le Cozannet, R. J. Nicholls, D. Idier, and A. Maspataud. Climate change-driven coastal erosion modelling in temperate sandy beaches: Methods and uncertainty treatment. *Earth-Science Reviews*, 202:103110, 2020.

G. Vittori, P. Blondeaux, M. Mazzuoli, J. Simeonov, and J. Calantoni. Numerical investigation of unsteady effects in oscillatory sheet flows. *Int. J. Multiphase Flow*, 133:1–16, 2020.

J.-J. Webber and H.-E. Huppert. Stokes drift in coral reefs with depth-varying permeability. *Philos. Trans. R. Soc. Lond., A*, 378:1–12, 2020.

J.-J. Webber and H.-E. Huppert. Stokes drift through corals. *Environmental Fluid Mechanics*, 2: 1–17, 2021.

A. Wu and P. Mirbod. Experimental analysis of the flow near the boundary of random porous media. *Phys. Fluids*, 30:047103, 2018.

Y.-T. Wu, P. L.-F. Liu, K.-S. Wang, and H.-H. Hwung. Runup of laboratory-generated breaking solitary and periodic waves on a uniform. *J. Waterw. Port, Coast.*, 144 (6):04018023, 2018.

Y.-T. Wu, P. Higuera, and P. L.-F. Liu. On the evolution and runup of a train of solitary waves on a uniform beach. *Coast. Eng.*, 170, 104015:1–22, 2021.

Y.-T. Wu, K.-W. Wang, and N. Kobayashi. Runup of breaking solitary waves on rough uniform slopes. *Ocean Eng.*, 245:110551, 2022.

H. Yeh and H. B. Mason. Sediment response to tsunami loading: mechanisms and estimates. *Géotechnique*, 64(2):131–143, 2014.

Q. Zhang and A. Prosperetti. Pressure-driven flow in a two-dimensional channel with porous walls. *J. Fluid Mech.*, 631:1–21, 2009.